Exploring Nonresonant Interactions in Condensed Matter by Two-Dimensional Terahertz Spectroscopy

D I S S E R T A T I O N

zur Erlangung des akademischen Grades

Dr. rerum naturalium
(Dr. rer. nat.)
im Fach Physik

eingereicht an der
Mathematisch-Naturwissenschaftlichen Fakultät
Humboldt-Universität zu Berlin

von
Dipl.-Phys. Giulia Folpini

Präsidentin der Humboldt-Universität zu Berlin:
Prof. Dr.-Ing. Dr. Sabine Kunst

Dekan der Mathematisch-Naturwissenschaftlichen Fakultät:
Prof. Dr. Elmar Kulke

Gutachter/innen:
1. Prof. Dr. Thomas Elsaesser
2. Prof. Dr. Kurt Busch
3. Prof. Dr. Alfred Leitenstorfer

Tag der mündlichen Prüfung:
18.12.2017

Abstract

Terahertz (THz) spectroscopy gives insight into a large variety of low-frequency excitations in condensed matter, such as molecular rotations, phonons, soft modes in ferroelectrics and intersubband transitions in semiconductors. Semiconductor crystals such as GaSe are used generate fields of MV/cm in the 20 THz range, and of 100 kV/cm in the 1-5 THz range by difference frequency mixing. Moreover, novel sources using organic crystals like OH1 can generate strong fields (800 kV/cm) with a spectrum covering several octaves, from 1 THz to 35 THz. The very large detection bandwidth provided by electro-optic sampling (EOS) with ultrashort pulses is then crucial for exploiting such powerful broadband sources.

We demonstrate the potential of linear absorption spectroscopy with a multi-octave spanning THz source by measuring the full librational band of water, determined by its hydrogen bond network. Comparing neat water to hydrated biomolecules (DNA), we identify the impact of local interactions of the hydrated biointerface. We show that water molecules hydrogen-bonded to phosphate groups display a blue shifted librational absorption, caused by a stronger bonding potential.

The main part of the thesis is devoted to nonlinear THz spectroscopy, in particular nonresonant interactions and higher-order nonlinear processes. Owing to a collinear interaction geometry and a fully phase resolved detection by EOS, nonlinear multidimensional THz spectroscopy gives insight into the dynamics and correlations of phenomena in the THz spectral range.

We present two-dimensional two-color spectroscopy on GaAs quantum wells. A powerful pulse at 20 THz resonantly excites intersubband transitions driving Rabi oscillations. A nonresonant 2 THz pulse is used to coherently control the phase of the nonlinearly emitted field, leading to switching between absorptive and emittive behavior, resulting in an overall increase of the resonant absorption at 20 THz without direct energy exchange with the THz pulse.

To explore strongly coupled interactions, the 1.1 THz soft mode of the molecular crystal aspirin is probed by two-dimensional THz-THz spectroscopy. In the tightly packed crystal, the local field couples low frequency nuclear vibrations to highly polarizable electronic dipoles, which dominate the nonlinear response. As a consequence of the highly nonperturbative light-matter interaction, a polarization dependent nonlinear shift of the emission frequency is unveiled.

Zusammenfassung

Terahertz (THz) Spektroskopie ist hervorragend geeignet, dafür eine Vielzahl von Anregungen mit niedriger Frequenz in kondensierter Materie zu erforschen. Prominente Beispiele hierfür sind Molekülrotationen, Phononen, Softmoden in Ferroelektrika und Intersubbandübergänge in Halbleitern. Halbleiterkristalle wie GaSe können verwendet werden, um elektrische Felder mit Stärken von MV/cm im 20 THz-Bereich und von 100 kV/cm im 1-5-THz-Bereich durch Differenzfrequenzmischung zu erzeugen. Darüber hinaus eignen sich organische Kristalle (OH1) als neuartige Quellen, um starke elektrische Felder (800 kV/cm) über einen mehrere Oktaven umspannenden Spektralbereich von 1 THz bis 35 THz zu erzeugen. Die sehr große Bandbreite, welche mittels elektrooptischer Detektion (EOD) durch ultrakurze Pulse zugänglich ist, erweist sich dabei als entscheidend für die Ausnutzung so starker Breitbandquellen.

Wir zeigen das Potential linearer Absorptionsspektroskopie, welche eine THz-Quelle mit einem mehrere Oktaven umspannenden Spektralbereich verwendet, durch die Bestimmung der vollen Librationsbande von Wasser. Diese wird hauptsächlich durch sein Wasserstoffbindungsnetzwerk bestimmt. Durch den Vergleich von reinem Wasser mit hydratisierten Biomolekülen (DNA) ist es gelungen, den Einfluss lokaler Wechselwirkungen des hydratisierten Biointerfaces zu identifizieren. Wassermoleküle, welche über Wasserstoffbrückenbindungen an Phosphatgruppen gebunden sind, haben aufgrund eines stärkeren Bindungspotentials eine blau verschobene Librationsabsorption.

Der Hauptteil der Arbeit widmet sich der nichtlinearen THz-Spektroskopie, mit einem Fokus auf nichtresonanten Wechselwirkungen und nichtlinearen Prozessen höherer Ordnung. Aufgrund der kollinearen Interaktionsgeometrie und einer vollständig phasenaufgelösten Detektion durch EOD ermöglicht nichtlineare und zweidimensionale (2D) THz-Spektroskopie Einblicke in die Dynamik und Korrelation von Phänomenen im Spektralbereich von 0.5 bis 100 THz.

Im Rahmen dieser Arbeit werden GaAs-Quantentöpfe durch 2D-Spektroskopie untersucht. Durch einen starken Puls mit einer Frequenz von 20 THz werden in der Probe Rabi-Oszillationen von Intersubband-Übergängen angeregt. Ein nichtresonanter 2-THz-Puls wird verwendet, um die Phase des nichtlinear emittierten Feldes sowie den Übergang zwischen absorbierenden oder emittierendem Verhalten zu kontrollieren. Dies führt zu einer Erhöhung der resonanten Absorption bei 20 THz ohne einen direkten Energieaustausch mit dem THz-Puls.

Um stark gekoppelte Wechselwirkungen zu erforschen, wurde die 1.1-THz Softmode des Molekülkristalls Aspirin durch zweidimensionale THz-THz-Spektroskopie untersucht. Im dicht gepackten Kristall koppeln durch das lokale elektrische Feld niederfrequente nukleare Vibrationen an stark polarisierbare elektronische Dipole, welche die nichtlineare Antwort dominieren. Als Konsequenz der nicht-pertubativen Licht-Materie-Wechselwirkung wird eine polarisationsabhängige, nichtlineare Verschiebung der Emissionsfrequenz gefunden.

Contents

Introduction

The terahertz (THz) spectral range, with wavelengths between 3 μm and 3 mm, bridges the gap between optics and electronics, where interesting physics abounds. In the past twenty years, the development of powerful THz sources [1–3] and coherent detection schemes like electro-optic sampling (EOS) [4] has spurred the development of linear and nonlinear THz spectroscopy, including multidimensional techniques derived from three-dimensional infrared spectroscopy [5–7].

THz spectroscopy offers insight into a wide range of low frequency excitations in condensed matter, such as soft modes in ferroelectric materials [8], molecular rotations and vibrations in liquid and gases [9, 10], phonons, polaritons, multiple quantum coherences and interband four wave mixing tunneling in semiconductors [11–14], excitons and intersubband excitations in low dimensional semiconductor quantum wells [15–17], ultrastrong light-matter coupling regimes in semiconductor heterostructures and metamaterials [18, 19].

Exploiting a novel octave-spanning THz source [20] opens up new perspectives on THz linear absorption spectroscopy. We observed the librational band of bulk liquid water (10-30 THz) and studied the changes brought on by water forming hydrogen bonds to other organic molecules, in particular to the phosphate groups on the backbone of DNA [21].

Exploring the dynamics and the correlations of these often highly-collective phenomena requires a nonlinear multidimensional THz spectroscopy. Using the concept of frequency vectors in a multidimensional frequency space [22], a coherent 2D THz spectroscopy can be implemented between 1 and 40 THz, with multiple THz pulses in a collinear geometry and a fully phase resolved detection technique [17, 23].

Multidimensional THz spectroscopy relies on coherent detection in a large bandwidth to be able to capture the interactions of the huge electronic dipoles typical of this frequency range. Two-dimensional THz spectroscopy can explore high-order nonlinearities involving multiple nonresonant interactions with the THz

electric fields to study, e.g., dark multiple quantum coherences [24]. In crystalline materials, highly collective effects involving a large number of molecules can also be explored. As an example, nonresonant THz radiation causes tunneling in semiconductors and ferroelectrics [8],[25], where excited charges are created by exploiting the very large decoherence rate they experience when the THz electric fields drives them over a large portion of the Brillouin zone [26].
Low frequency interactions in molecular crystal also have a markedly collective character: the local field causes highly coupled electronic and vibrational dipoles at low frequencies, so that the low frequency phonons behave like soft modes. Using 2D THz-THz spectroscopy, we have studied the response of the soft mode in crystalline aspirin, unveiling a nonlinearity characterized by a polarization-dependent frequency shift of the mode [27].
Furthermore, to explore the potential of nonresonant THz control of emission in the mid-infrared range, we implemented two-color spectroscopy with radiation at 2 THz and 25 THz, exploiting our broadband THz detection scheme. Shining powerful 2 THz radiation on GaAs quantum wells, we can affect the net absorption of mid-IR radiation resonant to an intersubband transition. The phase of the emitted field can be manipulated without any direct exchange of energy with the THz field [28], opening up the possibility of lossless nonresonant control of infrared devices.

Outline

This thesis consists of four chapters, the first two discussing the experimental and theoretical framework of multidimensional THz spectroscopy and the following presenting original experimental results.
In Chapter 1 generation and detection techniques for THz radiation are discussed. After a brief overview of existing detectors and sources, the focus is on techniques employed in our set-up: specifically, phase-resolved detection via electro-optic sampling and THz and mid-infrared generation by frequency mixing in nonlinearly active GaSe and ZnTe crystals. A novel ultrabroadband THz source is presented, where radiation spanning five octaves is generated in organic crystals such as DSTMS and OH1. To highlight the interest in broadband THz spectroscopy, in Chapter 2 this source is used to perform linear absorption spectroscopy on liquid water both in bulk and at the surface of biological molecules, i.e. hydrated DNA, observing how disturbances in the water hydrogen bond network affect the water librational band in a wide frequency range.
In Chapter 3, after a brief review of third-order infrared spectroscopy, our con-

cept of THz coherent multidimensional spectroscopy is presented and the experimental set-up for THz-THz and THz-midinfrared 2D spectroscopy are described. The specific characteristics of our collinear, phase resolved set-up allow to access collective, nonresonant and highly nonperturbative interaction regimes which would otherwise remain inaccessible in a more classic multidimensional infrared concept.

In Chapter 4 we present a two-color spectroscopy study of nonresonant control of intersubband transitions in GaAs quantum wells. First the theoretical framework of the Stark effect in a rapidly varying electric field and its effect on intersubband excitation and light emission is discussed, then the experimental results are presented: a nonresonant electric field at 2 THz results in field-induced absorption of a resonant 21 THz mid-infrared pulse. The THz effect on the phase of the re-emitted field can be used to nonresonantly control Rabi oscillations. The results are further analyzed in depth by simulating the full interaction of the light fields with an ensemble of two-level systems. The important role of radiative damping and decoherence are discussed.

In Chapter 5, THz-THz spectroscopy is applied to an aspirin molecular crystal, a model system to study the highly collective character of interactions in this frequency range. The aspirin crystal structure and THz spectrum are discussed, focusing particularly on its hybrid rotational-electronic mode at 1.1 THz, which is then described in the framework of Cochran's theory of soft modes. The nonlinear response is modeled as two electronic and vibrational two-level systems coupled to each other by the local electric field: simulating its interaction with external THz electric fields uncovers an interesting type of nonlinearity characterized by a polarization dependent instantaneous shift of the mode emission frequency. The rich experimental signal is presented, showing good agreement both with the soft mode model and with ab initio calculations on the aspirin crystal.

Chapter 1

Ultrafast generation and detection in the terahertz regime

The THz range, extending in wavelength from tens of microns to millimeter waves, covers a wide range of interesting phenomena, such as collective lattice vibrations, spin excitations, vibrational and rotational degrees of freedom of complex molecules, intra-excitonic transitions, free carrier absorption in semiconductors and intersubband transitions in quantum confined structures. The linear response of different materials has been studied by absorption spectroscopy using FTIR or THz spectrometers. Since strong THz sources have become more readily available, nonlinear THz time domain spectroscopy (TDS) has become a thriving field of research.

In this chapter, different methods for generating and detecting THz radiation will be discussed, giving an overview of how the development of new techniques fostered the advance of spectroscopy in the THz window. In particular, detection by electro-optic sampling and generation by frequency mixing in nonlinear crystals will be discussed more in depth. A novel technique for ultrabroadband THz and mid-infrared (MIR) generation in organic crystals with exceptionally high nonlinear coefficients will be introduced, generating a continuous spectrum from 0.5 THz up to 35 THz.

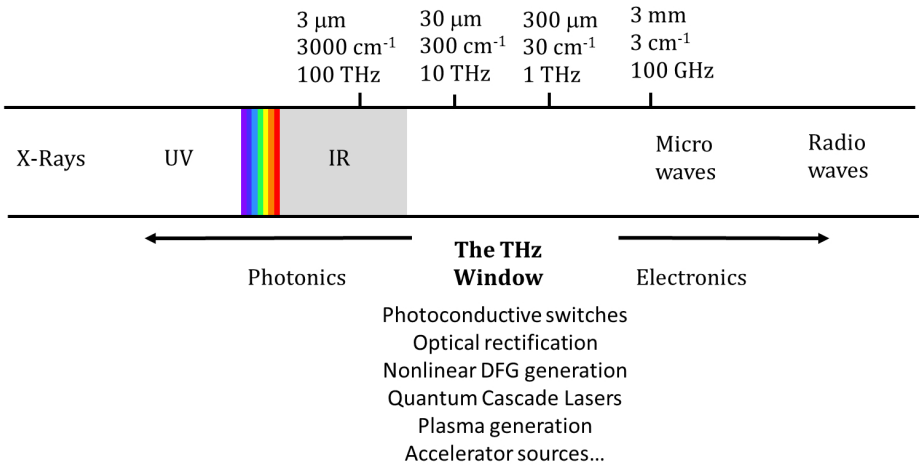

Figure 1.1: The THz window of the electromagnetic spectrum. The development of new generating techniques filled the gap between photonics and electronics.

1.1 The THz window

The THz range, bridging the gap between optics and electronics, is traditionally defined from 0.1 to 10 THz, or from 3 to 300 cm^{-1}, while from 10 to 100 THz lies a spectral region often labeled as mid-infrared (MIR) (Fig.1.1). For years, the spectral region up to 10 THz was termed "the THz gap", due to a striking lack of powerful sources and reliable detectors compared to the neighboring microwave and infrared regions. However, in the last three decades this void has been filled by the development of a wealth of powerful techniques, effectively turning the THz gap into the so called THz window [2].

THz generation techniques

THz radiation can be produced in a handful of different ways, from the most widely employed antennas and nonlinear optics sources, to more complex devices such as quantum cascade lasers. We will now give a brief overview of some of the most relevant techniques.

- **Photoconductive switches and electronic sources**
  Photoconductive (PC) antennas - or Auston switches - for THz generation have first been introduced in the Eighties by *Auston et al.* [29]: they consist of a semiconductor substrate with a short carrier lifetime (typically GaAs), subjected to a bias field by metallic electrodes in the form of strip

lines. The electrodes are usually separated by a gap of the order of tens of microns, where a bias of 10-50 V induces an electric field of the order of a few kV/cm. An ultrashort laser pulse is focused on the substrate, inducing ultrafast transient currents $j(t)$ in the gap which, in turn, radiate an electric field $E_{THz} \propto \frac{dj(t)}{dt}$ in the antenna substrate [2, 30]. Here a substrate lens collects the THz radiation in a a collimated beam which then propagates in free space. The THz output typically peaks around 1 THz in frequency, with moderate field strengths, but more sophisticated antenna geometries can enhance both field strengths and bandwidths, exceeding 5 THz.

GaAs antennas are efficiently pumped at 800 nm by Ti:sapphire laser systems, while the development of InGaAs antennas which can be pumped at 1.5 nm also allowed to pump PC switches with fiber lasers to build extremely compact emitters for radiation around 1 THz [31].

Continuous THz waves can also be generated by mixing laser beams in semiconductor photomixers, producing a field at a frequency corresponding to the beating between the two laser frequencies [30].

- **Optical rectification and DFG**

  Optical rectification, first demonstrated in KDP crystals by *Bass et al.* [32] consists in the generation of short laser pulses by difference frequency mixing of spectral components of the pump in a nonlinear crystal. The electric field - generated from mixing of close-by spectral components - is quasi-DC, hence the name optical rectification. Efficient THz generation requires velocity matching between the infrared pump and the propagating THz pulse: in certain semiconductor crystals such as ZnTe, GaSe and GaP, thanks to a fortuitous matching of the group velocity for an 800 nm pump and phase velocity in the THz ranges, generation between 1 and 2 THz is readily achieved. While these crystals are the most commonly used, a wide range of semiconductors and metals are suitable for OR in the THz range [33].

  mid-infrared pulses at higher frequencies (10-70 THz) can also be generated by nonlinear frequency conversion, exploiting second-order nonlinearities and the birefringence of crystals such as GaSe to achieve phase matched difference frequency mixing between pumps at different wavelengths [34] or between different spectral components of an ultrashort pump pulse [35].

  Alongside more traditional semiconductor materials, some organic molec-

ular crystals have been used for THz generation, in order to exploit their extremely large optical nonlinearities. The most used organic crystals are DAST and closely related organic salts. They are usually pumped with OPAs in the infrared (1.2 μm - 1.6 μm) to generate THz fields of hundreds of kV/cm [3]. Even higher fields can be achieved by using large aperture crystals pumped at a low repetition rate with a powerful pump beam: tailoring of the pump wave front can improve the THz beam focus quality, achieving fields as high as 80 MV/cm for a diffraction limited beam [36]. Recently, other organic materials such as BNA or quinolinum crystals [37, 38] have been studied for generation with an 800 nm pump, while at that wavelength crystals like DAST, DSTMS and OH1 can generate an ultrabroadband spectrum extending up to 30 THz [20].

- **Tilted pulse front generation**
  Lithium niobate crystals have large nonlinear optical coefficients, but contrary to ZnTe or GaSe they do not allow for collinear velocity matching OR. Tilted pulse front pumping (TPFP) was proposed [39] to achieve efficient phase-matched THz generation in LiNbO crystals by having the pump and the THz pulse propagating noncollinearly. Phase matching can be realized by tuning the angle between the two propagation directions, either by having the THz generation in a Cherenkov cone geometry, or by tilting the pump phase fronts using a grating [40]: this technique requires a more complicated pump geometry, but by taking full advantage of the high nonlinear coefficients of LiNbO it can generate field amplitudes up to 650 kV/cm at 0.2 THz [41].

- **Gas plasma generation**
  Different schemes are available to generate THz and MIR radiation in a laser generated gas plasma [42, 43]: early attempts relied on ponderomotive acceleration of plasma electrons, but the use of external DC or AC biases proved more efficient. In particular, the most efficient technique for plasma generation in the 0-5 THz range requires focusing an 800 nm laser pulse at the fundamental and second harmonic frequency in a Nitrogen, air or noble gas plasma: the 400 nm second harmonic pulse breaks the gas inversion symmetry, allowing THz generation by laser induced ionization current [44]. High gas pressure gas pressures field amplitudes up to 400 kV/cm can be achieved [45], together with larger spectral bandwidths

as nonlinear propagation effects in the plasma generate higher frequency components.

- **Quantum cascade lasers**
  Semiconductor diode lasers, relying on electronic transitions over semiconductors band gaps, are widely used in the infrared region [46]. To reach the far-infrared and THz range, QCLs use semiconductor heterostructures (typically GaAs but also Ge,Si and InP are used), where quantum confinement opens up sub-bands in the conduction and valence bands: optical intersubband transitions, involving electrons in the conduction band, can be tailored by modifying the confinement potential to achieve very low transition frequencies down to the THz range [47]. The multistage cascade scheme, where electrons in the lower level of the transition cascade down to the higher level of the following quantum well thanks to electric bias, helps to achieve high efficiency proportional to the number of cascade stages. In the mid-infrared range, QCLs can operate at high efficiency at room temperature, reaching peak powers up to 5 W for 5 μm (60 THz) radiation [48]. Devices in the 1-5 THz range operate at cryogenic temperatures (160-190 K). Typical output powers are in the range of a few milliwatts [49], but recently outputs close to 1 W have been demonstrated using large area QCLs [50].
  More recent development include broadband, octave spanning THz QCLs, allowing for frequency comb operation [51] and pulsed emission via active mode locking schemes [52].

- **THz metamaterials**
  Artificially structured electromagnetic materials are a technology borrowed from the microwave regime, but they can be adapted to the THz range thanks to their scalable geometry. Arrays of metallic resonators with sub wavelength gaps - such as Split Ring Resonators - can be used to generate and enhance THz fields [53], to realize optical components like lenses, absorbers, switches [54], and cloaking devices [55], or to reach ultrahigh light-matter interaction coupling regimes [56].

- **Accelerator sources**
  Besides table-top sources, ultrafast THz beams are also available from large accelerating facilities. Intense THz beams can be generated in syn-

chrotrons and particle accelerators from accelerating electron bunches [57], where THz emission can also be used as a diagnostic for the bunch length [58]. Free Electron Lasers can also provide THz beamlines in a frequency range from hundreds of GHz to 50 THz, providing output powers up to a few kilowatts [59],[60].

- **THz high harmonic generation**
  A fascinating novel technique allows to generate ultrabroadband beams with in a spectral range extending from the THz range up to visible light. High harmonics of THz radiation are generated in a similar way to traditional HHG, which normally produces XUV radiation, but in semiconductor crystals instead of in gases: the acceleration of electron bunches during Bloch oscillations in a GaSe crystal can generate a continuous spectrum containing more than 20 harmonics of a 10 THz pulse, reaching up to green visible light [61, 62].

Detection of THz radiation

The THz gap entailed not only a lack of suitable sources, but also of practical detection techniques. While higher frequency MIR radiation can be detected with HgCdTe thermal detectors, photons in the THz range do not carry enough energy to be detected by a liquid nitrogen cooled sensor. Lower frequency radiation can be detected with bolometers cooled with liquid helium [63], which however makes them bulky and slow.
The need for a fast, time resolved detection in the THz range spurred the development of various different techniques. Most of the generation schemes listed above also have an analogue in field detection.
Photoconductive antennas can also be used as detectors [64]: most commercial devices are limited to frequencies lower than 4 THz, but more sophisticated schemes have achieved detection in the 100 THz range [30, 65]. Pumped with fiber laser they are compact and reliable, and are widely employed as detectors for commercial tabletop THz spectrometers. The technology for QCLs can also be used to build Quantum Cascade Detectors [66], and a detection scheme analogous to plasma generation an be implemented exploiting four wave mixing in air or other gases [67].
Electro-optic sampling - developed in 1983 by *Auston and Smith* [68] - corresponds to Optical Rectification: it allows for fully phase resolved, coherent detection of THz and MIR pulses, paving the way for ultrafast THz TDS.

1.2 Phase resolved detection with electro-optic sampling

Electro-optic Sampling (EOS) is a technique which enables fully phase-resolved detection of THz transients by detecting the polarization change in a probe pulse induced by the Pockels effect in a nonlinear crystal.
This section will first briefly describe the Pockels effect, then the limiting factors to detection and the advantages of different nonlinearly active materials. Finally, a typical EOS setup will be described.

The Pockels effect

The linear electro-optic effect [69] describes the change of refractive index displayed in crystals in presence of a strong electric field: the effect can be read out by a probe pulse, whose polarization will change while traveling through the crystal. The effect is exploited to build THz detector: the polarization of a near infrared short pulse is modified when a strong THz beam is present, and the polarization change is linearly proportional to the amplitude of the THz electric field.
The Pockels effect is a second order nonlinear effect. To describe it we relate the crystal polarization to an external electric field through the susceptibility $\chi(E)$ [70]:

$$P = \chi(E)E = (\chi^{(1)} + \chi^{(2)}E + \chi^{(3)}E^2 + ...)E \tag{1.1}$$

The Pockels effect is described by the second order term $P_2 = \chi^{(2)}E^2$. The second order susceptibility is a third- rank tensor $\chi^{(2)}_{ijk}$:

$$P_i(\omega) = \sum_{j,k} \chi^{(2)}_{ijk} E_j(\omega) E_k(0) \tag{1.2}$$

which describes a DC field $E_k(0)$ inducing a polarization P_i at frequency ω.
Since the Pockels effect involves the second order susceptibility tensor, it is present only in non-centrosymmetric crystals. Centrosymmetric materials only exhibit a change of refractive index at higher order, depending quadratically on the applied DC field, which is called quadratic electro-optic effect or Kerr effect.
The strength of the electro-optic effect in a material is usually expressed through the electro-optic coefficient r_{ijk}, which is defined from the power series expression for the dielectric function:

$$\frac{1}{\epsilon_{ij}} = \left(\frac{1}{\epsilon_{ij}}\right)^{(0)} + \sum_k r_{ijk} E_k + ... \tag{1.3}$$

The tensor r_{ijk} must be symmetric in its first two indexes, as is ϵ_{ij}. For ease of notation, it is the usually written in its contracted form r_{ij}. It directly relates the change of refractive index to the applied external field:

$$\Delta\left(\frac{1}{n^2}\right) = \sum_j r_{ij} E_j \tag{1.4}$$

It is related to the second order susceptibility as:

$$r_{ij}(\omega) = -\left(\frac{4\pi}{n_o^2 n_e^2}\right)\chi^{(2)}_{ikj}(\omega) \tag{1.5}$$

where n_o and n_e are respectively the ordinary and extraordinary refractive indexes in the crystal, if birefringent. Otherwise, if it has only one refractive index the expression will involve n^4.

Good electro-optic crystals need to have a large value of r. The most widely used materials are GaP and ZnTe, which crystallize in a zincblende structure with point group symmetry $\bar{4}3m$: for this symmetry group the tensor r_{ij} has only three nonzero component, all with the same value $r_{41} = r_{52} = r_{63}$. For GaP, $r_{41} = 0.97$ pm/V, while for ZnTe $r_{41} = 4$ pm/V, for a probe field at 800 nm.

A non-birefringent material such as ZnTe starts off with only one refractive index n_o for all axes. If however a strong field is present, which we will assume is oriented on the Z axis, then its index ellipsoid becomes:

$$\frac{X^2}{n_o^2} + \frac{Y^2}{n_o^2} + \frac{Z^2}{n_o^2} + 2r_{41}E_z \cdot XY = 1 \tag{1.6}$$

with the X and Y coordinates now coupled together. We can change coordinate system to get back to an ellipsoid with uncoupled coordinates by rewriting:

$$\left(\frac{1}{n_o^2} + r_{41}E_z\right)x^2 + \left(\frac{1}{n_o^2} - r_{41}E_z\right)y^2 + \frac{z^2}{n_o^2} = \frac{x^2}{n_x^2} + \frac{y^2}{n_y^2} + \frac{z^2}{n_o^2} = 1 \tag{1.7}$$

The new refractive indexes along the x and y axes can be defined as

$$n_{x,y} = \frac{n_o}{\sqrt{1 + n_o^2 r_{41}E_z}} \sim n_o \mp \frac{1}{2}n_o^3 r_{41}E_z \tag{1.8}$$

The phase retardation accumulated between the two axes for a probe pulse at wavelength λ traveling through a crystal of thickness d is then:

$$\Gamma = \frac{n_o^3(\lambda) r_{41} d}{\lambda} E_{THz} \tag{1.9}$$

The polarization change induced in the probe pulse is directly proportional to the external electric field: a time dependent THz field can then be reconstructed in amplitude and phase by varying its relative delay to the probe pulse. It is however necessary to choose a suitable probe and EOS crystal.

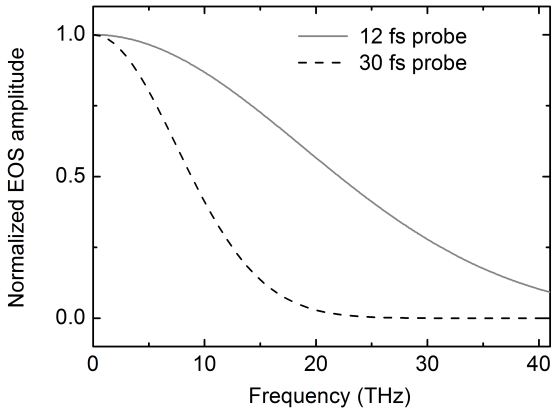

Figure 1.2: Detection bandwidth for different probe time durations: The normalize electro-optic signal amplitude is plotted as a function of the measured radiation frequency for a probe duration of 12 fs (solid grey line) and 30 fs (dashed black line)

Constraints on EOS detection

To fully exploit the potential of the EOS technique, the characteristics of the probe beam and of the nonlinearly active crystal need to be carefully selected in relation to the radiation one wants to characterize. Indeed, the temporal duration of the probe pulse sets a limit on the measurable bandwidth, as do phonon absorptions and velocity mismatch in the electro-optic crystal.

Probe pulse duration For accurate EOS detection, the probe pulse needs to be shorter than the half cycle of the highest frequency in the THz spectrum. In this case, the probe pulse overlaps only with the positive or the negative lobe of the THz transient: the induced birefringence will build up over the entire probe duration to generate a signal proportional to the field amplitude. If on the other hand the probe duration is of the order of half of an oscillation or longer, when the electric field changes sign so does the polarization change induced by the Pockels effect: the overall amplitude of the EOS signal will be decreased.

If we consider a monochromatic wave with central frequency ν_0, sampled by a gaussian probe of duration $\Delta\tau$, the EOS signal amplitude is given by $A = \int dt \cos(2\pi\nu_0 t) e^{-(t/\Delta\tau)^2}$. As shown in Fig.1.2, the signal amplitude decreases at higher frequencies, drastically so for a longer probe duration. In the plot, the dashed black line is the signal amplitude for a 30 fs long probe pulse, such as those coming from an amplified Ti:sapphire laser: at 15 THz, the signal intensity is just 1/10th compared to peak sensitivity at lower frequencies. On

the other hand, for a 12 fs probe - e.g., the ultrafast pulse of an oscillator - the intensity reaches 10% at 40 THz (solid grey line in the plot). Detection in the THz range does not require an ultrashort probe pulse. This, however, becomes a requirement for mid-infrared detection at higher frequencies.

Crystal thickness The thickness of the nonlinear crystal plays a two-fold role in determining the sensitivity and bandwidth: if the probe and THz beam are spatially overlapped, the signal intensity builds up over the entire crystal volume, allowing for accurate detection of weak electric fields. However, since the beams have very different frequencies, their propagation velocities are different. While propagating, the group velocity mismatch (GVM) will build up a delay between the pulses, limiting their effective interaction length. A monochromatic THz wave with central frequency Ω travels trough the electro-optic crystal with a velocity given by the refractive index $n(\Omega)$, while the probe pulse velocity is given by the group index $n^g(\omega_p)$ In a crystal of thickness d the pulses accumulate a delay:

$$\delta(\omega) = \frac{n^g(\omega_p) - n(\Omega)}{c} d \tag{1.10}$$

The response function of the sensor can then be written as [71]:

$$G(\Omega) = \frac{2}{n(\Omega) + 1} \frac{e^{i2\pi\Omega\delta(\Omega)} - 1}{i2\pi\Omega\delta(\Omega)} \tag{1.11}$$

where the first term is the Fresnel factor, accounting for reflections at the crystal surface. The distance over which the pulses are overlapped and the electro-optic signal builds up constructively is the coherence length

$$l_c(\Omega) = \frac{\pi c}{\Omega |n^g(\omega_p) - n(\Omega)|} = \frac{c\lambda_{THz}}{2|v^g(\omega_p) - v(\Omega)|} \tag{1.12}$$

which depends on the mismatch between the group velocity of the probe beam $v^g(\omega_p) = d\omega_p/dk_p$ and the THz beam phase velocity $v(\Omega) = \Omega/k_{THz}$. The electro-optic crystal material should ideally have the lowest possible velocity mismatch at the probe and THz frequency of interest.

If the crystal thickness exceeds the coherence length for a certain frequency, negative interference will reduce the output of the electro-optic crystal. There's a clear trade off between a broad-band detection and long interaction length: for a low frequency pulse, which has a longer coherence length, a thicker crystal will allow signal build up over a larger volume, but detection at higher frequencies will be suppressed by destructive interference. Conversely, a thin crystal will be able to detect over a large bandwidth, but it may display poor sensitivity for lower frequencies.

Crystal	r_e (pm/V)	$\hbar\omega_{TO}$ (THz)	C	GVM (ps/mm)
GaP	0.97	11	-0.47	0.72
ZnTe	3.9	5.3	-0.07	1.3

Table 1.1: Material constants for the most frequently employed electro-optic crystals. [71, 73]. Values are shown for an 800 nm pump.

Phonon absorption and sensitivity Lastly, it is important to consider that many attractive materials with a high electro-optic coefficient also have optical phonons in the THz range. For example ZnTe has a transverse optical phonon at $\omega_{TO} = 5.3$ THz, while GaP has $\omega_{TO} = 11$ THz. Phonon resonances affect the electro-optic coefficient r_{41} [72]:

$$r_{41}(\Omega) = r_e \left(1 + C\frac{(\hbar\omega_{TO})^2}{(\hbar\omega_{TO})^2 - (\hbar\Omega)^2 + i\hbar\Omega\gamma}\right) \tag{1.13}$$

where γ is the phonon resonance damping rate and r_e is the electronic component of r_{41}, constant in the THz range. The Faust-Henry coefficient C represents the ratio between the electronic and ionic components of the electro-optic coefficient. Below the lattice resonance, the two contributions add to each other, however above it the electro-optic coefficient is reduced. A low Faust-Henry coefficient is then highly desirable for broad band detection.

Table 1.1 shows some relevant parameters for EOS detection for ZnTe and GaP, two of the most widely used electro-optic crystals. GaP has a lower velocity mismatch and an optical phonon at higher frequency. However it has a high factor C, which above 11 THz further reduces its value of r_{41}. ZnTe on the other hand has a quite large r_e and a very small Faust-Henry coefficient: its sensitivity is almost identical above and below its phonon band. Inside the reststrahlen band however, its sensitivity is extremely low due to higher velocity mismatch: a thin ZnTe crystal can support large bandwidth detection, but to measure in the 5-8 THz region a different detector, such as GaP, needs to be used.
Other crystals such as GaSe or the organic crystal DAST also have interesting electro-optical properties, however their birefringence makes them unpractical as detector materials.

Electro-optic sampling detection setup

A EOS set-up requires a THz and a NIR probe beam tightly focused together on a suitable crystal, and a detection scheme to measure the change in polarization in the probe. Fig.1.3 shows schematically how the EOS scheme is implemented in our set-up.

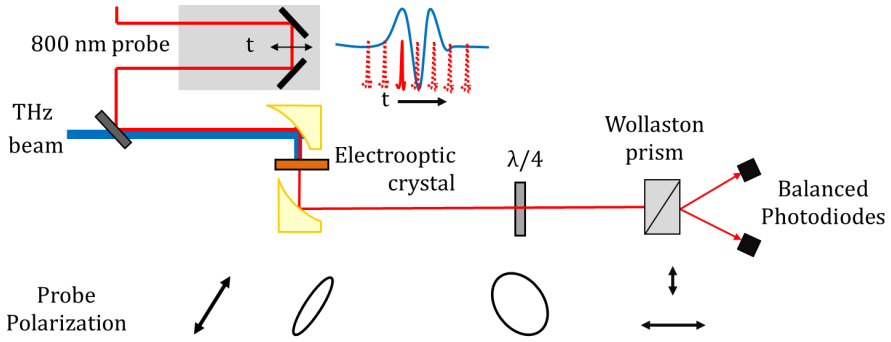

Figure 1.3: Schematic representation of an EOS scheme. A strong THz/MIR pulse shines on an electro-optic crystal such as ZnTe. A probe pulse much shorter then the pulse to be measured is focused on the same spot at a variable time delay, allowing for temporal scanning of the infrared pulse. Due to the Pockels effect, the EOS crystals displays induced birefringence, turning elliptical the initially linear polarization of the probe pulse. A quarter wave-plate rotates the polarization in the complex plane, distinguishing left-handed and right handed polarizations. The probe is then split by a Wollaston prism in two linearly polarized component, which are then detected by ultrafast photodiodes: measuring the difference between the intensity on the two axes allows to retrieve the MIR electric field from the magnitude of the change in polarization

We use an 800 nm probe short enough for the highest THz frequency to be measured, i.e. a 30 fs pulse for low frequency THz or an ultrafast 12 fs oscillator pulse to measure higher MIR frequencies. The probe travels on a precision delay stage, varying the temporal overlap with the THz pulse and allowing for scanning of the electric field with sub-fs resolution.
To ensure spatial overlap on the EOS crystal, both the probe and the THz beam are focused by a Gold parabolic mirror: all beams hitting the mirror parallel to its axis are focused together in the parabola focus, regardless of their wavelength and without spherical aberrations. A second matching parabolic mirror restores the probe to a collimated beam for transport to the detector.
The probe is at first linearly polarized: if it does not overlap with the THz beam on the EOS crystal its polarization remains unchanged, but in the presence of a strong THz field the acquired additional component turns its polarization elliptical. Before reaching the detector, it passes through a series of optics meant to separate the components of the elliptical polarization.
First it passes through a $\lambda/4$ plate, which rotates the polarization components of $\pi/2$ in the complex plane: the effect on an elliptical polarization differenti-

ates between left- and right-handed pulses, allowing to distinguish the sign of the Pockels effect, and in turn that of the THz field. Linearly polarized light becomes circularly polarized. Next, a Wollaston prism separates the beam in two components, polarized linearly either parallel or perpendicular to the prism axis. The $\lambda/4$ plate axis orientation is chosen so that a linearly polarized probe is split in two components of equal intensity. Finally, the two beams are focused on a couple of fast balanced photodiodes, which measure the difference between their intensity.

Using a circularly polarized probe it is also possible to implement polarization-sensitive EOS [74]: in a [111] oriented ZnTe crystals both polarization components of the probe, each sensitive to a corresponding THz polarization, can be detected with equal efficiency. A half wave plate before the Wollaston prism allows to select which component is to be measured without adjusting the crystal orientation or the alignment.

If the probe beam is taken from the oscillator in order to measure in the MIR range, it is necessary to synchronize the EOS measurement on the probe (85 MHz repetition rate in our system) with the amplifier pulses generating the THz (1 kHz). The previous oscillator pulse, which did not interact with the THz beam, is measured as a reference and subtracted from the signal to reduce shot noise from intensity imbalances in the two photodiodes [35]. If the probe pulse comes from the amplifier itself, then synchronization is automatic provided that the probe beam path is equal to that of the THz beam. For noise reduction, a chopper can be installed on the THz beam line blocking every other pulse, in order to obtain blank probe pulses to be used as a reference.

Since the Pockels effect is linear, the difference can be used to extract the THz field amplitude:

$$\frac{I_1 - I_2}{I_1 + I_2} = \sin(\Gamma) = \sin\left(\frac{2\pi l_c}{\lambda_p}(n^g(\omega_p))^3 r_{41} E_{THz}\right) \tag{1.14}$$

The THz electric field can then be reconstructed both in amplitude and phase, up to an arbitrary sign. If a thin EOS crystal is used, such that the crystal thickness d is shorter than the coherence length for all involved frequencies, then $l_c = d$: the detector is calibrated to accurately measure E_{THz} in kV/cm.

1.3 THz and mid-infrared generation by nonlinear optical processes

In this section the methods for generating THz radiation by optical interaction in nonlinear crystals will be discussed. The first section will focus on generation

by Optical Rectification (OR) in a range up to 5 THz, then phase-matched difference frequency generation (DFG) in the mid-infrared range will be discussed, and finally more recent development in broadband THz generation in organic crystals will be presented.

1.3.1 Collinear optical rectification

Optical Rectification, the generation of DC or low frequency radiation, was first demonstrated in KDP [75] for a DC electric field, and later on it has been widely employed for the generation of free-space THz beams from a wide range of materials [33]: THz emission has been reported from many different semiconductors such as ZnTe, GaP, GaSe, CdTe, Te, InP and GaAs, nonlinear crystals like $LiNbO_3$, metals, and more recently organic crystals such as DAST. Optical rectification can be described as the other side of the coin of the Pockels effect: instead of having a DC field mixing with a probe a frequency ω to create a polarization at the same frequency, here we consider two electrical fields very close in frequency giving rise to a quasi-DC polarization:

$$P_i(\Omega) = \int \sum_{j,k} \chi_{ijk}(\Omega) E_j(\omega) E_k^*(\omega + \Omega) d\omega \tag{1.15}$$

Here we called $\Omega = \omega_1 - \omega_2 \to 0$ the target THz frequency.
Different materials, having different polarizabilities, will display stronger or weaker OR: usually however the strength of the effect is not given in terms of $\chi^{(2)}$ but of the electro-optic coefficient r_{ijk}, as:

$$P_i(\Omega) = \int \sum_{j,k} \frac{1}{2} n_i^2(\omega) n_j^2(\omega) r_{ijk} E_j(\omega) E_k^*(\omega + \Omega) d\omega \tag{1.16}$$

The effective nonlinear coefficient is be defined as $d_{eff} = n^4 r/4 = \chi^{(2)}/2$ Typically OR is achieved by having different frequencies in the spectrum of an infrared pump pulse: the broader the pump bandwidth, the higher THz frequency it will be capable of generating. However to achieve an efficient generation, the THz components generated in different points of the nonlinear crystal by the propagating pump need to interfere constructively with each other. The phase matching condition $\Delta k = k(\Omega) - k(\omega + \Omega) + k(\omega) = 0$ for $\Omega \ll \omega$ can be written in terms of velocity matching:

$$k(\Omega) = \partial k / \partial \omega|_{\omega_p} \Omega \longrightarrow v(\Omega) = v^g(\omega_p) \tag{1.17}$$

Here $v(\Omega)$ denotes the phase velocity for the THz and $v^g(\omega_p)$ the group velocity at the pump infrared frequency. The coherence length over which THz radiation

Crystal	r_{ij} **(pm/V)**	d_{eff} **(pm/V)**	$\mathbf{n}(\omega_p)$	$\mathbf{n}^g(\omega_p)$	$\mathbf{n}(\Omega)$	α **(cm^{-1})**
ZnTe	3.9 (r_{41})	68.5	2.87	3.13	3.17	1.3
GaSe	1.7 (r_{22})	28	2.85	3.13	3.27	0.07

Table 1.2: Relevant parameters for THz generation by OR by an 800 nm pump. The values of $n(\Omega)$ and α are given at 1 THz. [76]

builds up constructively can then be defined as:

$$l_c = \frac{\pi}{\Delta k} = \frac{c}{2\Omega(n(\Omega) - n^g(\omega_p))} \tag{1.18}$$

A long coherence length allows to use thicker crystals, building up a higher THz field. Efficient THz generation also requires low absorption in the THz range, a large electro-optic coefficient and no significant pump absorption.

Some semiconductor crystals naturally fulfill the velocity matching condition when pumped with a Ti:sapphire 800 nm beam: in particular ZnTe has almost identical values for the THz refractive index and the group refractive index at 800 nm. As we have see, ZnTe has a large electro-optic coefficient r_{41}, but it displays 2-photon absorption at 800 nm, generating free carriers which increase THz absorption [2]: for optimal operation at 800 nm, the pump intensity must be kept low enough to avoid multiphoton interaction. Using a lower frequency pump beam avoids this issue, but at cost of automatic phase-matching: at 1 THz, phase matching can be achieved using a 1.6 μm pump in a tilted pulse front propagation scheme, using a contact grating on the ZnTe crystal to maintain the collinear THz propagation emission [77].
Another widely used crystal is GaSe, a negative uniaxial crystal: at normal incidence, with the propagation direction parallel to its optical axis, it also features quasi-phase matched generation. Furthermore it has very low absorption coefficient α in the THz region, and due to its high band gap of 2.2 eV it does not display any multi-photon absorption of the pump. GaSe has an hexagonal symmetry ($\bar{6}2m$ point group symmetry), so its only relevant nonlinear optical coefficient is d_{22}, which has quite a large value $d_{22} = 54$ pm/V. Some significant crystal parameters for generation at 1 THz in GaSe and ZnTe are collected in Tab.1.2.

In our setup we used both GaSe ([001] oriented) and ZnTe ([110]) pumped with a broad band amplified Ti:sapphire beam with an energy of 1 mJ per pulse. A schematic view of the setup is shown in Fig.1.4.(a): to optimize THz generation the 800 nm pump pulse was sent through a pulse shaper during the amplification process to obtain a super-gaussian spectral shape with a 60 nm

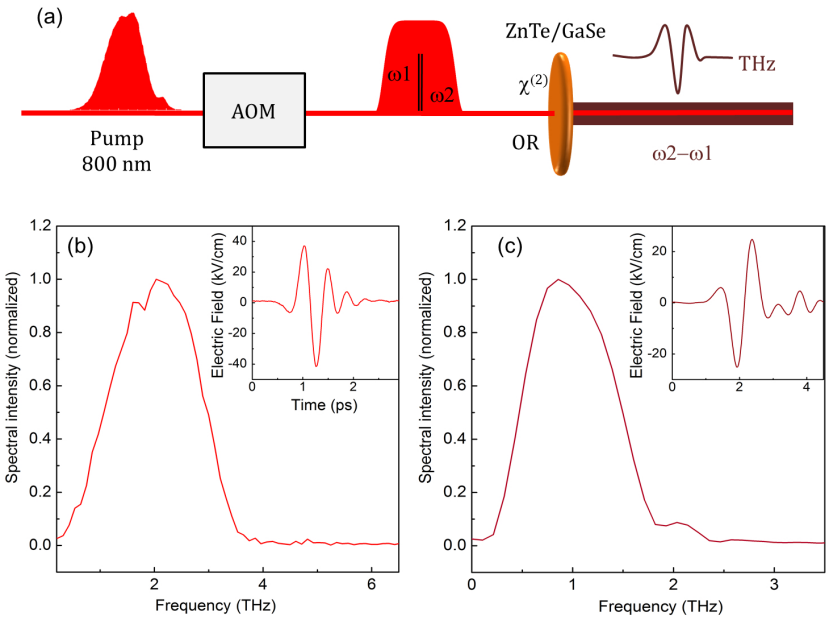

Figure 1.4: (a) Schematic of THz generation by Optical Rectification: a super-gaussian amplified 800 nm pump shines on a thick GaSe/ZnTe crystal, where THz radiation is generated by mixing frequencies close together in the pump spectrum (b) Spectrum of 2 THz radiation generated in GaSe and corresponding electric field transient (inset) (c) Spectrum of 1 THz radiation generated in ZnTe and corresponding electric field transient (inset)

bandwidth, so that the spectral components interacting through OR would all have equal intensity.

The amplified beam, with an energy per pulse of 1 mJ, shines on a nonlinear crystal at normal incidence, generating high-field THz pulses. Some typical spectra generated in GaSe and ZnTe are shown in Fig.1.4.(b) and (c) respectively: a 500 μm thick GaSe produces a beam centered at 2 THz, with a 2 THz bandwidth (FWHM), while ZnTe (1 mm) generates a 1 THz FWHM spectrum centered around 1 THz. The electric field transients, measured in an EOS setup with a 300 μm ZnTe detecting crystal, are shown in the insets. The field amplitudes achieved in our set-up are fairly high for the low-frequency THz range: the large surface area of the crystal we use allows us to shine a relatively high pump intensity (up to 1 mJ per pulse) while still avoiding thermal damage, while a thick generating crystal can be used to build up a larger THz field over its whole volume thanks to velocity matching.

1.3.2 Phase-matched DFG in GaSe

Due to limitations in velocity matching, OR in a collinear geometry is only a suitable generation scheme for low THz frequencies. However, exploiting GaSe birefringence it is possible to achieve phase matched generation in the MIR range up to 70 MHz [34]. These schemes are based on phase matched Difference Frequency Generation (DFG) of pump beams at different central wavelengths: the MIR central frequency can be tuned by changing the orientation of the GaSe crystal [78, 79].

GaSe is a negative uniaxial crystal: it has one optical axis coinciding with its $\hat{z}$ axis, orthogonal to the [001] surface. Its ordinary refractive index is larger then the extraordinary, taking the values $n^o = 2.883$ and $n^e = 2.502$ at 800 nm [80]. An incident beam, polarized perpendicular to the plane containing the propagation direction $\hat{k}$ and the optical axis $\hat{z}$ will follow the ordinary refractive index, while a beam polarized in the $\hat{k}$ - $\hat{z}$ plane will see the extraordinary index.

Our generation scheme is based on type I phase matching, where two pump beams polarized one on the extraordinary and one on the ordinary axis produce an ordinary MIR beam by difference frequency mixing. The phase matching condition $\Delta k = 0$ reads:

$$n^o(\Delta\omega) \cdot (\Delta\omega) = n^e_\theta(\omega + \Delta\omega) \cdot (\omega + \Delta\omega) - n^o(\omega) \cdot (\omega) \tag{1.19}$$

Here $\Delta\omega$ is the generated MIR frequency.The extraordinary beam, polarized in-plane, propagates at an angle θ with respect to the optical axis, so that the refractive index n^e_θ is given by $(1/n^e_\theta)^2 = \sin^2\theta/(n^e)^2 + \cos^2\theta/(n^o)^2$. By rotating the GaSe crystal around its $\hat{x}$ axis phase matching conditions are fulfilled for a different value of $\Delta\omega$: this allows for tuning the generated MIR frequency. Due to the high refractive index of GaSe, the maximum tuning angle is $\sim 20°$, which corresponds to a maximum MIR frequency of.

The relevant nonlinear optical coefficient for GaSe ($\bar{6}2m$ group) is $d_{22} = n^3 r_{22} =$ 54 pm/V, which connects polarizations on the $\hat{x}$ and $\hat{y}$ crystal axes. The effective nonlinearity d_{eff} for type I phase matching is then [79]:

$$d_{eff} = -d_{22}\cos(\theta)\sin(3\phi) \tag{1.20}$$

Here ϕ is the azimuthal rotation angle, set to maximize the effective nonlinear coefficient. The polar angle θ, which for maximum DFM generation should be set to zero (pump propagation in the y-z plane), is used to set the output frequency via angle tuning.

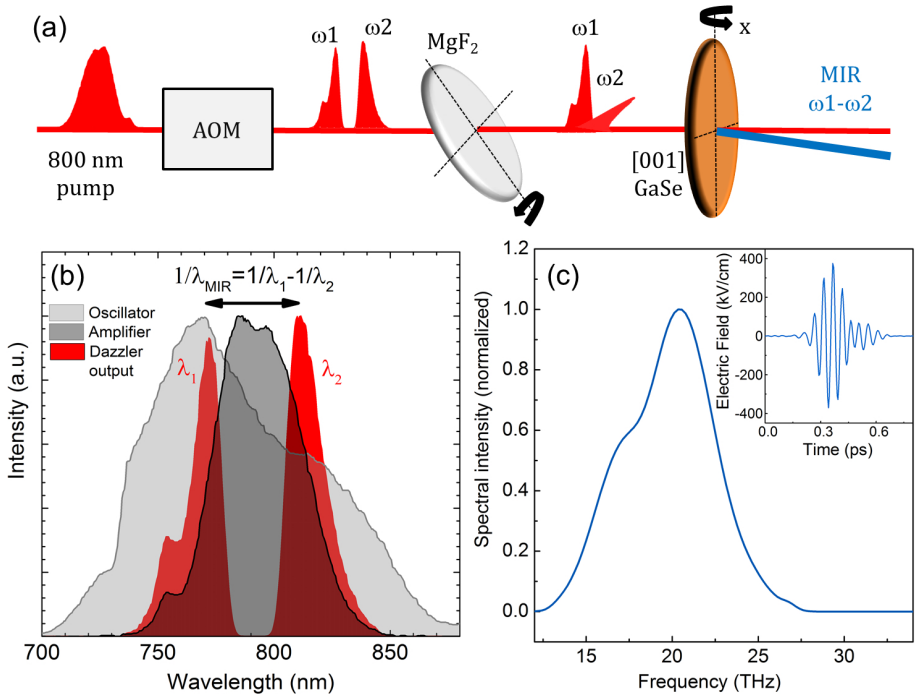

Figure 1.5: (a) Schematic of mid-infrared generation by DFM in GaSe: the pump pulse in the amplifier goes through an acousto-optic modulator, which suppresses the central wavelengths in the pulse leaving two peaks split up in both time and frequency. The frequency gap corresponds to the target MIR generated frequency. A birefringent MgF_2 plate introduces a frequency dependent phase delay so that on exiting the plate the two pump spectral component are cross-polarized and overlapped in time. The pump shines on a tilted [001]-cut GaSe crystal and generate MIR radiation by DFG: the between its optical axis and the pump propagation direction is chosen so that type I phase matching is achieved for the two cross polarized pump components and the MIR field polarized on the crystal ordinary axis. (b) Double-peaked spectrum of the amplifier pulse, after pulse shaping in an acousto-optic modulator (red), compared with the input oscillator spectrum (light grey) and the spectral shape of the amplified pulse without the AOM (dark grey) (c) Spectrum of 20 THz radiation generated in GaSe and corresponding electric field transient (inset)

To efficiently generate a desired MIR frequency, the two cross polarized pump components should be separated in frequency by that same $\Delta\omega$. It is possible to use two separate beam and use e.g. an OPA system to tune the pump frequency; in our set-up however we use a *DAZZLER* acousto-optic modulator

(AOM) pulse-shaper [81] placed before the amplifier cavity to select the wings of an 800 nm amplifier pulse (see Fig.1.5). In the AOM an acoustic wave form is sent through a TeO_2 piezoelectric transducer: the density modulation creates a time dependent diffraction grating, so that the transmitted output pulse has a specified spectral and temporal phase. The DAZZLER is set to create a spectrum with two peaks so that $1/\lambda_{MIR} = 1/\lambda_1 - 1/\lambda_2$: a typical spectral shape of the pump pulse - optimized for 20 THz generation - in shown in Fig.1.5).(b). The higher orders of the spectral and temporal phase are set to optimize the MIR output.
In order to have type I phase matching, the two spectral components must be cross-polarized: a [001]-oriented MgF_2 half wave plate is used to rotate the polarization of the high frequency component to have it propagate along the GaSe extraordinary axis. The plate is tilted 45° around its optical axis, and by an angle ϕ around its $\hat{x}$ axis. This ensures that the pump polarization is split equally on the ordinary and extraordinary axes, while the choice of ϕ sets the phase retardation between the two spectral components to π. To ensure that the two components are overlapped in time in the GaSe crystal, the delay added by the MgF_2 plate is precompensated using the AOM.
To summarize, the pump pulse consists of two cross-polarized spectral peaks separated by the target MIR frequencies, which shines on a [001] GaSe crystal tilted at an angle θ set by phase matching conditions. To tune the output center frequency, a few parameters need to be changed accordingly: the GaSe tilt, the MgF plate orientation ϕ, the spectral and temporal separation between the pump peaks created by the *DAZZLER*. The MIR beam emerges from the GaSe polarized along its ordinary axis (i.e. along the vertical $\hat{x}$ axis), and propagates on the $\hat{z}$ axis, non-collinearly with the generated pulse.
An output spectrum centered at 20 THz is shown in Fig.1.5).(c), with the measured electric field transient shown in the inset: the FWHM of this particular spectrum is 5 THz, generated using a 100 μm thick GaSe crystal. Choosing a thin generating crystal ensures broadband generation, while the more stringent phase matching conditions imposed by a thicker crystal result in a narrow spectrum. At full pump power field amplitudes of the order of MV/cm can easily be achieved.

1.3.3 Ultrabroadband THz pulses in organic crystals

The generation schemes discussed for ZnTe and GaSe require phase matching to achieve generation of high electrical fields. However, if a generating crystal displays extremely large nonlinear coefficients, high output fields can be achieved

even in a very small coherence length, thus making phase matching unnecessary. Crystals grown from organic salts of stilbazolium and sulfonate were developed specifically to show very large molecular polarizabilities [82], which could be exploited for THz generation. Such organic crystals have proven to be challenging to grow with adequate control of thickness and optical quality, but recently thanks to improvements in the growth technology they have become more widely available [83].

Organic crystals like DAST [84] and DSTMS [85] have been shown to have very attractive characteristics: in particular the have an extremely high electro-optic coefficient (r_{11} = 77 pm/V at 785 nm, compared to r_{41}=4 pm/V for ZnTe) but also display non-negligible absorption in the THz range [86, 87]. They can generate extremely high fields (of the order of hundreds of kV/cm) at low THz frequencies when pumped with OPA systems or appropriate lasers between 1200 and 1600 nm [88–90]. Another organic crystal, OH1 [91], has comparably high nonlinear optical constants (r_{33} = 75 pm/V at 785 nm), but presents more favorable growth characteristics [92],[93]. Compared to DAST and DSTMS, which are monoclinic crystals (point group m), OH1 is an orthrombic crystal (*mm2*): since its dielectric axis coincide with the crystallographic axis, it is easier to grow at the correct orientation. Furthermore, while DAST and DSTMS have an optical phonon at 1.1 THz, in OH1 the absorption at this frequency is lower (with a smaller absorptive feature at 1.7 THz), making it more suited for generation at low frequencies.

Research has been focused mostly on generation below 5 THz, where OH1, DAST and DSTMS can generate light in quasi phase-matched conditions [3]. Early attempts at pumping at 800 nm with a Ti:sapphire pump showed potential for much more broad band generation up to 15 THz [94].

Recently, we developed a technique for generating ultrabroadband pulses, spanning from 0.5 to 30 THz, by pumping organic crystals with a properly tailored pump beam [20]. The amplified 25 fs Ti:sapphire beam at 800 nm have a bandwidth of 22 THz at the FWHM, and of 40 THz at 1/10th of the maximum, allowing for broadband MIR generation by DFG. Using a DSTMS crystal, grown by *Rainbow Photonics* on the [001] surface and polished to 0.35 mm, we achieved a peak electric field value of 800 kV/cm.

In Fig.1.6.(a) is shown the field generated with a 0.35 mm OH1 crystal ([100] surface) with a pump energy of 200 μJ, far from the crystal damage threshold ($\sim$ 100 GW/cm^2). Overall, the bandwidth generated in such organic crystals spans five octaves.

To shape the pump pulse we used a *DAZZLER* AOM, choosing a supergaussian

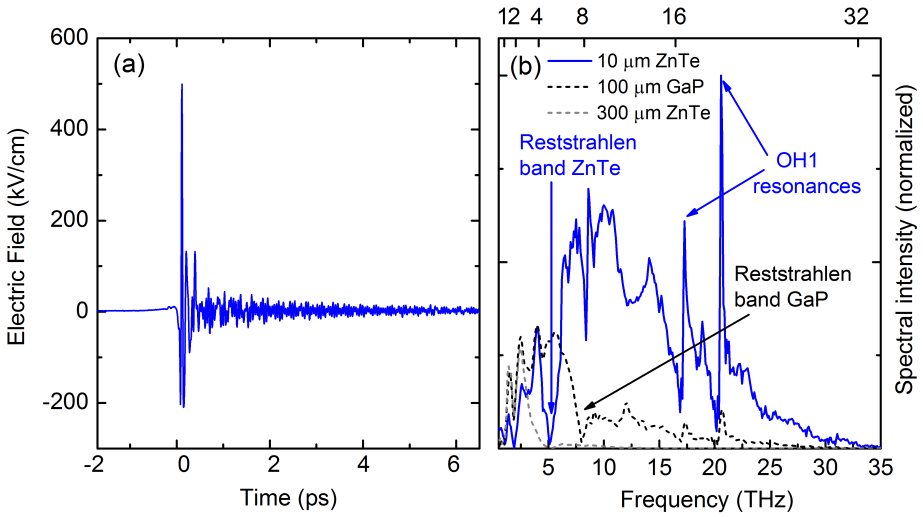

Figure 1.6: (a) Electric field generated by the organic crystal OH1 pumped with 800 nm radiation (thin ZnTe as a detector) (b) OH1 spectrum spanning 5 octaves, measured with different detectors to fill the gaps left by ZnTe and GaP reststrahlen bands. The blue curve has been measured with a thin 10 μm ZnTe crystal, the dashed black curve with a 100 μm GaP, and the dashed grey curve with 300 μm ZnTe.)

spectrum and adjusting the higher order spectral phase. The pulse spectral density is shown in Fig.1.6.(b): the blue curve was measured using a thin 10 μm ZnTe crystal as a detector, to ensure a large detection bandwidth. It clearly shows to large peaks at 16.2 THz and 20.6 THz, which correspond to resonances in the generating crystals (both DAST and DSTMS show similar features at these frequencies). These narrow resonances result in a strong and long lived emission, lasting for 6 ps and showing a beating pattern from the interference of the two components. Acting on the pump spectral phase, it is possible to enhance these features, increasing the peak field amplitude, or suppress them favoring the generation of lower frequencies.

The thin ZnTe detection crystal is less sensitive in the low THz range, since spectral components with longer wavelength can not build up a strong electro-optic signal in the 10 μm active layer. Further more, the ZnTe reststrahlen band prevents detection in the 5-8 THz range. In Fig.1.6.(b) we also show measurements performed with different EOS crystal to overcome these limitations: the dashed grey line is acquired with a 300 μm thick ZnTe, which is extremely sensitive at 1-2 THz, but can not measure in the MIR range due to destructive interference of the EOS signal over the crystal length. The dashed black line

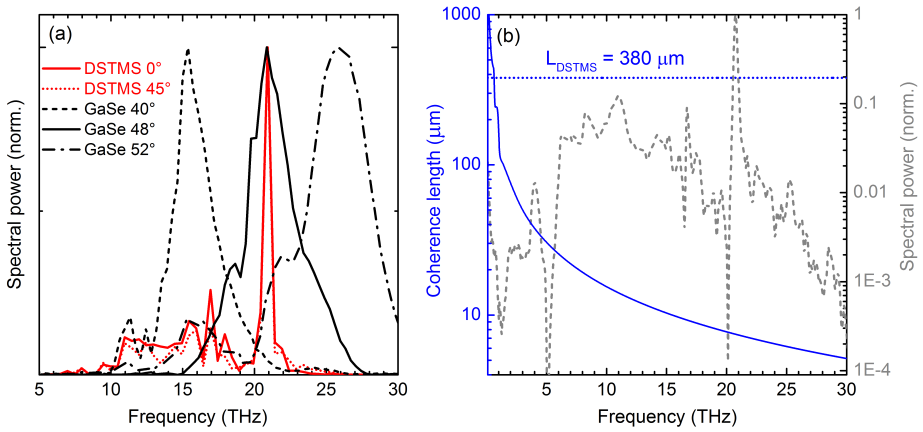

Figure 1.7: (a) Generated spectrum by GaSe (black) and DSTMS (red) for different pump incidence angle. For DSTMS the spectral output is nearly identical at 0° (solid line) and 45° (dotted line), while for GaSe the peak emitted frequency shifts from 21 THz at 48° (solid line) to 15 THz at 40° (dashed line). (b) Coherence length in DSTMS pumped at 800 nm as a function of frequency (solid blue line, left axis), compared to the emitted spectral power (dashed grey line, right axis). The dotted blue line marks the thickness of the DSTMS crystals: it is larger then the coherence length for all frequencies above 1 THz, where the emitted spectral power is larger.

shows a measurement with 100 μm GaP to cover the reststrahlen band; however GaP own phonon absorption falls between 7 and 9 THz, strongly reducing the crystal sensitivity above it.

Non phase matched generation

Contrary to DFG in crystals like GaSe, octave-spanning generation in organic crystals is not based on a phase matched process. Indeed, the spectral intensity generated in OH1 and DSTMS is independent from the pump incidence angle in the crystal: Fig.1.7.(a) shows in red the emission from a DSTMS crystal as a function of frequency, normalized to its highest peak at 21 THz. The solid line corresponds to normal pump incidence and the dotted line to a 45° incidence angle: their output spectra are nearly identical, the main difference being an overall loss of power at 45° due to reduced effective surface.

On the other hand pump incidence angle is a critical parameter for phase matched generation. In the same panel, the black lines represent the spectrum generated from GaSe for different tilt angles (respectively 40° as a dashed line, 48° as a solid line and 52° as dashed-dotted): changing the angle tunes the

peak output frequency from 15 THz to 26 THz.
Furthermore, phase matched generation occurs inside the coherence length for each frequency: for efficient generation, the nonlinear crystal should be thinner than the coherence length in the region over the whole generation bandwidth. If it is longer then the coherence length for a spectral component, destructive interference strongly reduces the output.
The coherence length for THz generation in DSTMS pumped at 800 nm has been calculated according to:

$$l_c = \frac{c}{2\Omega(n(\Omega) - n^g(\omega_p))} \tag{1.21}$$

with $n^g(\omega_p) \sim 2.8$ at 800 nm [85] and $n(\Omega) \sim 2.2$ in the THz range [86]. The result is plotted as a blue solid line in Fig.1.7.(b). The coherence length exceeds the crystal thickness of 380 μm only for frequency below 1 THz, where the DSTMS spectral output (shown as a dashed grey line) is less the 1% of the peak. Above 15 THz, where emission is most intense, the coherence length is less then 10 μm: phase-matched generation can not support the large spectral bandwidth of DSTMS and similar organic crystals. However the large second order nonlinearity $d_{11} = 214$ pm/V allows to achieve a high spectral intensity even over such a short interaction length.

Chapter 2

Broadband THz absorption spectroscopy of water and hydrated biomolecules

Organic crystals can be used to achieve very high field strengths. When pumped at 800 nm, they offer a huge bandwidth, albeit with a somewhat complicated spectrum which is reflected in a quite structured and long lasting temporal shape of the electric field. However, such broadband pulses can be exploited for many interesting spectroscopic applications: in this section results on linear absorption spectroscopy of bulk and interfacial water will be presented.
First, we present a linear absorption spectrum of bulk liquid water collected in a single measurement, well reproducing results found in literature. Furthermore, DNA hydration has been studied to assess how hydrogen bonding of water molecules with phosphate groups on the DNA backbone influences the full water librational spectrum. Experiments with confined water in reverse micelle structures of different sizes confirm our interpretation of the DNA spectrum.

2.1 Water absorption spectrum up to 30 THz

Water in its bulk liquid state consists of a network of hydrogen bonded molecules arranged in a well known geometry: each molecule forms on average four hydrogen bonds, two through the donor OH group and two through the accepting oxygen atom [95]. This arrangement is dynamic, with bonds breaking and reforming as the molecules undergo fluctuating torsional motions.
The absorption spectrum of bulk liquid water in the infrared region is very well

established in literature: spectra from the microwave up to the visible range (1 cm^{-1} to 15000 cm^{-1}) have been acquired by different measuring techniques, tested for accuracy and reproducibility and collected together [96]. The main spectral features in the spectral range from 1 THz to 30 THz are summarized in Tab.2.1.

In the IR range, the most prominent effects are bending and stretching of the OH bonds, respectively around 50 THz and 100 THz (1600 and 3300 cm^{-1}).
For the 1 THz - 30 THz spectral region, *Zelsmann et al., 1995* [97] have reported the spectra of water and deuterized water (D_2O) for different temperatures. Water spectral features in this range stem from intermolecular motions affecting the hydrogen-bond network: bending of the O-H-O hydrogen bonds appears around 1.5 THz, O-H-O stretching peaks at 5.5 THz, while the strongest absorption band, at 20 THz, is due to molecular librations. Librations are rotational motions hindered by the hydrogen bond network, which makes them a very sensitive probe of its structural changes: as shown in Ref.[98], excess energy from the excited OH1 bending mode (1650 cm^{-1}) is transferred to the librations, which are then red-shifted. In general, weaker hydrogen bonds will shift the librational absorption peak to lower frequencies due to the lower force constants involved, while stronger bonds with a higher force constant will result in a blue shift.

Zelsmann's spectra for bulk water at room temperature is shown in Fig.2.2 as a solid black line. These results however have only been measured up to 20 THz, while the decreasing slope of the L2 peak has been reconstructed by fitting the measured peak. Direct measurements of the other slope are in good agreement [99], but data had to be collected in different setups. Using organic crystals as a broadband THz source we are able to acquire the whole libration spectrum in a single run.
The setup for broadband linear absorption measurements is schematically shown in Fig.2.1.(a): the pump beam comes from a Ti:sapphire amplifier laser system,

Attribution	**Frequency**	**Wavenumber**	**FWHM**
Hydrogen bond bending B	1.5 THz	50 cm^{-1}	80 cm^{-1}
Hydrogen bond stretching S	5.5 THz	183.4 cm^{-1}	148 cm^{-1}
Libration L1	11.8 THz	395.5 cm^{-1}	300 cm^{-1}
Libration L2	20.6 THz	686.3 cm^{-1}	344 cm^{-1}

Table 2.1: Bands in the bulk liquid water spectrum up to 30 THz [97]

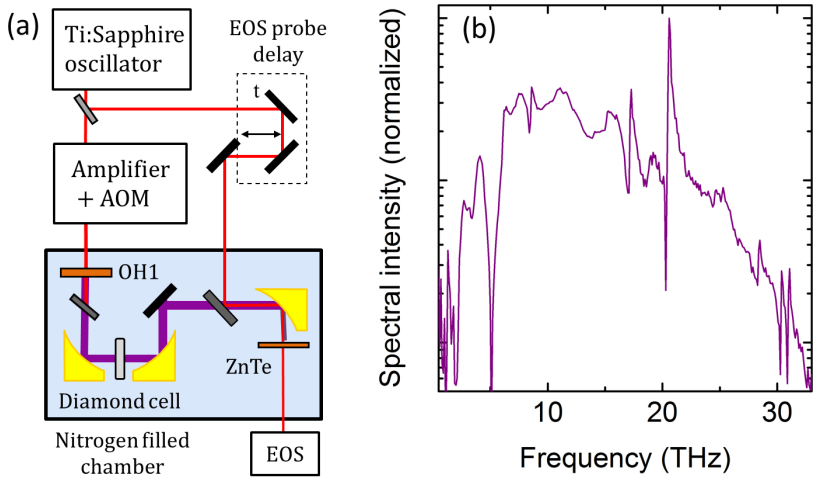

Figure 2.1: (a) Setup for broadband linear absorption measurement: radiation generated in an organic crystal is focused on a diamond cell by a couple of parabolic mirrors; transmitted radiation is measured by EOS. (b) Broadband OH1 spectrum transmitted through diamond windows.

including a *DAZZLER* AOM used as a pulse-shaper set to optimize mid-infrared generation. For this set of measurements we used the organic crystal OH1 as a source. Minding the organic crystal damage threshold, the pump energy on its entrance surface was limited to 200 μJ. The broadband radiation is measured in an EOS scheme, using a thin (10 μm) ZnTe crystal as an active medium. All measurements were carried out in a nitrogen atmosphere to avoid absorption originating from water vapor and CO_2 in air.

To hold our sample we used a commercial diamond window cell (from *Diamond Materials*): since diamond has an extremely flat dispersion curve in the THz and MIR range [100], the windows don't affect the spectral shape of the transmitted pulse. The window were chosen 450 μm thick to avoid reflection on the windows creating pulse replicas in our measuring time frame. Losses due to reflections on the windows amount to $\sim 70\%$ of the electric field in the beam focus. A typical spectrum transmitted through the empty diamond cell is shown in Fig.2.1.(b) in logarithmic scale.
The two diamond windows were separated by 16 μm Mylar spacers and filled with distilled water at room temperature. Absorbance is calculated as $A = -\log_{10} I/I_0$, by comparing the transmitted intensity with a reference taken on empty the diamond cell. Figure 2.2 shows the fitted spectrum by Zelsmann, together to our results using OH1 as a source. We observe very clearly the hy-

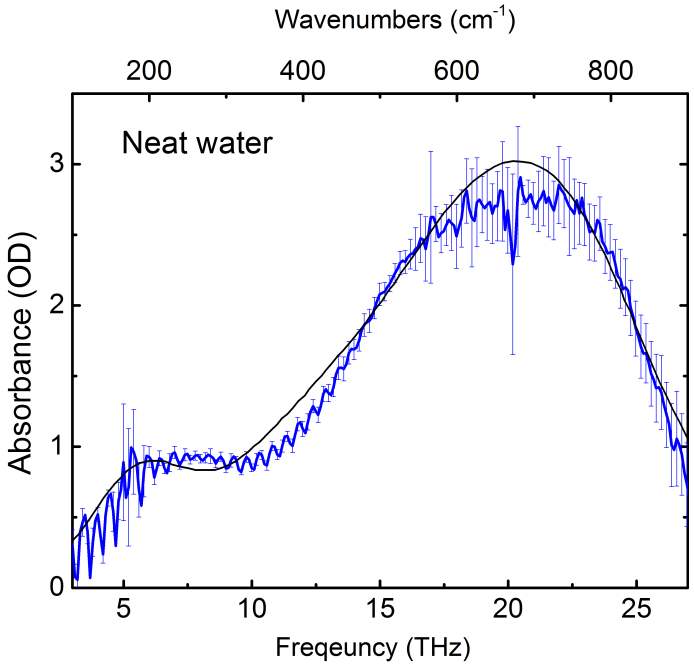

Figure 2.2: Absorbance (in Optical Densities) of 16 μm of neat water in the 3-27 THz range (blue line), compared to a spectrum from literature [97]

drogen bond stretching and librational bands, matching the peaks position and width established in the literature. However, we are able to measure up to 30 THz, fully resolving the downward slope of the L band. Higher noise level close to 20 THz is due to the OH1 generation resonance, while the ZnTe reststrahlen band reduces the sensitivity around 5 THz.

2.2 Water confined in DOPC reverse micelles

In bulk water, the hydrogen bonds fix the molecules orientation in an interconnected network: the resulting range of motions determines the features of the neat water spectrum. For interfacial water however the normal hydrogen bond network is disrupted, modifying the water molecules orientation and motions. Understanding the properties of interfacial and trapped water is extremely important for the study of hydrated samples: indeed, large biological molecules like DNA or proteins are only functional in water solution, and molecular interactions are mediated by their highly heterogeneous hydration layer.
Reverse micelles (RMs) are used as model systems to study confined and in-

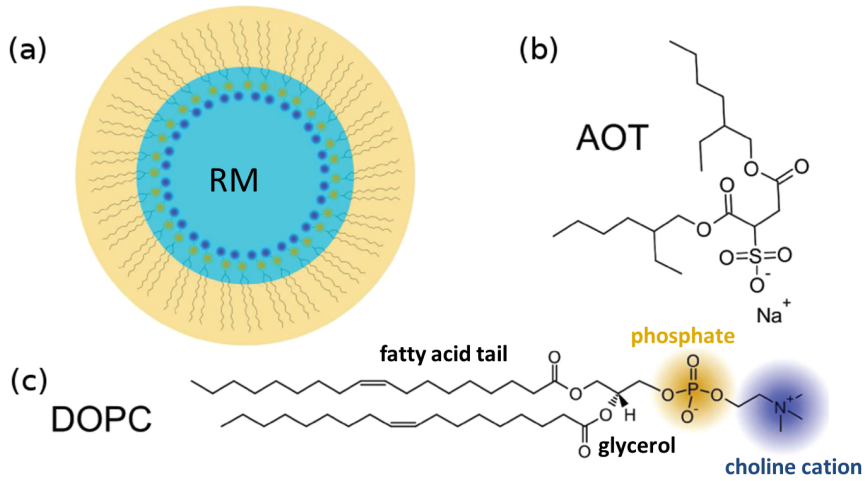

Figure 2.3: Water confined in a reverse micelle structure, and different surfactant heads. AOT has an anionic SO_3^- group with a sodium counterion, while DOPC has a PO_4^- group covalently bound to a choline counterion.

terfacial water, by isolating water nanodroplets inside a layer of surfactant molecules [101]. Fig.2.3.(a) shows a scheme of a reverse micelle structure: the water molecules are confined in a spherical structure by the micelles' polar head groups, while the long hydrophobic tails of the surfactant are pointing outward. Large RMs, containing many water molecules per charged head group, show a behavior similar to bulk water, since molecules are shielded from the charged groups by the hydrogen bond network. Smaller droplets, where most molecules are bonded to charged ions, show significant spectral changes [102].

An ample body of work has focused on AOT surfactant molecules (2.3.(b)), since they easily form stable RMs: AOT has a SO_3^- negatively charged group solvated in the water volume with a Na^+ counterion, creating a highly polar hydrophilic surface. Absorption spectroscopy has revealed that AOT RMs of increasingly small size (from 23 down to 10 $\AA$) show a marked red shift of the water L2 peak [103] from 20 to 15 THz, which has been explained in terms of the polar head groups trapping the first layer of water molecules, while the bulk-like droplet center has an almost unperturbed hydrogen bond network [102, 104].
Another family of surfactant molecules able to form reverse micelles are phospholipides. Since they are a major component of cellular membranes, their bonding to water molecule is of keen interest, and they have been extensively studied in the IR range as model systems for the phosphate heads on DNA backbone [105–107].

The DOPC molecule (2.3.(c)) has a hydrophobic fatty acid tail, bound to a glycerol group, and a head consisting of a hydrophilic PO_4^- phosphate group covalently bound to a choline group. Its structure is less polar than AOT, affecting its bond with water molecules: in particular, a water structure is formed around the choline group, which does not accept hydrogen bonds [107]. The THz spectrum of water confined in DOPC has not yet been investigated: we measured the linear absorption spectra of the whole L2 peak using our ultra-broadband source.
We used a benzene-DOPC base solution, diluted with varying amounts of water [108]: at the lowest hydration level there are on average only two water molecules for each phosphate head ($w_0 = 2$), while at the highest hydration $w_0 = 16$ most of the water molecules in the center of the droplets see a bulk-like environment. The size and shape of DOPC RMs has been investigated by *Abel et al.* in Ref.[107] where they estimate RMs hydrodynamic diameters in a range from 40.5 $\mathring{A}$ at $w_0 = 2$ to 74.7 $\mathring{A}$ for $w_0 = 16$.

The diamond cell used for bulk water measurements was filled with DOPC-benzene solution, using a 250 μm Teflon spacer to reach absorbance levels close to the neat water measurement. To isolate the absorption from the water droplet from benzene or surfactant absorption, as a reference I_0 we used the base DOPC solution in benzene, at a 0.25 molar concentration.
Fig.2.4.(a)-(d) show linear absorption spectra for four different hydration levels w_0= 2, 4, 8, 16. Panel (e) shows the absorption from the base solution, using transmission through the empty diamond windows as a reference. The base solution has a prominent absorption band around 20 THz: the saturation appearing in this range in the hydrated measurements stems only from absorption in benzene, and is unrelated to the confined water nanodroplets.
The $w_0 = 16$ is qualitatively very similar to the bulk water spectrum (shown in panel (f) for comparison). As the RM size decreases however, a feature at 25 THz begins to appear, becoming more prominent than the bulk L2 peak for $w_0 = 2$. As expected, interfacial water features are more prominent for small structures and disappear for larger droplets, but contrary to the effect measured for AOT, in DOPC the bound water absorption appears blue shifted of ~ 200 cm^{-1} compared to the L2 peak.

To gain better insight, the group of Damien Laage (*ENS Paris*) performed Molecular Dynamics simulations of water confined in DOPC micelles, in the same framework of their previous work in Ref.[107]: the reverse micelle structure is pre-assembled around a water sphere of adjustable size, initially in a bulk configuration. The DOPC molecules are then arranged around it with the

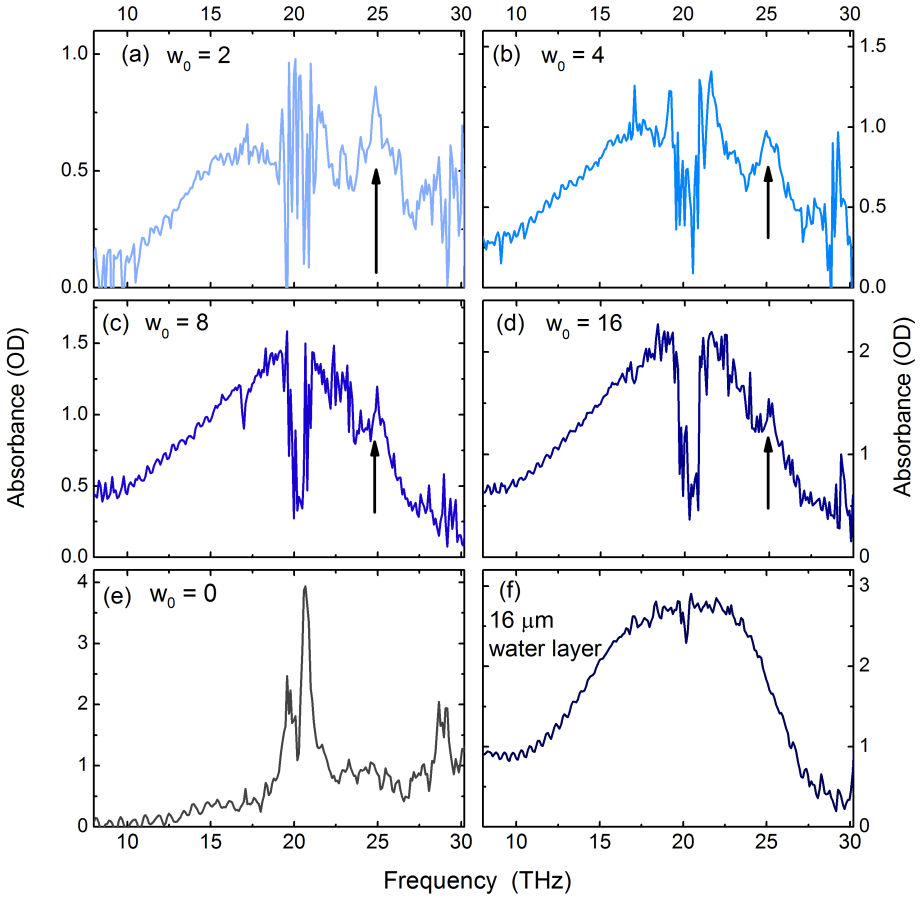

Figure 2.4: Absorption spectra of water confined in DOPC micelles for different water concentrations using the base DOPC solution ($w_0 = 0$) as a reference. (a) $w_0 = 2$ water molecules per phosphate head (b) $w_0 = 4$ (c) $w_0 = 8$ (d) $w_0 = 16$. For comparison, the base DOPC-benzene solution (e) and bulk water (f) absorbance are also shown, in both cases using the empty diamond cell as a reference.

phosphate pointing toward the water and the fatty acid tails directed outward in a cube filled with benzene molecules. A molecular dynamics simulation (GROMACS v4.6.6) retrieves the RM final configuration by steepest descent on the system energy, using the CHARMM force field for the DOPC and benzene and the SPC/E potential for water.

The librational spectrum is then calculated from Ref.[109]

$$\alpha(\omega)n(\omega) = \frac{4\pi\omega \tanh(\hbar\omega/2k_BT)}{3\hbar cV} \int_{-\infty}^{+\infty} dt e^{-i\omega t} \langle \mu(t) \cdot \mu(0) \rangle \qquad (2.1)$$

where $\alpha(\omega)$ is the absorption coefficient, $n(\omega)$ the refractive index, V the sample

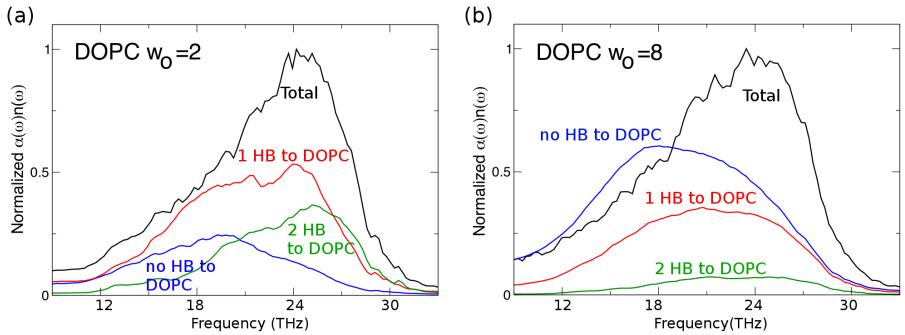

Figure 2.5: Calculated absorption spectrum for DOPC solution. The black curve shows the total absorption, decomposed in three component: the blue curve shows molecules bonded to the water hydrogen network, the red curve molecules with one hydrogen bond with the phosphate group, and the green curve with both. (a) $w_0 = 2$, showing a spectral feature at 25 THz (830 cm^{-1}) (b) $w_0 = 8$, bulk like behavior.

volume, T the temperature, and $\mu(t)$ the total dipole moment.

Fig.2.5 shows the calculated absorption spectra respectively for $w_0 = 2$ (Fig.2.5.(a)) and for $w_0 = 8$ (Fig.2.5.(b)). The black line is the total absorbed intensity: for $w_0 = 8$ it has only one peak at 600 cm^{-1}, consistent with bulk-like behavior, while for $w_0 = 2$ the main peak is blue shifted (650 cm^{-1}), with a second peak appearing at 830 cm^{-1} = 25 THz.

The emergence of a second peak well reproduces our experimental result. The overall blue shift of the main peak cannot be observed in our data, but the region around 21 THz is saturated by benzene absorption, so that a shift of a couple of THz can not be observed reliably.

The total absorption was decomposed in its contribution coming from bulk like water, connected to the hydrogen bond network of other water molecules, and bound water, with one or both hydrogen bonds linked to DOPC phosphate groups instead: to this end the absorption spectrum was calculated using the dipole moment of each individual molecule instead of the total dipole, discarding cross correlations between water molecules. For $w_0 = 8$ the bulk-like contribution (in blue) dominates the absorption, and molecules with two hydrogen atoms bonded to the DOPC are a negligible fraction (HB2, green line). Water with 1 bond to the DOPC (HB1, red line) show a slight blue shift which broadens the band overall, but without forming a separate peak.

At $w_0 = 2$, on the other hand, most water molecules are bonded to a phosphate head and the bulk like contribution at 20 THz is the weakest component of the

overall absorption. HB1 water gives the most prominent contribution, with a broader peak centered at $\sim$ 700 cm^{-1}: contrary to HB1 for $w_0 = 8$, the peak shows two lobes at 20 and 25 THz. HB2 waters, which are entirely bound to DOPC instead to the water network, absorb mainly at 25 THz, contributing to the appearance of the second absorption band.
The appearance of a blue shifted librational peak is due to stronger hydrogen bonds with phosphate groups. Such a blue shift is not observed in AOT RMs, where the more delocalized negative charge on the sulfonate group does not provide a stronger bond compared to neighboring water molecules.

2.3 Characterization of interfacial water on the DNA backbone

Interaction with the surrounding water molecules is essential to the structural and functional properties of large biomolecules. In particular, DNA double helix shape (B-form DNA) is only stable when the molecule is surrounded by a sufficient number of water molecule, while at a low hydration level the molecule undergoes a structural change assuming the more rigid A-form [110].
Interaction with the surrounding water environment, which involves both long range Coulomb interaction and more local hydrogen bond fluctuations, has been the object of numerous studies in the IR range [111]. The libration and OH stretching band in particular are sensitive probes for vibrations of the phosphate groups on the DNA back bone. At high hydration level the water hydrogen bond network works as a heat sink for the excited backbone, while at lower hydration levels the water molecules are mainly fixed on the main hydration sites (phosphate groups and Na counterions on the back bone), with significant reduction on their rotational degrees of freedom. Two-dimensional IR spectroscopy has proven to be a very effective tool in studying the dynamics of the DNA-water surface, exploring the anharmonicity of modes on the DNA backbone and highlighting how only the first two water layers are involved in interaction with the DNA [112].
In the THz range the spectra of single DNA bases has been investigated [113, 114], but the effect on librations of molecules bonded to the backbone phosphate groups has been explored only up to 3 THz [115]. To study DNA hydration in a range up to 30 THz, we drop-cast thin ($\sim$ 10 μm) DNA lipid films (CTMA) [112] on our cell diamond windows. Instead of filling the cell with liquid, it was connected to either an hydrating ($NaBrO_3$) or dessicating agent (P_2O_5), allowing us to go from 0% relative humidity to 92% r.h., i.e. from 2 water molecules

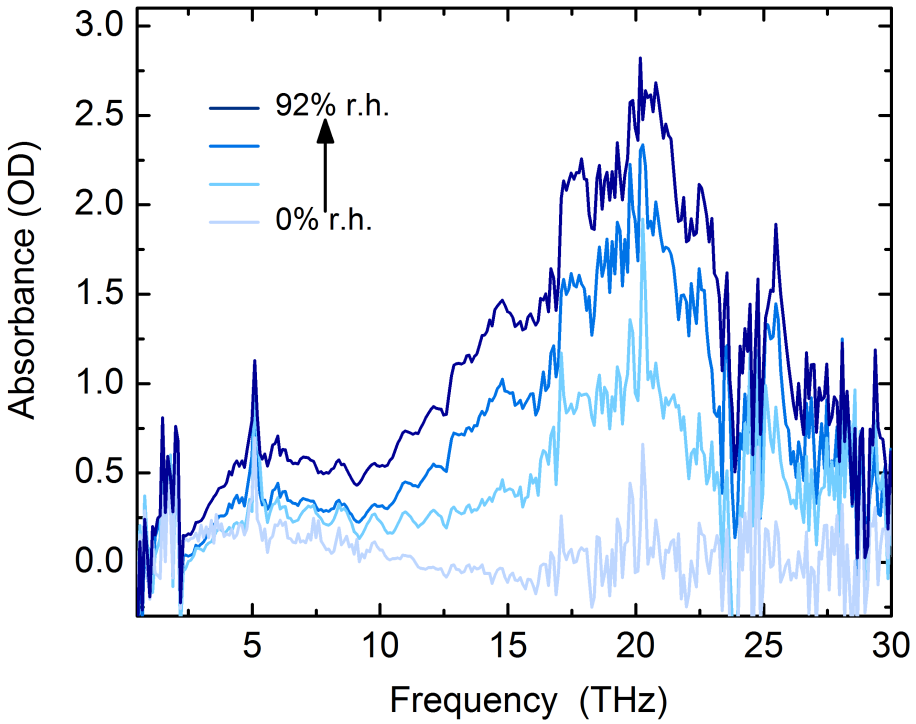

Figure 2.6: Absorption spectrum of DNA-AP23 lypid film at different hydration levels. The lighter curve corresponds to the dry DNA-lipid film, while darker curves represent higher hydration levels, up to a fully hydrated DNA film (92% hydration) after 10 hours under the effect of an hydrating agent.

per base pair to more than 20. As a reference we use the measured transmission through the fully dry DNA film, to avoid any contribution from absorption in the lipid matrix.

During the (de-)hydration process we kept the sample under nitrogen atmosphere in our set-up, measuring continuously to fully capture the transition. Figure 2.6 shows representative traces at different stages of hydration, going from 0% r.h. (lightest line) to 92% r.h. (darkest). Each curve is the average of 10 consecutive scans, each taking 4 minutes. Full hydration is reached after roughly 10 hours.

At full hydration, the measured spectrum resembles that of neat water, with the hydrogen bond stretching band around 5 THz and the librational band at 20 THz. The librational peak is modulated compared to the pure water measurement, with the largest modulations appearing at 15 and 25 THz. Furthermore, the 25 THz feature appears very early in the hydration process: at first it is as prominent as the main librational band, while at 92% r.h. it reaches only

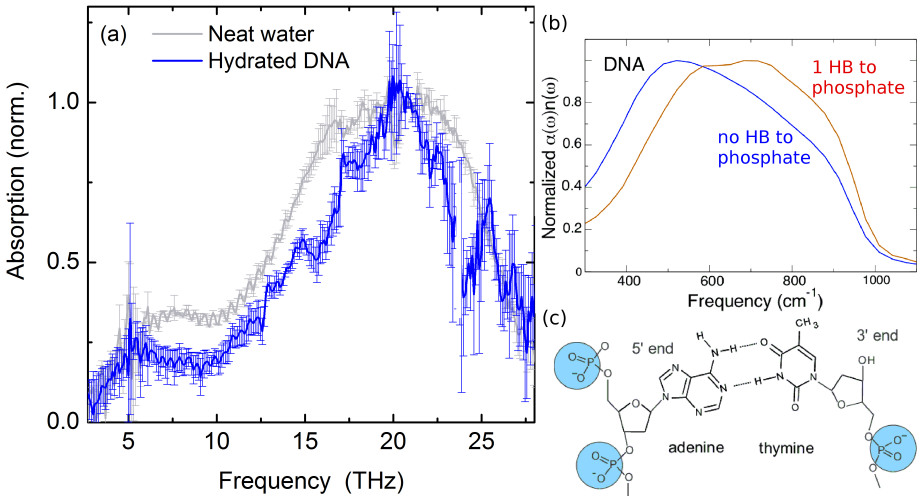

Figure 2.7: (a) Comparison between hydrated DNA at 92% r.h. (blue line) and 6 μm bulk water absorption (grey line) spectra. The curve is the average of five different hydration runs, with the error bars showing the standard deviation for each frequency. The features at 15 and 25 THz can be related to water bonded to different hydration sites on DNA. (b) Calculated absorption spectrum for water molecules with one vs. no bonds to DNA backbone phosphate groups (c) Scheme of an adenine-thymine base pair connected to the DNA backbone, with the position of the PO_2^- groups marked by blue circles

2/3 of the absorbance. This is consistent with the assumption that at very low hydration levels, the first water molecules bond with the backbone phosphate groups (shown in Fig.2.7.(c)), so that their rotational motion is confined by a steeper potential in the same vein as the water molecules bonded to phosphate heads on DOPC.

Figure 2.7.(a) shows the absorption spectrum of DNA at 92% r.h., averaged from five different full hydration runs (blue line), compared to bulk water. The features at 15 THz and 25 THz are larger then the fluctuations (the error bars show one standard deviation) and clearly differ from the L band in pure water. Considering the similarities with the shifts observed in RMs with different charged groups, the these two side bands can be assigned to water molecules attached to different sites on the DNA backbone. The hydration layer of DNA is highly heterogeneous, leading to markedly different water dynamics on different hydration sites [116]: the electric potential at each spot allows for different ranges of motion compared to the normal hydrogen bond network, shifting the libration peak to higher or lower frequencies. On the other hand water farther

out from the first hydration shell is fundamentally screened from interacting with the DNA surface, and has vibrational properties closely related to neat water.

Molecular dynamics calculations in the same framework as those performed for reverse micelles have been carried out for water bonded to DNA phosphate heads in an aqueous solution. As shown in Fig.2.7.(b), water molecules with one bond to the DNA backbone display a blue shift in absorption compared to molecules connected only to the neat water. The change in bond strength is reflected also in a shortened average oxygen-oxygen distance, which is 2.65$\mathring{A}$ for molecules next to a DNA phosphate group compared to 2.75 $\mathring{A}$ in neat water.

More detailed molecular dynamics simulations would be required to fully understand the feature in our spectra, including the smaller peaks appearing at 22 THz and 17 THz, but the insight afforded by broadband THz spectroscopy are plain to see.

Chapter 3

Multidimensional infrared and terahertz spectroscopy

Understanding the complexity of molecular dynamics in the condensed phase requires a more elaborate technique than linear spectroscopy. In a system with many degrees of freedom, it is nearly impossible to resolve the electronic and vibrational responses and to understand their couplings if they are all projected on a single temporal or spectral axis. To address this problem, multidimensional coherent spectroscopies have been developed: by spreading the signal along multiple axes, such techniques can unravel the complex interactions typical of solid state matter and liquid solutions.

Multidimensional spectroscopies were first developed for the microwave range, in the framework of nuclear magnetic resonance (NMR) [117], where intricate pulse sequences and phase cycling can be used to isolate and select specific signals [118]. To access faster time scales than the millisecond range typical of NMR, the same principles have been applied to visible and ultraviolet light (UV-VIS) and to the infrared (IR) range. Two-dimensional IR spectroscopy has proven to be an invaluable tool to study vibrational properties, dipole-dipole couplings and molecular interactions in solid state and in solutions [119, 120]. At higher frequencies, multidimensional spectroscopy is used to study the electronic response [121].

Spectroscopy in the THz range has taken longer to become a widely explored field, due to a scarcity of suitable detectors and sources. THz time domain spectroscopy (TDS) [122] has first been used to study linear material properties in the THz range. Static and transient techniques in transmission and reflection geometry have been widely employed for both scientific and industrial appli-

cations, including but not limited to pharmaceutical and security applications, monitoring of industrial processes and art conservation [30].
More recently the dynamics of THz range interactions have been explored in pump-probe experiments, often in mixed THz pump-IR probe or optical probe schemes [5, 57] or Raman-THz spectroscopy [123]. The development of intense THz sources has allowed to expand the field into more complex applications, including coherent control of light matter interaction [6], and extending to different spectral domains, e.g., with THz pump/X-Ray probe methods [124, 125].
Multidimensional THz-THz spectroscopy follows more closely the 2D-IR concept: it has been developed first in a 2D pump-probe scheme [22] characterized by its collinear interaction geometry, and later on also in a fully three-dimensional scheme [24, 126].
The next section contains a brief overview of multidimensional IR spectroscopy concepts, particularly concerning its use to unravel the contributions to nonlinear susceptibilities. In particular, time ordered Feynman diagrams will be used to describe the third order nonlinear response. Our concept of THz spectroscopy will then be described in more detail, highlighting the common ground with IR spectroscopy as well as the main differences, particularly concerning how phase resolved detection in a collinear interaction geometry enables us to easily access multiple orders of nonlinear interaction at once. Finally, the experimental implementation of a two-dimensional THz spectroscopy and of a two-color THz-MIR set-up will be described.

3.1 Density matrix representation and Liouville pathways

To describe the response of an ensemble of oscillators - i.e. a condensed matter system - to external electric fields, it is convenient to use the density matrix formalism [127]. The density matrix operator is defined as:

$$\rho = |\psi\rangle\langle\psi| = \sum_{n,m} c_n c_m^* \, |n\rangle\langle m| \tag{3.1}$$

for a pure state $|\psi\rangle$. In a condensed-phase system however, we typically deal with statistical ensembles of oscillators. In that case the density matrix is defined as an ensemble average:

$$\rho = \sum_s p_s \, |\psi_s\rangle\langle\psi_s| \tag{3.2}$$

where p_s is the probability of finding the system in a state $|\psi_s\rangle$, with $p_s \geq 0$, $\sum_s p_s = 1$. The elements of the density matrix are then written as

$\rho_{n,m} = \sum_s p_s c_m^{s*} c_n^s = \overline{c_m^* c_n}$.

The diagonal elements of the density matrix represent the population of the system levels, while off-diagonal elements are the coherences between different states. The expectation value of an operator is calculated by taking the trace of its product with the density matrix, $\langle A \rangle = \mathrm{Tr}(A\rho) = \sum_{n,m} A_{n,m}\rho_{n,m}$.

The time evolution of the density matrix can be calculated using the Liouville equation:

$$\frac{d}{dt}\rho = -\frac{i}{\hbar}[H, \rho] \tag{3.3}$$

where H is the system Hamiltonian. We consider an interaction with a classical electric field $\mathbf{E} = -1/c\frac{\partial \mathbf{A}}{\partial t} = E_0 \sin(kx - \omega t)$, where $\mathbf{A}$ is the field vector potential in the Coulomb gauge ($\nabla \cdot \mathbf{A} = 0$). By neglecting the term in $|A|^2$, the system Hamiltonian is:

$$H = \frac{\mathbf{p}^2}{2m} - \frac{e}{mc}\mathbf{p} \cdot \mathbf{A} \tag{3.4}$$

where $\mathbf{p}$ is the momentum, m is the mass, e the elementary charge, and c the speed of light. The interaction with the field is expressed by the $\boldsymbol{p} \cdot \boldsymbol{A}$ term, which in the dipole approximation reduces to $-\frac{e}{mc}\mathbf{p} \cdot \mathbf{A} \sim -\mathbf{E}\langle\mu\rangle$, where $\langle\mu\rangle = e\langle x\rangle$ is the dipole moment.

We then write the system Hamiltonian in matrix form as the sum of the base Hamiltonian $H_0 = \frac{p^2}{2m}$, with energy eigenvalues on the diagonal, plus the electromagnetic interaction H_E, which contains the off-diagonal dipole terms:

$$H = H_0 + H_E = \begin{bmatrix} \epsilon_1 & 0 \\ 0 & \epsilon_2 \end{bmatrix} + \begin{bmatrix} 0 & -\mu \cdot E(t) \\ -\mu \cdot E(t) & 0 \end{bmatrix} \tag{3.5}$$

where $\epsilon_{1,2}$ are the energy of the state, $E(t)$ is the time dependent electric field. Calculating the time evolution for a two-level system density matrix with these Hamiltonian gives the optical Bloch equations, which will be discussed in Chapter 3, Sec.4.2.1.

To study the nonlinear response of a sample, we want to calculate its macroscopic polarization, given by the expectation value of the dipole operator: $P = \langle\mu\rho\rangle$. For a two-level system we see that off diagonal elements give rise to a macroscopic polarization, which emits a light field at frequency corresponding to the transition energy.

Perturbation theory is used to expand the density matrix and the system polarization with respect to the electric field. The macroscopic polarization is:

$$P \propto \sum_n \chi^{(n)} E^n = \sum_n \langle \mu \rho^{(n)}(t) \rangle \tag{3.6}$$

The off-diagonal element of the density matrix create oscillating polarization, emitting light at the transition frequency.

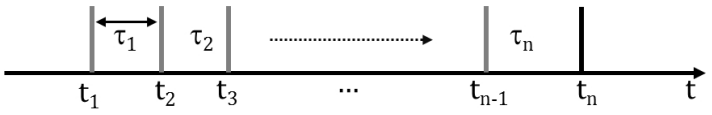

Figure 3.1: Schematic representation of multiple interactions: each pulse, represented as a dark grey line, arrives at time t_1, t_2,..., t_{n-1}. The last interaction at t_n represents the last emission resulting from all previous interactions (black line).

The n-th component of the nonlinear polarization is then simply $P^{(n)} = \chi^{(n)}E^n = \langle\mu\rho^{(n)}(t)\rangle$. To write the perturbative expansion of the density matrix at time t we make use of the time-evolution operators in the interaction picture:

$$U_0(t,t_0) = e^{-i\hbar H(t-t_0)} \tag{3.7}$$

For an n-th order interaction, we assume that the system interacting with n electric fields at times $t_0,...,t_n$, separated by intervals $\tau_1...\tau_n$, as shown in Fig.3.1. Each field has an interaction picture dipole operator $\mu_I(t_n) = U_0^\dagger(t,t_n)\mu U_0(t,t_n)$. The n-th order density matrix in the interaction picture is the convolution in time of the electric fields with the nested commutators $[\mu_I(t_n),\rho(-\infty)]$, so that the n-th order polarization reads:

$$\begin{aligned} P^{(n)}(t) &= \left(-\frac{i}{\hbar}\right)^n \int_0^\infty d\tau_n \int_0^\infty d\tau_{n-1}... \int_0^\infty d\tau_1 \\ &\quad E(t-\tau_n)E(t-\tau_n-\tau_{n-1})...\cdot E(t-\tau_n-\tau_{n-1}-...-\tau_1) \\ &\quad \langle\mu(\tau_n+...\tau_1)[\mu(\tau_{n-1}+...\tau_1),...[\mu(0)\rho(-\infty]...])\rangle \end{aligned} \tag{3.8}$$

We can define the n-th order response function $S^{(n)}(t_1,...t_n)$ as:

$$S^{(n)}(t_1,...t_n) = \left(-\frac{i}{\hbar}\right)^n \langle\mu(t_n+...t_1)[\mu(t_{n-1}+...t_1),...[\mu(0)\rho(-\infty]...])\rangle \tag{3.9}$$

The many terms involved can better be dealt with using a diagrammatic representation.

Double-sided Feynman diagrams

To represent different Liouville interaction pathways, a graphical representation using Feynman diagrams [128] is helpful. Double sided diagrams [129] represent interaction on the *bra* and *ket* side in a very intuitive fashion, so that it is clear when a system is found in a polarization or population state.
Examples of double sided diagrams are shown in Fig.3.2.(a)-(c), and read as

follows: the vertical axis represent time, the instant when an interaction occurs is marked by dashed lines. The system state is written in bracket notation between two vertical line, and interactions of an electric field characterized by (k, ω) with the system are shown as arrows: the left side represent the time evolution of the *ket* side of the density matrix, and the right line the *bra* side evolution. Incoming arrows represent absorptive interactions raising the system to an higher level on one side, while outgoing arrows are emittive interactions which bring the system to a lower level. Absorptive interactions on the *ket* side carry a + sign, and emissions a - sign; interactions on the *bra* side have their sign reversed. This can be summarized by saying that a right pointing arrow has a phase $e^{-i\omega t}e^{+ikr}$ and a left pointing arrow $e^{+i\omega t}e^{-ikr}$.
A system ends up in a population state when the *ket* and *bra* side are in the same state (e.g. $|1\rangle\langle 1|$), requiring an even number of interactions. If the quantum levels are different (e.g. $|1\rangle\langle 0|$) the system is in a polarization or coherence state, i.e. an oscillating polarization at frequency ω_{01}.
The last interaction, generating the signal that is measured by an external observer, must be an emission on the *ket* side, and it must leave the system in a population state. The wave vector and frequency of the emitted radiation are linear combinations of the wave vectors and frequencies of the interacting fields, taken with the appropriate signs:

$$\vec{k}_S = \pm\vec{k}_1 \pm \vec{k}_2 \pm \vec{k}_3 \tag{3.10}$$

$$\omega_S = \pm\omega_1 \pm \omega_2 \pm \omega_3 \tag{3.11}$$

Fig.3.2 shows some exemplary interactions in the third order for a 3-level system. Diagram (a) shows stimulated emission from the first excited states: the first two pulses take oscillators first into a polarization state, and then in a population state at the first excited level. A third pulse acting as a probe brings the system back to a $|1\rangle\langle 0|$ polarization state, which relaxes back to the ground state in en emittive interaction.

The second diagram - in panel (b) - shows molecules which are back in to the ground state after the first two interaction, corresponding to a ground state bleaching. The last diagram in (c) depicts excited state absorption: the system in taken to the first excited state by the first two interactions, so that the third pulse can bring the system up to a coherence involving the second excited state, and the last emission returns it to a $|1\rangle\langle 1|$ population.
Another common way of displaying Liouville pathways [130] is shown in panels (d)-(e): here the vertical axis represents energy, with the ground state at the bottom and excited state on top; time is on the horizontal axis, running left to

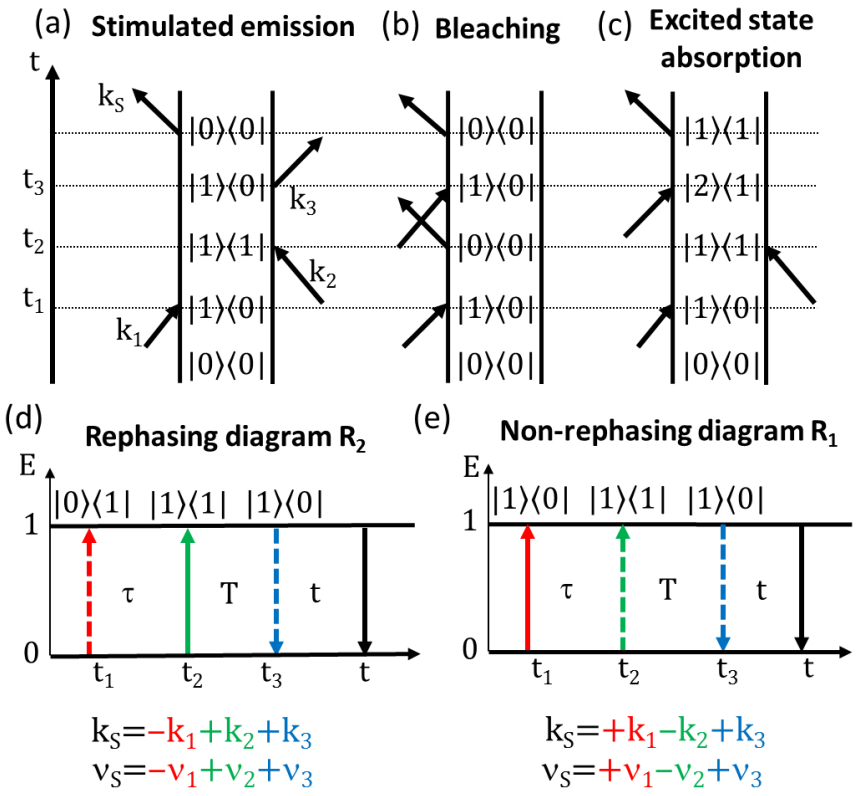

Figure 3.2: (a)-(c) Examples of double sided Feynman diagrams for different interactions: stimulated emission (a), ground state bleaching (b) and excited state absorption (c). The vertical axis represents time, arrows are interaction either on the *ket* (left) or *bra* (right) side of the density matrix. Incoming arrows are absorptive interactions, outgoing arrows are emittive. The quantum state of the system is specified in bracket notation. (d)-(e) Schematic representation of respectively a rephasing and non-rephasing $\chi^{(3)}$ interaction sequence as time ordered Feynman diagrams. The horizontal axis represents time, and the vertical axis energy. Arrows represents absorption (upward) or emission (downward), either on the *ket* (solid arrow) or *bra* side (dashed arrow). The last black arrow is an emission on the *ket* side, read out as the emitted signal: its wave number and frequency are a linear combination of those of the interacting pulses

right. The distinction between *bra* and *ket* interaction is shown by the arrows themselves: solid lines correspond to interactions on the *ket* side and dashed lines on the *bra* side.

Reducing the number of relevant diagrams

We now consider three pulses interacting with the sample at times t_1, t_2, t_3,separated respectively by a delay time τ and a waiting time T. The third order response emitted at time t is expressed by the commutators in

$$P^{(3)}(t) = \langle \mu \rho^{(3)}(t) \rangle = \langle \mu(t)[\mu(t_3), [\mu(t_2), [\mu(t_1,)\rho(-\infty)]]] \rangle \tag{3.12}$$

This requires calculating the convolution in time of the electric fields at the time of each interaction with the response function $S^{(3)}$. We write each field as $E(t) = E_A(t)(e^{-i\omega t + ikr} + e^{+i\omega t - ikr}) + E_B...$, including terms from the three pulses, each split in a negative and positive phase component.
We can simplify the calculation if some assumptions are valid:

- **Semi-impulsive limit** If we can assume the laser pulses to be significantly shorter then the time-scales of any response in the system, the interaction is said to be in the semi-impulsive limit. The pulses are then approximated by δ functions occurring at a fixed time - e.g. pulse A is $E_1(t) = E_1 \delta(t - t_1) e^{i(\pm\omega t \mp kr)}$

- **Time ordering** In the semi impulsive limit the pulses are subjected to strict time-ordering: we can assume that the only relevant diagrams have the pulses interacting in an 1-2-3 order.

- **Rotating wave approximation** If we can assume that only resonant interaction affect the system, then the phase of the electric field contains a term $e^{\pm i\omega t} = e^{\pm i\omega_{01} t}$, equal to the phase of the electric dipole matrix element. When calculating the diagram, one of the electric field phase terms will result in a rapidly oscillating term $\propto e^{\pm 2i\omega t}$. The other term, with an opposite sign, cancels out with the dipole phase, giving a slow varying term $\propto e^{-\Gamma t}$. In the RWA we can discard the oscillating terms, since they integrate to zero: this corresponds to keeping only one sign in the electric field phase.

The relevant diagrams are reduced to 4, typically labeled R_1, R_2, R_3, R_4. Their complex conjugate diagrams, carrying the same information, are discarded in the RWA. Due to phase matching consideration, diagrams $R_{1,4}$ and $R_{2,3}$ have different wave vectors and are emitted in different directions: they represent the rephasing and non-rephasing components of the third-order nonlinear response. The diagrams R_1 and R_2 describe stimulated emission, R_3 and R_4 bleaching: they carry redundant information, so that only one set of diagram needs to be considered. To give a full description of the response in the perturbative regime,

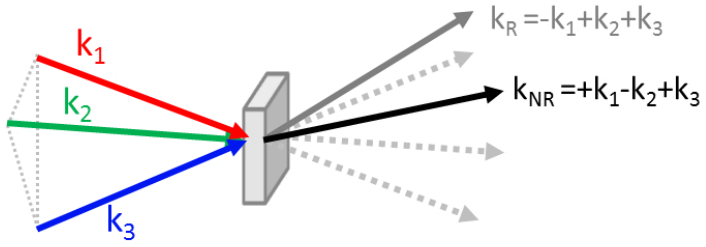

Figure 3.3: Rephasing and non-rephasing signals can be distinguished by their different wave vectors: three pump beams with wave vectors $\vec{k}_1$, $\vec{k}_2$, $\vec{k}_3$, represented by colored solid arrows, shine on a sample generating rephasing (solid grey line) and non-rephasing (solid black line) signals in different directions

it is enough to focus on the two diagrams R_1 and R_2 which represent rephasing and non-rephasing pulse sequences.

Rephasing vs. non-rephasing contributions

The R_1 and R_2 diagrams, representing the non-rephasing and rephasing contributions to the third order response, are shown in Fig.3.2.(d)-(e). The main difference between them is the phase relation between the first and third excitation, and the resulting wave vector of the final emission. Let us first consider R_1 (panel (d)): here the first pulse on the *ket* side ($+k_1$) creates a polarization which then evolves through a free induction decay (FID), resulting in a loss of coherence. After a delay time τ the second pulse interacts on the *bra* side ($-k_2$) bringing the system to a population state on the first level. The population evolves during the waiting time T, over which energy relaxation, population transfer or spectral diffusion can occur, influencing the dynamics of subsequent interactions. A third pulse performs the last interaction, inducing emission on the *bra* side ($+k_3$). The last polarization state is the same as the one induced during τ: the oscillators dipoles do not regain the coherence lost in the previous evolution, and the emission stems from the FID of the residual coherent polarization.

In the rephasing diagram R_2 (panel (e)) the first two pulses act first on the *bra* side and secondly on the *ket*, in the opposite order as in R_1: when the third pulse acts again on the *bra* side, it brings the system back to a coherence state $|1\rangle\langle 0|$, conjugate to the coherence during τ. Since the dipoles have been "flipped over", the same processes that caused dephasing now restore the lost coherence, barring any spectral diffusion during the population time. After the dipoles

recombine an echo is emitted: for an inhomogeneous line, it will appear as a pulse after a time equal to τ, with a slope depending both on the time delay over which coherence was lost and on the line natural dephasing time.
Overall, the emission wave vector and frequency for rephasing (R) and non-rephasing (NR) signals are given by:

$$\vec{k}_{NR} = +\vec{k}_1 - \vec{k}_2 + \vec{k}_3 \qquad \nu_{NR} = +\nu_1 - \nu_2 + \nu_3 \tag{3.13}$$

$$\vec{k}_R = -\vec{k}_1 + \vec{k}_2 + \vec{k}_3 \qquad \nu_R = -\nu_1 + \nu_2 + \nu_3 \tag{3.14}$$

Even if they all have the same frequency, due to phase matching conditions they can be differentiated by their wave vectors in real space: Fig.3.3 shows three pulses with three independent k-vectors (red, green and blue arrows), which generate rephasing (dark grey arrow) and non-rephasing (black arrow) signals emitted in different spatial directions.

3.2 Multidimensional infrared spectroscopy

In the last twenty years two dimensional infrared spectroscopy [120, 131] has become a most prominent method to understand the dynamics of the $\chi^{(3)}$ response in many different systems. It has been used to study semiconductors and low dimensional confined systems, unraveling complex many body interactions [132], studying excitons in quantum wells structures [133] or energy transport in carbon nanotubes [134]. It gives insight into vibrational properties of water [135] and hydrogen bonded systems [136], the couplings in photosynthetic molecules [137] and in the ultrafast dynamics of DNA and of many other biological molecules in an aqueous solution [138].
Nonlinear multidimensional spectroscopy aims at retrieving the third order response made up of the various rephasing and non-rephasing diagrams. To do so, multiple pulses interact with the sample separated in time by different delays. The nonlinear signal is collected of two time or frequency axes, so that correlations can be unraveled over multiple dimensions.
An early pump-probe technique involves using an intense, narrow-band pump pulse, which interacts twice with the sample bringing it to a population state. After a delay τ the population is read out by a broad-band probe, which is then measured in a frequency-resolved detector, providing the frequency axis ν_{probe}. Scanning over the pump frequency provides a second frequency axis ν_{pump}. However, since a narrow-band pump is necessarily long in the time domain, this limits the time resolution of the experiment.
An alternative approach consists in using ultrashort pulses to impulsively ex-

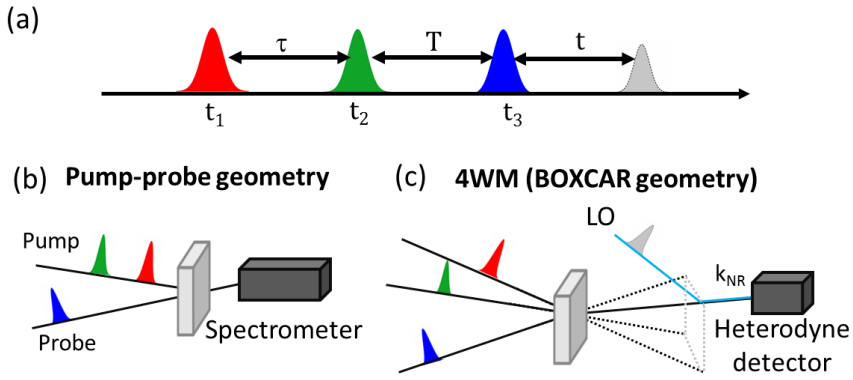

Figure 3.4: Interaction schemes for three-pulse IR spectroscopy: (a) three pulses interact with the sample at times t_1,t_2,t_3, separated respectively by a delay time τ and a waiting time T. (b) Partially collinear pump-probe set-up: two phase locked pump pulses bring the sample in a population state, which is read out by a non-collinear probe, which is measured by a spectrometer. (c) Fully noncollinear 4WM set-up: three pulses, each with independent $\mathbf{k}$ vectors, perform three interactions. Different nonlinear signals are emitted each in a direction fixed by the by momentum conservation (rephasing $\mathbf{k}_R$ and non-rephasing $\mathbf{k}_{NR}$ signals are shown): they are heterodyned by a local oscillator LO, at a time t after the third interaction.

cite transitions in the large pulse bandwidth. Typically, three separate beams interact each only once with the sample, separated by variable delays as shown in Fig.3.4.(a): the first beam arrives at time t_1, the second beam at $t_2 = t_1 + \tau$ after the coherence time τ, and the third beam at $t_3 = t_2 + T$ after the waiting time T. The system is put first in coherence state, then in a population state by the second beam. After population evolution during T, the third beam creates again a coherence, either along a rephasing or a non-rephasing pathway.

Two possible interaction geometries are shown schematically in Fig.3.4 - a partially collinear pump-probe set-up in panel (b) and a fully noncollinear 4-wave mixing (4WM) scheme in panel (c): these two methods are fully equivalent and return identical nonlinear signals [139].

In a pump-probe geometry, two collinear, phase locked pulses bring the sample to a population state: scanning the delay τ between the two beams provides the frequency axis $\nu_{pump} = \nu_\tau$. After the waiting time T the probe performs a third interaction, and is read out by a spectrometer providing the second axis $\nu_{probe} = \nu_t$. Pump-probe schemes are well suited for distinguishing homogeneously and inhomogeneously broadened spectral lines through dynamic hole

burning, and to gauge spectral diffusion during the population evolution.
In a 4WM schemes, the three beams interact in a fully non-collinear geometry. The nonlinear signal is read out by a local oscillator (LO) after a time interval t from the last interaction: the two frequency axis ν_t and ν_τ are defined by scanning the t and τ time delays. The emitted nonlinear signals are emitted in a direction fixed by momentum conservation $\vec{k}_S = \pm\vec{k}_1 \pm \vec{k}_2 \pm \vec{k}_3$. The rephasing and non-rephasing contributions are emitted in different directions. In the widely used BOXCAR interaction geometry (shown in the figure) the pump beam occupy three corners of a square, and the nonlinear signal is emitted in the direction of the fourth corner: phase cycling procedures [140, 141] are used to select either a rephasing or a non-rephasing contribution in the detection direction. Collinear 4WM schemes have also been developed, in order to reduce the technical challenges in setting up a BOXCAR experiment. To preserve the ability to select a specific interaction pathway the pulses polarization is used similarly to the phase cycling procedures used for NMR [142, 143].

3.2.1 Concepts of 2D IR spectroscopy

In this section we will describe a prototypical result of 2D IR spectroscopy: as an example, we consider two coupled transitions at fundamental frequencies ν_1 and ν_2, shown as solid black arrows in Fig.3.5.(a)) with transitions to higher excited states in grey.
The emitted electric field is measured in a spectrometer or by heterodyning with a local oscillator in order to extract the third order response $S^{(3)}(\tau, T, t)$. A Fourier transform along the two temporal axes τ and t returns the third order response in frequency space $S^{(3)}(\nu_{pu}, \nu_{pr})$, where multidimensional spectra are analyzed (Fig.3.5.(c)): the horizontal axis corresponds to the frequency of the probe beam, ν_t, and the vertical axis is the frequency of the pump ν_τ. The 2D correlation spectrum shows different peaks, positioned in spots corresponding to the transition frequencies. The peaks position, amplitude, and line-shape, offer many insight in to the microscopic details of the interaction [144].

The diagram shows positive signals in red, and negative signal in blue. The main spots appear on the frequency plane diagonal, at the transition frequencies, the signal amplitude proportional to the dipole strength of the transition. The positive signals - exactly on the diagonal - results from two superimposed contributions: stimulated emission from the upper states $|10\rangle$ (at ν_1) and $|01\rangle$ (at ν_2), and a bleaching of ground state absorption. The latter stems from increased probe transmission at the transition frequency when the number of

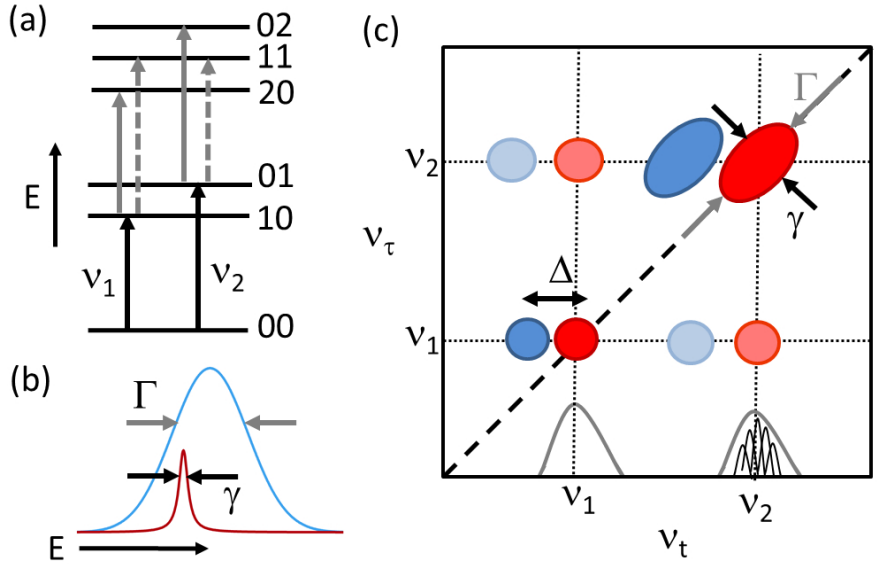

Figure 3.5: Concepts of IR spectroscopy: (a) Coupled transitions at frequencies ν_1 and ν_2, and their excited states (b) Homogeneous and inhomogenoeus broadening: the in homogeneous linewidth Γ of the gaussian blue line stems from the superposition of many smaller transition of natural linewidth γ, shown by lorentzian line in red (c) Correlation spectrum in the frequency plane as a function of the transition frequency ν_t (horizontal axis) and excitation frequency ν_τ (vertical axis). Bleaching signals appear as increased absorption on the diagonal (red spots), while excited state absorption appears as reduced transmission (blue spots), in a slightly off-diagonal position due to the anharmonicity Δ. An homogeneously broadened line (at ν_1) has a circular line shape, while an inhomogeneous line (at ν_2) has an elliptical line shape. The diagonal line width marks the inhomogeneous linewidth Δ, while the cross-diagonal dimension gives Γ. If the transitions are coupled, cross peaks appear on the anti-diagonal (light red and blue spots).

available oscillators in the ground state is reduced by excitation from the pump. Next to it, slightly of diagonal, the negative signal corresponds to excited state absorption (solid grey arrows in panel (a)). The red shift Δ on the probe frequency axis is due to the transition anharmonicity: if the oscillator were perfectly harmonic the positive and negative signals would overlap and cancel out. The separation between diagonal peaks can thus be used to gauge the degree of anharmonicity of a transition.

The shape of the diagonal peaks relays important information about the inter-

nal structure of an absorption line. If a transition is homogeneously broadened - like the excitation at ν_1 in Fig.3.5 - pump absorption at a frequency in the line bandwidth results in an overall change in signal amplitude evenly spread over the line: the resulting 2D signals are roughly circular in shape, so that the width γ of the lorentzian line can be retrieved from the circle diameter.
If on the other hand the transition is inhomogeneously broadened - as the transition at ν_2 - its gaussian line width Γ is the result of the superposition of many narrower transitions with slightly different central frequencies (Fig.3.5.(b)) due to local variations in the local potential. A narrow band pump excites only a specific transition, so that the pump-probe signal is not spread over the whole bandwidth, but localized to a certain homogeneous line of width γ (hole-burning). The nonlinear signal than has an elliptical shape: its longer axis along the diagonal corresponds to the inhomogeneous broadening, while the narrower off diagonal width gives the natural line width γ.
Away from the frequency space diagonal cross-peaks appear (ν_1, ν_2) and (ν_2, ν_1) if two transitions are coupled (shown in lighter shades of red and blue in the diagram). Considering the spot at (ν_1, ν_2), the positive signal is due to a bleaching of the transition at ν_2, excited by the pump. The probe causes excited state absorption to the $|11\rangle$ state (dashed grey arrow in panel (a)), recorded by the negative cross peak. In the absence of coupling, the two signals would overlap and cancel each other out.
By varying the waiting time in full correlation spectroscopy set up, or the delay time in a pump-probe geometry, the dynamics of the excitation evolution can be studied, by observing how the peaks, intensity and line shape evolve. When the delay is larger then the dephasing time, any correlation with the previous excitation is lost, cross peaks disappear and all signals acquire a broad, circular shape.

3.2.2 Absorptive line-shape

Both in a pump-probe and in a 4WM set-up, rephasing and non-rephasing signal components are emitted in different spatial directions, respectively $\vec{k}_R = -\vec{k}_1 + \vec{k}_2 + \vec{k}_3$ and $\vec{k}_{NR} = +\vec{k}_1 - \vec{k}_2 + \vec{k}_3$. In order to collect the full third order nonlinear response both need to be measured, either by moving the detector to the appropriate emission or by using phase cycling techniques. The rephasing diagram R_2 and the non-rephasing R_1 are proportional to the complex terms:

$$R_1(t_{pu}, t_{pr}) \propto e^{-\imath\omega t_{pu}} e^{-\imath\omega t_{pr}} e^{-\Gamma t_{pu}} e^{-\Gamma t_{pr}} \tag{3.15}$$

$$R_2(t_{pu}, t_{pr}) \propto e^{\imath\omega t_{pu}} e^{-\imath\omega t_{pr}} e^{-\Gamma t_{pu}} e^{-\Gamma t_{pr}} \tag{3.16}$$

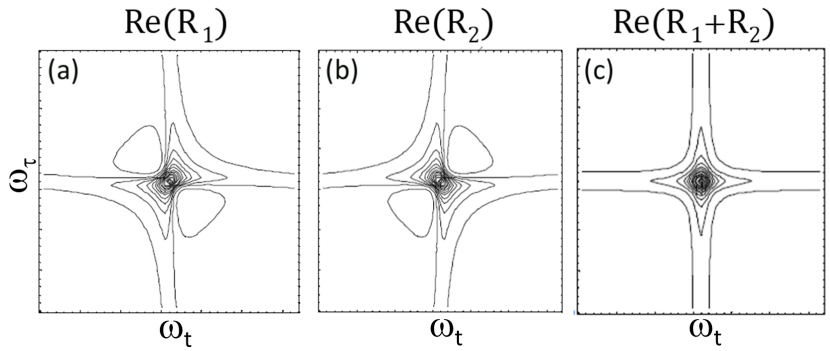

Figure 3.6: Real component of the rephasing (b) and non-rephasing (a) signal as a function of pump and probe frequency. Line shapes are broadened by dispersive components, which can be eliminated by calculating the purely absorptive line shape (c). The diagrams are taken from [131].

where the dephasing rate Γ has been included.

The time dependent third order response is proportional to the same phase terms, so that when it is Fourier transformed the frequency dependent line shapes are in the form:

$$R_1(\omega_t, \omega_\tau) \propto \frac{1}{-i(\omega_t - \omega) - \Gamma} \cdot \frac{1}{i(\omega_\tau - \omega) - \Gamma} \tag{3.17}$$

$$R_2(\omega_t, \omega_\tau) \propto \frac{1}{i(\omega_t - \omega) - \Gamma} \cdot \frac{1}{i(\omega_\tau - \omega) - \Gamma} \tag{3.18}$$

These terms are imaginary and contain both absorptive and dispersive contributions: the signals in the frequency domain have positive and negative components and broadened line shapes. As an example, the calculated real component of rephasing and non-rephasing contributions are shown in Fig.3.6.(a)-(b) (from [131]). The real component of the response is phase twisted, respectively on the both diagonal and cross-diagonal direction. The dispersive side bands contribute to broaden the linewidth, worsening the resolution of close-by transitions.
To overcome this issue, a purely absorptive line shape can be calculated by combining contributions from rephasing and non-rephasing diagrams. The well-established method proposed by *Khalil et al.* [145] involves summing the two contributions and taking the real part, thus obtaining a strictly positive (or negative) signal with the most narrow line width (Fig.3.6.(c)), called purely absorptive 2D correlation spectrum. This procedure results in high-resolution 2D spectra with narrow, well defined feature, but requires two separate measurements taken in identical conditions, since imbalances between the rephasing and

non-rephasing contributions results in imperfect cancellation of the dispersive features.
It must be noted that this technique can be applied only when the detected response stems exclusively from a third order nonlinearity. If the signal includes higher order contributions, as can easily happen in THz spectroscopy, it is not possible to define a purely absorptive line shape in a meaningful sense, and the absolute value of each component should be analyzed by itself to avoid mixing spurious contributions.

3.3 Multidimensional THz spectroscopy

The same techniques used in multidimensional IR spectroscopies are of great interest for the THz range, to unravel the complicated collective interactions typical of this spectral region. Two-dimensional THz spectroscopy was first developed in the pioneering work by *Kuehn et al.*, first in a scheme with two phase-locked pulses [22] and later in a 3-pulse set-up [17]. Two-dimensional experiments have afforded insight into many solid state systems, exploring quantum wells IS transitions [126, 146, 147], nonresonant interband excitations in bulk InSb [13], high order response and high harmonics generation in graphene [148], and nonresonant tunneling in ferroelectrics leading to bulk photovoltaic effect [8].
Most recently, a true multidimensional THz spectroscopy using three coherent THz beams has been used to study multiquantum coherences in InSb [23, 24]. The facility for higher-order non-resonant interaction characteristic for the THz range grants insight into dark two-photon and two-phonon coherences that would otherwise not be accessible, while by varying the waiting time the relaxation dynamics can be understood more in depth. In the next section the specific characteristics of 2D THz spectroscopy will be discussed, highlighting the advantages of using a collinear geometry together with an EOS detection scheme. The experimental work in this thesis is carried out using a two-pulse scheme.

Collinear geometry and phase resolved detection

The main advantage of our THz spectroscopy concept originates from using a collinear geometry in the sample. In a traditional 2D-IR experiment, e.g. in a pump-probe set-up, the beams will reach the sample at different angles, as shown in Fig.3.7.(a).
The $\mathbf{k}$ vector of a nonlinear signal stemming from a specific interaction se-

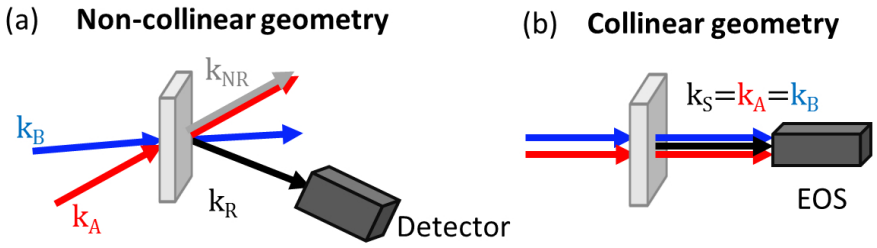

Figure 3.7: (a) Typical interaction geometry in IR spectroscopy: the pump beams (blue and red arrows) shine on the sample at an angle, so that each nonlinear contribution is emitted in a specific direction set by momentum conservation: in particular, the rephasing (black arrow) and non-rephasing (grey arrow) signals are shown at $\vec{k}_R = -\vec{k}_A + 2\vec{k}_B$ and $\vec{k}_{NR} = +\vec{k}_A - \vec{k}_B + \vec{k}_B$. (b) THz spectroscopy interaction geometry: the beams hit the sample collinearly, so that both the transmitted fields and the nonlinear signal are emitted in the same direction, and measured together by electro-optic sampling

quence will be fixed by the linear combination of the incident fields, due to phase matching, as $\vec{k}_S = n\vec{k}_A + m\vec{k}_B$. The different nonlinear signals are thus uniquely identified by their **k** vectors in real space. Given the interaction geometry and the pulses polarization, a certain detection direction corresponds to only one specific nonlinear signal.

The high divergence of THz beams however makes the separation of the incoming and outgoing beams in real space a challenge. A collinear geometry, where all beams shine on the sample at normal incidence, is much more practical. In this geometry (Fig.3.7.(b)) the transmitted field, including the pump beams and the nonlinearly emitted field, is all collected after the sample in the same direction, with $\vec{k}_S = \vec{k}_A = \vec{k}_B$: not only the rephasing and non-rephasing components can be measured at the same time, but so can signals from higher order nonlinear interactions. In a collinear geometry, the interaction length in the sample is also increased compared to a noncollinear set-up requiring strict phase matching: this bolsters n-wave mixing phenomena where intense pulses performing multiple interactions with the sample.

The different nonlinear signals - e.g., pump-probe signals, photon echoes and higher order interactions - can now all be measured all in one go, without necessarily selecting in advance by choosing the detector position, but they are also not identified by their location anymore. The use of phase resolved detection however allows the different signals to be identified in the reciprocal frequency space, once they have been isolated from the pumps in the transmitted field.

Extraction of the nonlinear signals

A schematic representation of a typical 2D THz measurement is shown in Fig.3.8.(a): it contains the full transmitted field including the pump beams A and B. The two time axes represent the real time t (horizontal axis) between the pulses and the EOS probe, and the delay time τ (vertical axis) between the pulses themselves. Since the EOS probe acts as a local oscillator, t corresponds to the real time in a 2D IR scheme, while τ stands for the coherence time.
Any nonlinear signal must stem from both pulses interacting together with the sample. In particular to achieve a $\chi^{(3)}$ interaction one of the pulses has to interact with the sample multiple times. The nonlinear signal can then be extracted from the transmitted field in the time domain, by isolating the contributions that only appear when both pulses can interact with the sample. By using choppers to selectively block the beams, the nonlinear signal E_{NL} is calculated as

$$E_{NL}(t,\tau) = E_{AB}(t,\tau) - E_A(t,\tau) - E_B(t) \tag{3.19}$$

where E_{AB} represents the transmitted field when both beams are present and E_A, E_B those when only one beam is interacting with the sample. Nonlinear signals will be expected to exist only in the causal range - the section of the 2D time domain after the passage of both pulses - shown as a green shaded area in panel (a).
The use of an heterodyne EOS probe as a local oscillator offers another advantage compared to a classical IR pump-probe set-up, where the probe both contributes to and reads out the nonlinear signal: the two THz pulses in 2D set-up can be considered on equal footing, without the limitations of using a strong pump and a probe in a linear interaction regime. Since the THz pulses don't directly interact with the detector, they can both be equally strong without risk of detection saturation.

Frequency vectors picture

To identify the nonlinear signals, we need first to define frequency vectors, following the concept of *Kuehn et al.* [22]. Using a fully field resolved detection technique we can measure the full phase of the electric field, so that we can identify the field phase fronts (shown as darker and lighter grey stripes in Fig.3.8). Beam B, coming at a fixed delay, has phase fronts orthogonal to the real time axis, while beam A has diagonal phase fronts.

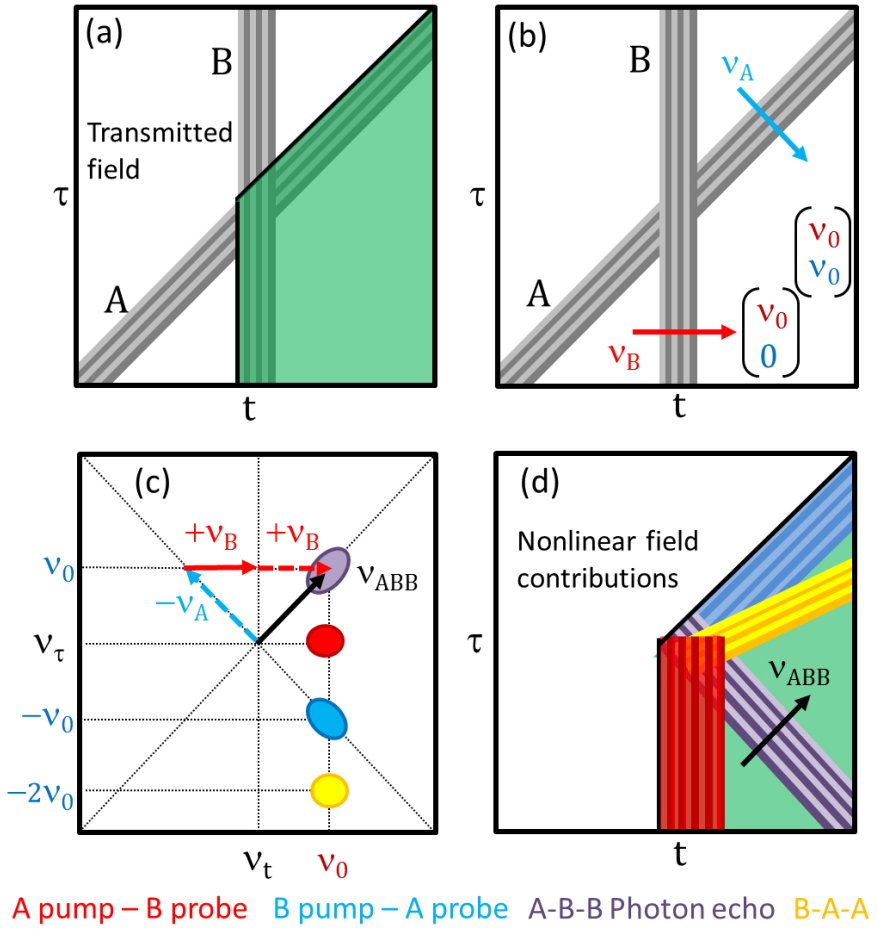

Figure 3.8: Concept of 2D THz spectroscopy: (a) Driving fields A and B ($\nu = \nu_0$) as a function of real time t (horizontal axis, EOS probe delay), and coherence time τ (vertical axis, delay between the pulses). Only the causal range (green area), after both pulses have interacted with the sample, contains nonlinear signals (b) The phase fronts (dark and light grey lines) define a frequency vector orthogonal to their direction. Pulse B, coming at a fixed delay, has a frequency vector $\nu_B = (\nu_0, 0)$ (red arrow). Pulse A, with diagonal phase fronts, has $\nu_A = (\nu_0, \nu_0)$ (blue arrow) (c) Nonlinear signal in frequency space: the detection (horizontal axis, ν_t) and interaction frequency (vertical axis, ν_τ) are defined by Fourier transform of t and τ. Adding up the frequency vectors of the driving fields, one finds nonlinear signals in different spots (colored circles). As an example, the A-B-B photon echo (purple spot) stems from $\nu_S = -\nu_A + +\nu_B + \nu_B = (\nu_0, \nu_0)$. Dashed arrows correspond to an interaction on the bra side. (d) Corresponding nonlinear fields in the time domain, retrieved by inverse Fourier transform.

The phase front direction identifies uniquely a frequency vector perpendicular to the phase fronts themselves, as shown in Fig.3.8.(b). Its components relay the oscillation frequency of the fields along the two time axes: pulse B shows no oscillations along the delay time axis, so its frequency vector is $\nu_B = (\nu_0, 0)$, while pulse A oscillates at ν_0 along both axes, since it has a variable time delay, resulting in $\nu_A = (\nu_0, \nu_0)$. In a fully 3D set-up frequency vectors also have a third component related to the waiting time T [23].
The nonlinear signal is now analyzed in frequency space by performing a double Fourier transform on both time axes. The real time transforms into the *detection frequency* ν_t, and the delay time into the *excitation frequency* ν_τ, which correspond to the first and second components of the frequency vectors respectively. in the 2D frequency space, the transmitted pump pulses are found in a position determined by their frequency vectors.
Since in a collinear geometry all different nonlinear contributions are measured together, they will all appear (if they can be excited in a certain sample) in the 2D spectrum (Fig.3.8.(c)). In the same way as k_S is determined by the pump pulses k-vectors in a non-collinear set-up, the frequency vectors of nonlinear signals in THz spectroscopy can be found by a linear combination of ν_A and ν_B:

$$\vec{\nu}_S = \pm n\vec{\nu}_A \pm m\vec{\nu}_B \tag{3.20}$$

Here n and m account for the possibility of multiple interactions, and the + or − signs are chosen with the same conventions as in Feynman diagrams. The nonlinear signal corresponding to a certain interaction sequence is located at the spot corresponding to its frequency vector.
The vectors can also be combined graphically, as shown in Fig.3.8.(c) for a rephasing A-B-B interaction sequence (purple spot): the A-B-B photon echo stems from an absorptive interaction of A on the *bra* side ($+\nu_A$), followed by absorption on the *ket* ($+\nu_B$) and emission on the *bra* side ($-(-\nu_B) = +\nu_B$) for B. By drawing the vectors with the correct sign (marking the bra interaction as dashed arrow) the spot corresponding to $\nu_{ABB} = (+\nu_0, +\nu_0)$ is identified. The same can be done for any other signal: as an example, in the figure are shown the B-A-A photon echo at $(+\nu_0, -2\nu_0)$ (yellow spot), and the two pump-probe signals (A pump-B probe in red and B pump-A probe in blue) in the same spectral position as the corresponding probe pulse.
It must be noted that the spot can not be identified uniquely: higher order interaction can end up in the same spot, for example by adding an even number of interactions with opposite sign. In many cases, such higher-order signals are comparably weak and, thus, can be neglected. For a clear separation, experiments with higher dimensionality are required, e.g. in an experiment with five

THz beams the lowest interaction has to be at the fifth order, but this is unpractical in terms of the experimental requirements and the very long measurement time necessary for higher order spectroscopies. However, it is often still possible to pinpoint the interaction sequence behind a specific signal based on physical constraints, e.g. allowed transition in the material, dipole strengths, symmetry relations, characteristic time evolution and so on.

Nonlinear signals in the time domain

Each contribution to the nonlinear signal can now be isolated and studied independently, by putting a filter around the relevant spot in the frequency plane and performing an inverse Fourier transform to retrieve the electric field in the time domain. This procedure has the added benefit of removing the noise collected in all other frequencies in the 2D frequency matrix, so that very weak nonlinear emissions of the order of tens of V/cm can still be analyzed.
The phase fronts of the nonlinearly emitted electric fields are determined by their frequency vector. Fig.3.8.(d) shows the electric fields corresponding to the spots in panel (c), with the same color convention for their phase fronts. While noise in the same spectral position would appear in the whole matrix in the time domain, any nonlinear emission from the sample will indeed appear only in the causal range, again shaded in green.
Our 2D THz spectroscopy concept allows for studying individually all the different contributions to the nonlinear signal, including possible higher order interactions. The experiment to be performed does not need to be selected in advance, but the THz fields can be used to interrogate the sample and record its response in all its complexity, and to analyze it in time or frequency with the techniques best suited to each specific experiment.
Due to this set-up affinity for multiphoton nonresonant interactions, using two beams it is still possible to observe third and higher order interactions in a pump-probe geometry, where each beam is interacting multiple times with the sample [22].

3.4 Experimental setup

We now discuss the specifics of the experimental implementation of our two-dimensional THz spectroscopy. In particular we will focus on the set-up used for the experiments presented in the following chapters - i.e. for 2D THz-THz spectroscopy and two-color THz-midinfrared 2D spectroscopy.

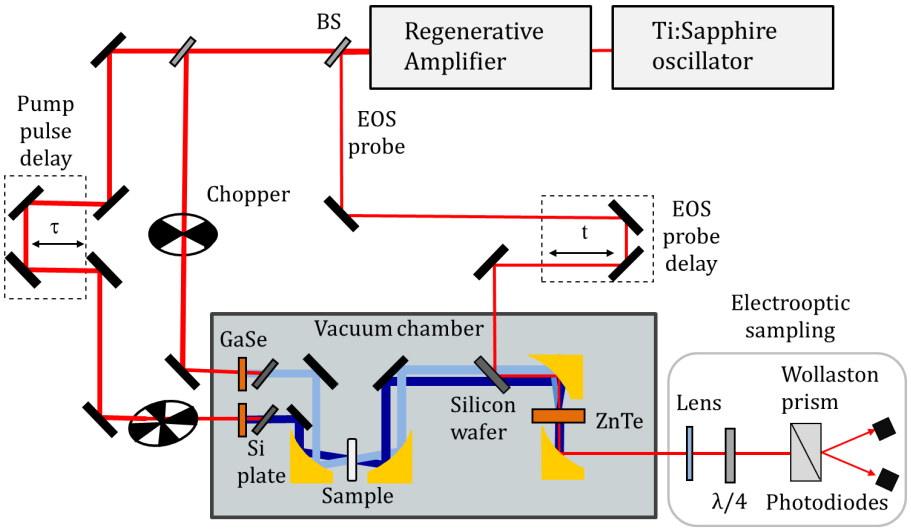

Figure 3.9: Setup for a two dimensional THz spectroscopy: the pump pulse from an amplified Ti:sapphire laser generates two THz beams by OR in GaSe, separated by an adjustable delay τ. After interacting with the sample, the transmitted field is measured by electro-optic sampling. By using two synchronized choppers on the pump beams we are able to extract the nonlinearly emitted field as a function of real time t and delay time τ.

3.4.1 2D THz-THz Setup

To generate coherent phase-locked THz pulses, we exploit phase-matched Optical Rectification (OR) in GaSe crystals pumped with an 800 nm pulse at normal incidence. In our set-up we use a Ti:sapphire oscillator, *Spectra Physics' Mai Tai SP*. It generates a beam centered at 800 nm, with a bandwidth of 60 nm and a time duration of 30 fs, at a 85 MHz repetition rate (Tab.3.1).
After traveling through a prism stretcher the beam is coupled to a *Spitfire* CPA [149] Ti:sapphire amplifier. The *Spitfire* is a 1 kHz regenerative amplifier sys-

	Repetition Rate	Pulse Energy	Peak Power	Pulse Length Δt	Bandwidth @ 800 nm
Oscillator	84 MHz	5 nJ	400 mW	30 fs	60 nm
Amplifier	1 kHz	4 mJ	4 W	50 fs	40 nm

Table 3.1: Technical specifications of the oscillator and amplifier pulses for 2D THz spectroscopy

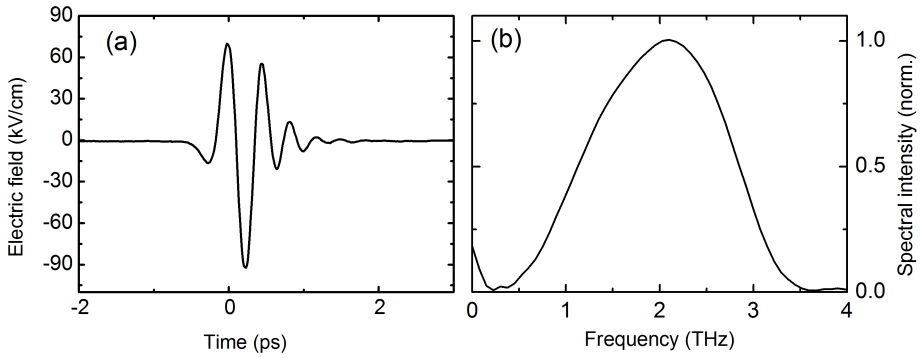

Figure 3.10: Typical THz electric field, in the time (a) and frequency domain (b)

tem, producing a powerful 4 W beam with 40 nm bandwidth, compressed down to 50 fs by a grating compressor.

As shown in Fig.3.9, the laser output (red line) is split into three components: 5% is split off to be used as an EOS probe, and the remaining beam is halved on another beam splitter into two independent beams, which are used for THz generation. The pump beams are chopped at 500 Hz and 250 Hz respectively, to enable independent measurement of the two THz beams, while a motorized micrometric delay stage allows to control the delay between the two pulses.

The two THz pulses (blue lines) are generated by OR in a 300 μm thick GaSe crystal as described in Sec.1.3.1. To generate the highest possible THz field, the GaSe crystal was pumped using the full output power of the amplifier beam, roughly 1.3 mW, resulting in a typical THz field amplitude of 90 kV/cm: a typical THz transient and spectrum is shown in Fig.3.10 (a)-(b). The generation, interaction and detection of THz beams are then carried out under vacuum conditions, since radiation in this frequency range is particularly susceptible to water vapor absorption.

An undoped silicon wave plate at the Brewster angle is used to block the pump beams, which are entirely reflected. The THz beams are then focused on the sample using a gold parabolic mirror, which minimizes geometrical and chromatic aberration in the focal plane. To ensure that the sample is placed in the focus and that the two THz beams are correctly overlapped in space, the system is benchmarked by measuring the intense pump-probe signal at 2 THz from multilayer graphene [148].

A second parabolic mirror collects the transmitted pulses, including the transmitted pump beams and any emission from the sample. All field components are restored to a collimated beam, which propagates to a second set of parabolic

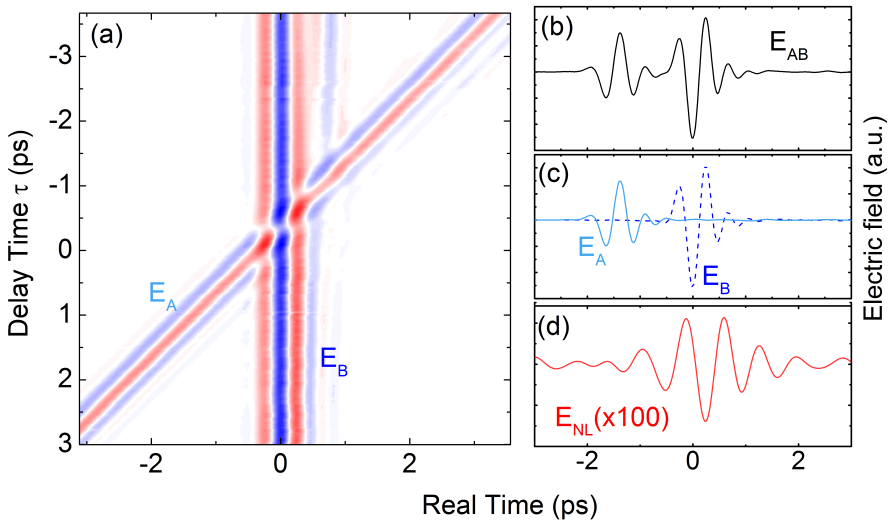

Figure 3.11: (a) Example of 2D THz spectroscopy signal, showing two THz electric fields as a function of real time t (horizontal axis) and delay time τ (vertical axis) (b) Electric field collected when both choppers are open (c) Single electric fields collected when only one beam is let through. The dashed blue line corresponds to beam B (vertical phase fronts in panel (a)) and the solid light blue to beam A (diagonal phase fronts) (d) Nonlinearly emitted electric field extracted by subtraction

mirrors to be focused on 300 μm ZnTe crystal. The choice of a thicker EO crystal is ideal for high sensitivity in the 2 THz range.
The amplifier EOS probe enters the vacuum chamber after traveling on a mechanical delay stage, so that the timing to the THz pulses can be scanned, and it is reflected on a Si plate to be focused on top of the THz beams by the same parabolic mirror. At full power ($\sim$ 20 mW), the probe beam would cause thermal damage when focused on the ZnTe crystal and saturate the balanced photodiodes used to measure the EOS signal: its intensity is reduced by IR filters to an appropriate level where where the diodes can operate in a linear regime.

The crystal thickness and duration of the probe pulse from the amplifier limit the system detection bandwidth. Nevertheless, in the 1-4 THz frequency range a 30 fs probe still allows for accurate detection, while the thick EOS crystal improves sensitivity for longer wavelengths.
A typical 2D signal is shown in Fig.3.11.(a): the horizontal axis represents the

	Repetition Rate	Pulse Energy	Peak Power	Pulse Length Δt	Bandwidth @ 800 nm
Oscillator	85 MHz	5 nJ	420 mW	14 fs	115 nm
Amplifier	1 kHz	1 mJ	1 W	25 fs	65 nm

Table 3.2: Technical specifications of the oscillator and amplifier pulses for two color spectroscopy

real time, or the delay of the probe with respect to the beams; the vertical axis is the time delay between the two. When both choppers are open, both fields are detected together (panel (b)), while when one of them is blocked they are detected separately (c). The nonlinearly emitted electric field (d) can then be extracted by subtraction.

3.4.2 Two-Color spectroscopy

To study nonresonant coherent control we wish to perform two-color spectroscopy with pulses at 1 THz and 20 THz. The set-up, shown in Fig.3.12, is conceptually similar to the 2D THz setup, with a few technical differences necessary to deal with the large mismatch in the frequencies involved. First and foremost, to support a large enough detection bandwidth an ultrashort oscillator pulse must be used as an EOS probe.
To this end, as a laser source we use a broadband Ti:sapphire oscillator, *Femtosource*'s *Integral Element*, providing 5 nJ pulses at an 85 MHz repetition rate. The pulses wavelength is centered at 800 nm, with an ultrabroad bandwidth of 115 nm in mode-locked operation. Using appropriate dispersive elements, such as negative dispersion dielectric mirrors, the oscillator pulses can be compressed to 12 fs time duration (FWHM), close to the diffraction limit for their bandwidth. The details about the oscillator pulse characteristics are summarized in table 3.2.
Out of the oscillator laser head, 5% of the beam is extracted using a beamsplitter to be used as a probe for EOS. The rest of the oscillator output coupled to a Ti:sapphire amplifier *Femtopower Compact PRO*, pumped by 1 kHz frequency doubled ND:Ylf lasers. The system this time is a multipass amplifier, so that the beam path length inside the amplification chamber is not so long as to prevent the use of an oscillator probe.

The pulses first go through a prism stretcher, ad then through the first four passes through the laser active medium. After this pre-amplification stage a Pockels cell reduces the repetition rate to 1 kHz. The beam is then split in

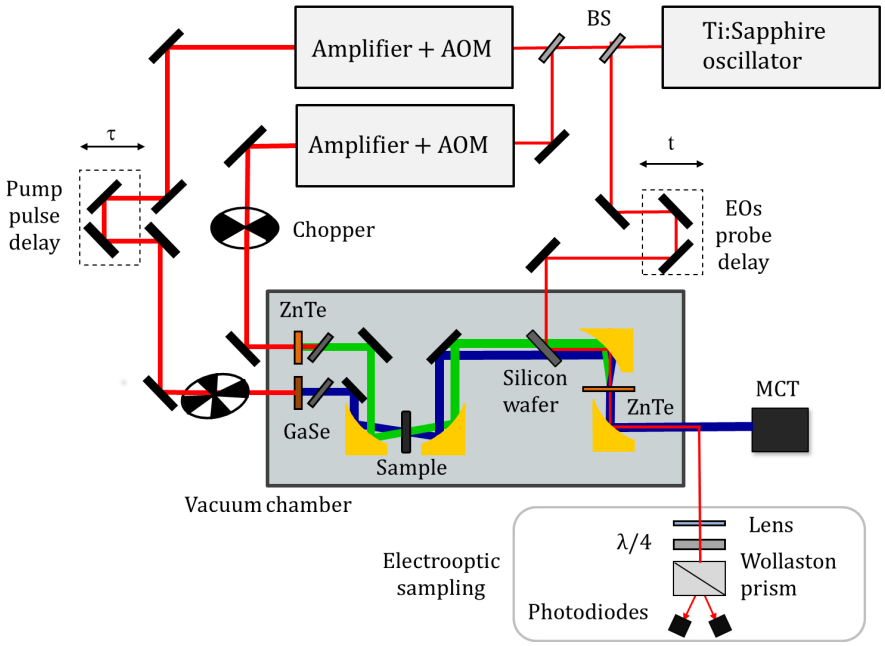

Figure 3.12: Setup for a two color THz-MIR 2D spectroscopy: to optimize THz and MIR generation the Ti:sapphire pumps come from two different amplifier systems, each with its own AOM to ensure an optimal pulse shaping.

two part, and each half is amplified in an independent system: this allows for tailoring of each pump pulse specifically to optimize either THz or mid-infrared generation using a dedicated *DAZZLER* AOM (Sec.1.3.2).
The *DAZZLER*s output, strongly reduced in intensity, are then amplified by 5 further passes through two separate Ti:sapphire crystals. Finally, the beams are compressed to roughly 25 fs, resulting in two beams of up to 1 mJ of energy, with a peak power of 1 W at full amplifying power. Depending on the specific pulse shaping, the output energy and time duration of the beam are adjusted in order to optimize the characteristics of the generated infrared radiation.

Like in the THz 2D setup, the amplified beams are chopped at 250 Hz and 500 Hz. THz radiation (in blue in the set-up scheme) is generated by OR in a 1 mm thick ZnTe crystal, resulting in a typical electric field amplitude of 30 kV/cm centered around 1 THz(Fig.3.13.(a)-(b)). Mid-infrared radiation (in green) is produced by DFG between cross-polarized pump components in a 200 μm GaSe crystal tilted at 43°: the incidence angle on the nonlinear crystal is used to tune its emission around 21 THz. Contrary to the low frequency case, MIR frequencies are generated at a much higher efficiency: the amplifier beam at full power can easily generate MIR output of the order of MV/cm,

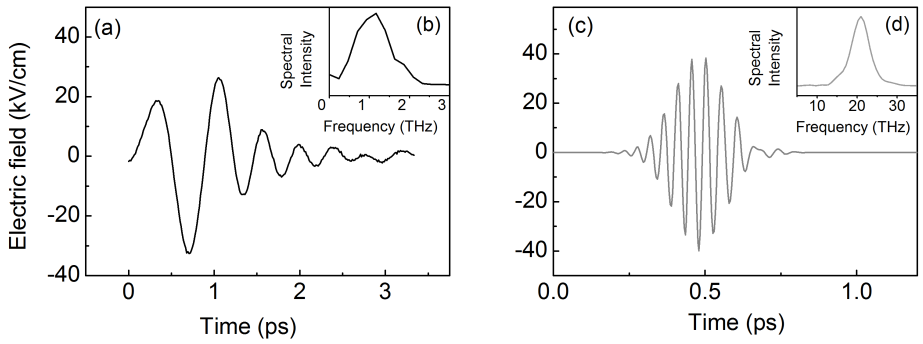

Figure 3.13: Time dependent transient and spectrum of the THz (a)-(b) and MIR (c)-(d) electric fields.

typically attenuated to less then 50 kV/cm to avoid a complete bleaching of the interaction with the sample. A representative mid-infrared field is shown in Fig.3.13.(c)-(d).

The beams are both focused on the sample and on the EO crystal using again two sets of gold parabolic mirrors. They are ideal for this purpose due to their broadband high reflectivity and focusing geometry: beams parallel to the parabola axis are focused in the same focal spot, regardless of their wavelength. For a fully field-resolved EOS detection, the ultrashort probe pulse focused together with the strong infrared fields on a 10 μm [100] ZnTe crystal grown on a [111] ZnTe substrate. The thin electrooptically-active layer ensures that the induced birefringence is accumulated over a thickness much lower than the coherence length of both THz and MIR radiation, allowing both to be detected at the same time.

As a secondary detection scheme, the transmitted beam was focused with a Germanium lens on a HgCdTe detector cooled to T = 77 K to perform frequency-integrated measurements of the transmitted MIR intensity - with retaining any phase information. Since the photodetector sensor is only sensitive to radiation higher then 13 THz, it can not be used to detect our THz beam.

3.5 THz spectroscopy in novel regimes

The peculiar characteristics of the pulses used for THz multidimensional spectroscopy allow to investigate systems in a context that is not accessible through conventional 2D spectroscopy. In particular, the THz facility for nonresonant interaction in the nonperturbative regime, the often collective nature of the material response and the long lived character of THz polarization quickly bring

THz measurements outside the applicability of the approximations most commonly employed in nonlinear IR spectroscopy.

Beyond the semi-impulsive limit

Typically, optical or infrared pulses are significantly shorter than the characteristic time evolution of the phenomena they excite. This allows the typical time delays of IR spectroscopy to be much longer than the pulse duration, resulting in a well defined time ordering of the interactions. Fig.3.14.(a) show two such pulses, pulse B arriving at time 0 in a lighter shade of blue and pulse A, darker, at a variable time delay.

In the semi-impulsive limit, the time ordering strictly defines the position of the various wave mixing signals with respect to the delay time: for example a rephasing contribution in the form ABB (black line) can exist only when pulse A arrives first on the sample, i.e. for positive time delays. Panel b shows a simulated photon echo response from a two level system. The nonlinearly emitted electric field is plotted as a function of real time t on the horizontal axis, and of delay time τ on the vertical: the signal appears only in the causal range, after both pulses have interacted with the sample, and in the expected quadrant with $\tau > 0$.

If however the driving pulses are longer than the pulse separation, strict time ordering does not apply. In a densely packed solid medium this can be due to local field corrections, accounting for the influence of nearby polarized oscillators on the electric field on a specific atom in the material. in this case the driving field is composed of the external field together with the emission from the polarization free induction decay (Fig. 3.14.b).

The time resolved response in a material where local field corrections are dominant has been described by *Wegener et al.* [150] for 4WM in a noncollinear geometry, but their findings are readily adapted to the THz range. Considering again an ABB interaction, it can now be observed even at negative time delays when pulse B shines first on the sample. Even though when pulse B arrive no photon from pulse A is present, later on A can still interact with the leftover polarization excited by B. Panel (d) shows a nonlinear signal calculated for long lived driving pulses, which is present even at negative time delays where only the BAA field, with different phase fronts, would be expected.

Beyond the RWA: nonresonant interaction

In conventional IR spectroscopy, all nonresonant contributions are neglected: the external electric field is assumed to be resonant with the transition under investigation. In this scenario, the RWA allows to discard contributions

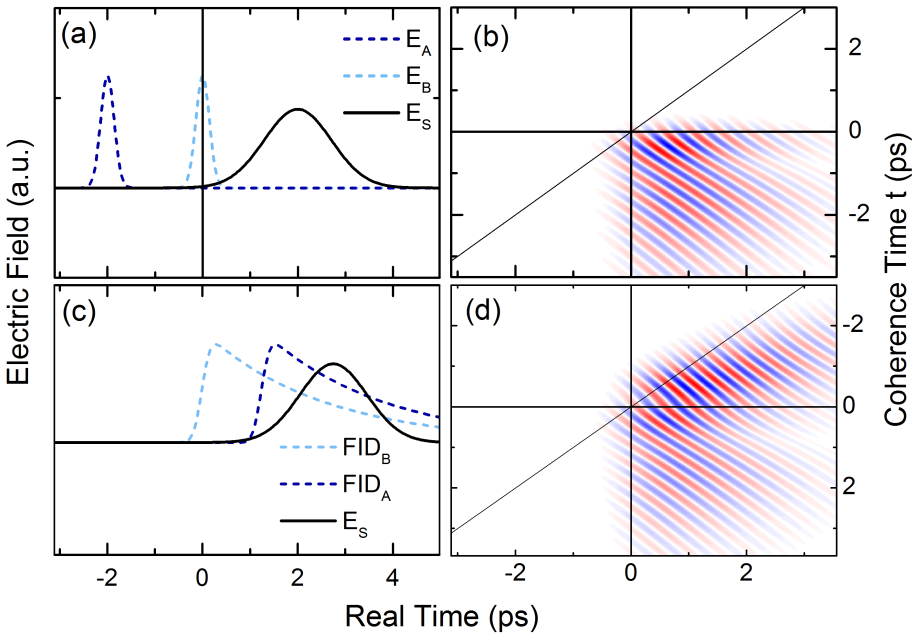

Figure 3.14: Schematic difference of the nonlinear response in or out of the semi impulsive limit. (a) Two driving pulses in the semi-impulsive limit, in blue with the real time axis centered on pulse B (dashed light blue line), and delay time assuming positive values when pulse A (dashed dark blue) comes first. The ABB photon echo response (solid black line) appears after the second pulse. (b) 2D plot of a typical photon echo signal as a function of real time t (horizontal axis) and coherence time τ (vertical axis): the only rephasing contribution is at positive delays. The maximum and minimum value of the field, in arbitrary units, appear respectively red and blue in the color scale. (c)Corresponding situation when the driving field is long lived, out of the semi impulsive limit. The ABB interaction sequence is possible even when pulse B comes first. (d) Corresponding nonlinear field, showing a rephasing ABB contribution even at negative delay times.

from rapidly oscillating diagrams ($\propto e^{-i2\omega t}$), and to keep only the slow varying terms $\propto e^{-\Gamma t}$. However THz radiation can easily drive interactions in a highly nonresonant regime [8, 24], provided the field is strong enough to access the nonperturbative regime. In that case, owing to the collective character of THz phenomena and to the large portion of band structure accessible by THz excitation, the nonresonant field can induce Zener tunneling or allow access to multiple quantum coherences.

In Ch.3 of this work we investigate how a highly nonresonant THz field can be

used to coherently control the mid-IR emission of GaAs quantum wells: however to describe such interaction, the rotating wave has to be abandoned in favor of describing the full interaction of the system density matrix with the external fields.

Beyond the $\chi^{(3)}$ limit: higher order multiple interactions

In the IR range it is usually assumed that each pulse performs only one interaction with the sample, so that a third-order $\chi^{(3)}$ interaction can be studied by conventional spectroscopy using a variety of 3-pulse schemes. However electric fields in the THz range often experience high coupling to electronic dipoles, leading easily to multiple interactions even with electric fields of comparatively moderate amplitude. In graphene $\chi^{(5)}$ and higher processes lead to high harmonic generations [151, 152], while in semiconductors such as InSb processes as high as $\chi^{(11)}$ have been observed using three THz pulses [153].

When an interaction requires diagrams at high order, or when the dominant order can not be defined - e.g., for the Rabi flopping of a saturated transition - the perturbative description can soon become unpractical, as the number of diagrams involved increases and the calculations get more cumbersome. Instead of calculating the response functions at different orders in a Mukamelian framework [127], the physics behind the observed nonlinear signals can be better understood by pursuing a solution of the full Liouville equation.

Such an approach is only enabled by the collinear character of THz multidimensional spectroscopy, where the nonlinear response at multiple orders is collected in a single experiment.

Beyond the perturbative regime

An interaction is said to be in the perturbative regime when the energy of the external electric field E_{opt} is significantly smaller then the internal energy of the system, $E_{opt} << E_{int}$. If that is the case, then it is convenient to describe the system nonlinear response in terms of its n-th order susceptibilities $\chi^{(n)}$, writing the polarization as $P = \epsilon_0 \sum_n \chi^{(n)} E^n$.

When the electric field energy is high enough to have $E_{opt} \sim E_{int}$, the system will be driven to saturation. The nonlinear response will then include contributions from all susceptibilities up to a high order, as happens for example during Rabi oscillations [22]. A perturbative expansion is then not an adequate description of the system response: as this is easily the case in the THz range, it is necessary to describe the full interaction of the external electric field with the system density matrix beyond a perturbative approach.

The next chapters will highlight applications to coherent quantum control and soft modes in molecular crystals. The interaction regimes we explored are accessible only with the specific capabilities of coherent multidimensional time domain spectroscopy in the THz range, granting insight on the highly collective nature of the nonlinear response in very disparate materials.

Chapter 4

Nonresonant coherent control of mid-infrared emission from GaAs quantum wells

Coherent control of quantum processes has long been a thriving field of research. generating a quantum mechanical superposition of the envelope wave functions of the optically coupled subbands Optical polarizations can be manipulated by exploiting quantum mechanical interference of wave functions, by exciting them coherently: coherent control can be achieved by having light fields interacting with the polarization within its dephasing time, before loss of coherence prevents further interaction [154]. Since dephasing times in condensed matter are usually on a sub-picosecond time scale, coherent control has become an accessible pursuit only after the technology for ultrafast interaction became widely available.

Since the development of controlled pulse shaping of laser pulses on a femtosecond time scale, coherent control has been demonstrated in a variety of systems, including exciton emission in quantum wells [155–158] and quantum dots [159], and spatial control of photoelectron transport [160]. It can be used to influence phononic excitations in the THz range [161] and to modify the emission of plasma THz sources [162]. Further examples include numerous applications to photochemistry via control of molecular orientation both in liquid [163] and gas phase [164]. However, up until now most studies have focused on resonant

excitation schemes of coherent control. At most quasi-resonant schemes have been investigated, such as adiabatic passage techniques for population transfer, which uses carefully tailored pulses of different colors to achieve a specified final population state in a system [165].
Powerful THz pulses can be used to directly control low frequency excitation and transient states in solids [166, 167], even nonresonantly exciting populations with a much higher energy then the THz photons [6]: the high-intensity THz beams generated in our setup make nonresonant control schemes a very promising endeavor. In this chapter we will discuss how, in the framework of the Autler-Townes shift in a rapidly varying electric field, a nonresonant THz beam can influence the intersubband (IS) polarization in GaAs quantum wells, leading to enhanced mid-infrared absorption and to a THz controlled phase shift of the linear and nonlinear emission of the IS transition. In a fully nonresonant manner, the THz radiation can be used to coherently control, and even switch on and off, resonant emission of radiation.

4.1 The Stark effect in atoms

In this section I will describe first the Stark effect in atoms in an electrostatic fields, before moving on the the Autler-Townes model for atoms in a rapidly varying electric field.

4.1.1 Stark effect in a static electric field

An atomic system system interacting with a static electric field undergoes a shift of its energy levels and a splitting of degenerate spectral lines [168]. We consider a perturbation small enough compared to the inner atomic forces, so that it can be treated with perturbation theory. The perturbed energy level can be calculated by solving

$$(H_0 + V)|n\rangle = E_n|n\rangle \tag{4.1}$$

where H_0 is the system Hamiltonian, the external perturbation is $V = -\mathcal{E} \cdot \mu$ and μ is the atom induced dipole moment and $\mathcal{E}$ is the electric field. For a non-degenerate initial state (e.g. the ground state of the hydrogen atom) the equation supports a non-zero first-order solution, giving an energy shift for level n:

$$\delta E_n^{(1)} = -\mathcal{E}\mu_{nn} \tag{4.2}$$

where μ_{nn} is the matrix element of the dipole operator. Since the energy correction is proportional to the electric field, this is called *linear Stark effect*.

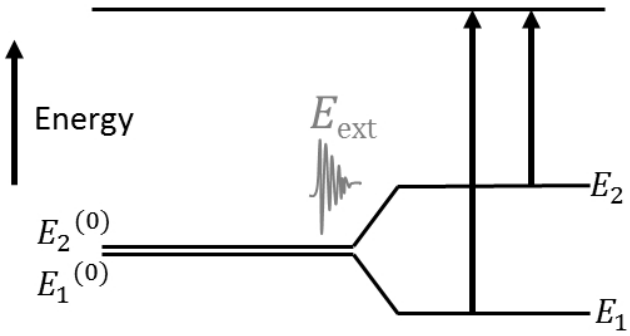

Figure 4.1: Splitting of two close-by energy $E_1^{(0)}$ and $E_2^{(0)}$ (left side) levels in presence of a strong electric field E_{ext} (right side).

The second order correction, which is proportional to the square of the electric field, gives the *quadratic Stark shift*:

$$\delta E_n^{(2)} = \mathcal{E}^2 \sum_m \frac{|\mu_{mn}|^2}{E_n^{(0)} - E_m^{(0)}} \tag{4.3}$$

For degenerate energy levels typically the linear term will be null, while the second order correction, which depends on the angular momentum quantum number, will break up the level degeneracy [169]:

$$\delta E_n^{(2)} = (a + Bm_J)\mathcal{E}^2 \tag{4.4}$$

We now consider a two level system with unperturbed levels $E_1^{(0)}$ and $E_2^{(0)}$, which are close to each other in energy. Upon application of an electric field, the two levels mix with each other resulting in two levels

$$E_{1,2} = \pm\frac{1}{2}\sqrt{(E_1^{(0)} - E_2^{(0)}) + 4|V_{12}|^2} \tag{4.5}$$

The energy separation of the perturbed levels is now larger then the original separation. The scheme in Fig.4.1 shows the effect of an external electric field on closely spaced levels: an optical transitions starting from the unperturbed levels will split up resulting in a Stark doublet.

4.1.2 Stark effect in rapidly varying fields: the Autler-Townes model

The Stark effect caused by an electrostatic field can easily be treated with time independent perturbation theory. To work with a fully time-dependent electric field, it is necessary to use more sophisticated methods.

The problem was first studied by Autler and Townes [170], who gave an approximate solution using Floquet's Theorem [171], the analogue in time to Bloch's theorem. When considering a sinusoidal electric field, the perturbed wave functions will also be periodic in time. The wave function of mixed states in the form:

$$\Psi = T_a(t)U_a + T_b(t)U_b \tag{4.6}$$

where U_a and U_b are the unperturbed wave functions of the two levels being admixed, which depend only on space coordinates. The time-dependent T functions are periodic:

$$T_a(t) = e^{i\lambda t}\sum_n A_n e^{-in\omega t} \tag{4.7}$$

The expression for $T_b(t)$ is analogous, with a different set of coefficients B_n. Autler and Townes find a complete set of solutions by retrieving the λ, A and B coefficients recursively through continuous functions. Once they have reconstructed the wave fractions, they can obtain the probability of finding the system in a certain state at any given time. The system oscillates between the mixed states defined by the A and B terms, and transitions to an higher lying lever at E_c are observed at frequencies $\omega_c + \lambda_{a,b} - K\omega_{ext}$, where K is an integer. The main spectral line at ω_c is shifted by λ, while additional lines for $K \neq 0$ have an intensity proportional to the $|A_K|^2$ coefficients. In general, if for the A set of solution we consider even K, set we will need to use odd K for the B to have a complete solution, and vice versa.

The solutions have the structure of a Stark-shifted level with sidebands shifted by K photons of the external electric field. This can easily be visualized in a dressed state picture [169, 172], where each transition is accompanied by absorption or emission of k photons at the external field frequency. We can then consider the new unperturbed states of the [*atom + field*] system including K photons:

$$E^{(0)}_{K,n} = E^{(0)}_n + K \cdot \hbar\omega \tag{4.8}$$

As we did for a static field, we consider two levels with similar energy. The second order energy corrections are calculated through second order perturbation theory, only this time starting from dressed states:

$$\Delta E^{(2)}_{k,1} = \frac{\mathcal{E}^2|\mu_{12}|^2}{4}\left(\frac{1}{E^{(0)}_1 - E^{(0)}_2 - \hbar\omega} + \frac{1}{E^{(0)}_1 - E^{(0)}_2 + \hbar\omega}\right) \tag{4.9}$$

$$\Delta E^{(2)}_{k,2} = \frac{\mathcal{E}^2|\mu_{12}|^2}{4}\left(\frac{1}{E^{(0)}_2 - E^{(0)}_1 - \hbar\omega} + \frac{1}{E^{(0)}_2 - E^{(0)}_1 + \hbar\omega}\right) \tag{4.10}$$

The sign of the term $E_1^{(0)} - E_2^{(0)} - \hbar\omega$ determines how the energy level separation is affected by the shift. If the external field phonons have lower energy than the transition ($\hbar\omega < E_1^{(0)} - E_2^{(0)}$) then the two perturbed levels will be further apart in energy, and the transition will be blue-shifted. On the other had, if $\hbar\omega > E_1^{(0)} - E_2^{(0)}$ the levels will end up getting closer, and the transition will be red-shifted. In terms of dressed states, this effect can be interpreted as level repulsion between a dressed ground state $|n = 1, \hbar\omega\rangle$ and the first excited state $|n = 2, 0\rangle$: as shown in Fig.4.2.(a), the dressed state of a "red" pump photon will be lower than the excited state, which will be pushed up by level repulsion, while a "blue" pump photon will push the excited state down. The solid black line in the figure shows the transition energy, which is increased by a low frequency perturbation and decreased by a high frequency one.

Accounting for the level repulsion effect, the displaced energy levels can be explicitly written as:

$$E_{k,1} = \frac{(2k+1)\hbar\omega}{2} \pm \frac{1}{2}\sqrt{(E_1^{(0)} - E_2^{(0)} - \hbar\omega)^2 + \mathcal{E}^2|\mu_{12}|^2} \tag{4.11}$$

$$E_{k,2} = \frac{(2k-1)\hbar\omega}{2} \pm \frac{1}{2}\sqrt{(E_2^{(0)} - E_1^{(0)} + \hbar\omega)^2 + \mathcal{E}^2|\mu_{12}|^2} \tag{4.12}$$

The Autler-Townes shift has been observed in numerous occasion, from the pioneering measurements of Autler and Townes themselves in the microwave range and dynamic Stark shifts in various atomic systems [169].
The transition energy shift due to the external electric field results also in a frequency shift of radiation emitted by the transition. In Fig.4.2.(b)-(c), we show the free induction decay emission from a transition excited by a resonant pulse. The emitted field (solid black line) is modified by the presence of a non-resonant field of either higher (b) or lower (c) frequency: the detail of the model used for the calculation are discussed in Sec.4.2.3. The lower frequency perturbation (red line) causes a blue shift of the transition, and as a result the emitted field phase is shifted to earlier times compared to the unperturbed FID. On the other hand for a high frequency perturbation (blue line), the emission is red shifted, and the free induction decay builds up a phase delay. These effects on the emitted field phase are not critical for linear absorption, but they will prove to be of essence for time resolved 2D spectroscopy

4.2 Intersubband transitions in quantum wells

Low-dimensional semiconductor heterostructures are important model system for the study of quantum coherences in solids. Since the nineties, advances

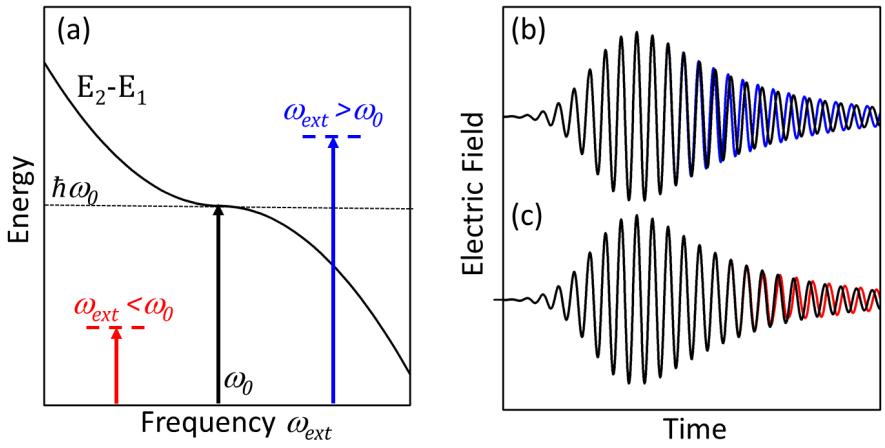

Figure 4.2: (a) Schematic of the Stark effect shift in the Autler-Townes picture. We consider two level energy levels separated by $\hbar\omega_0$ (black arrow), interacting with an external electric field with frequency ω_{ext}. The solid black line shows how the transition frequency is changed as a function of the frequency of an external field. The lower level is moved to a dressed state by an external photon with energy either lower (red arrow) or higher (blue arrow) than the unperturbed transition. Due to level repulsion, the upper excited state is then moved respectively to higher and lower energies, resulting in a blue shift (for a low energy nonresonant interaction) or a red shift (high energy) of the transition frequency. (b) Electric field emitted by the transition (solid black line) and its change due to an external electric field of higher frequency, resulting in a red shift (blue line) (c) Change of emission (red line) due to a perturbation at lower frequency, resulting in a blue shift compared to a resonant field (black line)

in crystal growth techniques have made mesoscopic semiconductor structures available which allow to confine electrons in three (*quantum dots*), two (*quantum wires*) or one dimension (Quantum Wells, QWs). QWs in particular confine electrons and holes in 2-dimensional wells: the small length of the confinement, comparable to the de Broglie wavelength of the carriers, makes them an excellent systems for studying quantum properties and polarization control [173].

By layering semiconductors with slightly different energy gaps, well structures are created in the valence and conduction energy bands. Fig.4.3.(a) shows the conduction band of a quantum well structure: the height of the potential barrier is determined by the difference in energy, and the well size L along the spatial confinement direction z is fixed by the thickness of the lower energy gap

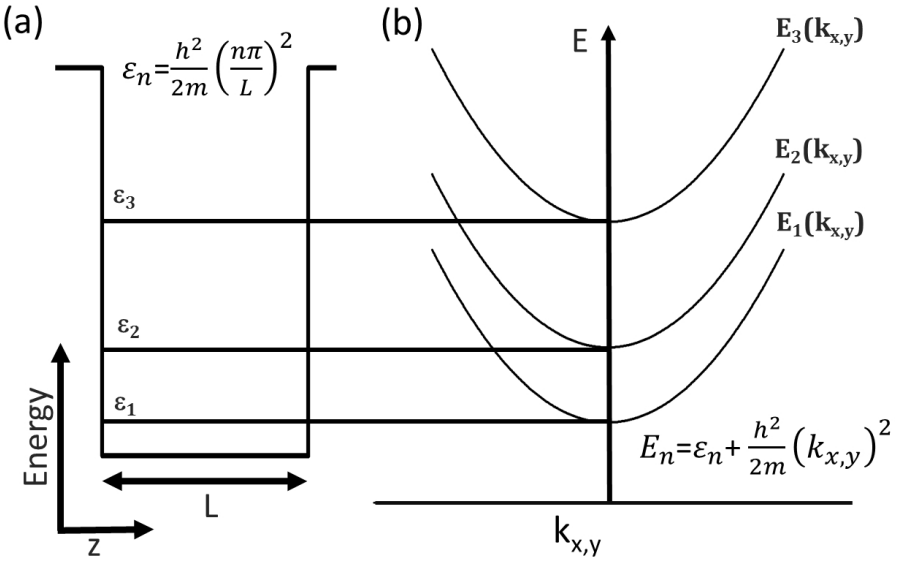

Figure 4.3: (a) Energy levels in the conduction band of a quantum well with confinement length L in the z direction (b) In-plane dispersion as a function of the wavevectors in the free x and y directions.

layer. Due to confinement, the energy values in the well are quantized and form an subband: in an ideal well with infinite energy barrier, the electronic wave functions are standing waves with fixed wavenumbers values. The energy levels in the well have energy:

$$\epsilon_n = \frac{h^2}{2m_{eff}}\left(k_{n,z}\right)^2 = \frac{h^2}{2m_{eff}}\left(\frac{n\pi}{L}\right)^2 \tag{4.13}$$

where m_{eff} is the effective mass of the electron.
In the x and y directions the particle is not confined, and in-plane dispersion is parabolic as shown in Fig.4.3.(b). The full electron energy is $E_n = \epsilon_n + \frac{h^2}{2m_{eff}(k_{x,y})^2}$.
The levels in the sub-band are connected through dipole-allowed optical intersubband (IS) transitions: the nearly parallel in-plane energy dispersion for different subband means that the IS transition energy is independent of $k_{x,y}$. The transition frequency $h\Delta\nu_{m,n} = \epsilon_m - \epsilon_n$ is set by the well width in the confinement direction z, resulting in narrow absorption lines
IS transition have since been studied extensively: they are attractive as sources for QCLs [174] and THz lasers [175]. More recently the Stark effect in QWs has also become of experimental interest, with results concerning excitonic Autler-Townes splitting [176, 177] and linear THz effect on population transfer in IS

transitions in single and multiple QWs [178, 179].
As we are going to discuss, when driven to a nonlinear regime of interaction an IS polarization can exhibit an oscillatory behavior, alternating between net absorption and emission in a Rabi oscillation [180]. Since most QWs are designed with barriers of the order of hundreds of meV, most IS transitions fall in the MIR range: powerful pulses in this spectral region became available relatively recently, preventing from accessing a nonlinear interaction regime in QWs. The first experimental observation of a Rabi flop was achieved by *Luo et al.* [181] in GaAs QWs. The critical influence of radiative coupling on quantum wells absorption has been is described in [16], showing how for highly doped quantum wells a high driving field does not cause a further absorption increase, due to a significant reduction of the local field inside the sample caused by reflection on the quantum wells layers. The effect of nonresonant excitation on the nonlinearity of an IS polarization has not, as of yet, been investigated experimentally.

4.2.1 Optical Bloch equations for a two-level system

To describe the interaction of a QWs system with an electric field (resonant or non-resonant) we use the density matrix formalism. Neglecting the IS transition second excited state, we consider the density matrix for an ensemble of two level systems [182]: this allows to treat the interaction nonperturbatively, including all orders of nonlinearity, but it neglects all many body effects and correlations among the QWs.We write ρ as:

$$\rho = \begin{bmatrix} \rho_{11} & \rho_{12} \\ \rho_{21} & \rho_{22} \end{bmatrix} \tag{4.14}$$

where the diagonal elements ρ_{11} and ρ_{22} represent the populations of the ground state and first excited state, and the nondiagonal elements ρ_{12} and ρ_{21} represent coherences between the two states, i.e. polarizations. Since the density matrix must be Hermitian, $\rho_{21} = \rho_{12}*$, where $*$ denotes complex conjugation. Since the total population of the system is 1, $\rho_{11} = 1 - \rho_{22}$. We then write:

$$\rho = \begin{bmatrix} 1 - \rho_{22} & \rho_{12} \\ \rho_{12}* & \rho_{22} \end{bmatrix} \tag{4.15}$$

The two level system is coupled with an electric field $\mathcal{E}$, so on top of the Hamiltonian H_0 of the non-interacting system we include the coupling through an interaction Hamiltonian H_E

$$H = H_0 + H_{\mathcal{E}} = \begin{bmatrix} \epsilon_1 & \mu \cdot \mathcal{E} \\ -\mu \cdot \mathcal{E} & \epsilon_2 \end{bmatrix} \tag{4.16}$$

Here ϵ_1 and ϵ_2 are the energy of the two levels coming from the unperturbed Hamiltonian H_0. The off-diagonal components are due to the interaction Hamiltonian $H_\mathcal{E}$, where μ is the IS transition dipole moment and $\mathcal{E}$ is the electric field, which in our case is composed of both resonant and nonresonant components.
The time evolution of the density matrix is determined by the Liouville-von Neumann equation.

$$\frac{d}{dt}\rho = \frac{i}{\hbar}[H, \rho] \tag{4.17}$$

We can now calculate the response of the two-level system interacting to an electric field resonant to the transition. To do so we solve two coupled differential equations for ρ_{22} and ρ_{12}, the optical Bloch equations (OBEs). The first one describes the time evolution of the polarization:

$$\frac{\partial}{\partial t}\rho_{12} = \left(i\omega_{12} - \frac{1}{T_2}\right)\rho_{12} - i\frac{\mu\mathcal{E}(t)}{\hbar}(1 - 2\rho_{22}) \tag{4.18}$$

And the second the evolution of the excited state population:

$$\frac{\partial}{\partial t}\rho_{22} = -\frac{1}{T_1}\rho_{22} + 2\frac{\mu\mathcal{E}(t)}{\hbar}Im(\rho_{12}) \tag{4.19}$$

Here ω_{12} is the IS transition frequency. To account for relaxation processes, dephasing was added phenomenologically: here T_1 represents the lifetime of the excited population and T_2 is the dipoles dephasing time.
These equations support an oscillatory solution for the polarization and excited state population. If the driving field is strong enough to excite a significant portion of the systems' electrons, the excited state population is proportional to a sinusoidal term $\sin^2(\Omega_R t/2)$: the Rabi frequency $\Omega_R \propto \mathcal{E}$ defines the period of an oscillation between between absorptive phases, when the excited state population is growing, and emittive phases, when it is decreasing. The instantaneous Rabi frequency is defined as:

$$\Omega_R(t) = \mu\mathcal{E}(t)/\hbar \tag{4.20}$$

We now consider a thin layer of QWs with sheet carrier density n_e. The macroscopic excited polarization is proportional to the density matrix coherence ρ_{12}:

$$P = 2n_e\mu Re(\rho_{12}) \tag{4.21}$$

The time dependent polarization generates a macroscopic current $j = \partial P/\partial t$, which emits a macroscopic electric field. In a thin layer, the emitted electric field is directly proportional to the current density, i.e. to the charge velocities, and not to its time derivative [183]. In this case the emitted field is:

$$E_{em} = -\frac{1}{2\epsilon_0 c}\frac{\partial P}{\partial t} = -\frac{n_e\mu}{\epsilon_0 c}\frac{\partial \rho_{12}}{\partial t} \tag{4.22}$$

For a strong enough electric field, the polarization also shows an oscillatory behavior, which is reflected in the phase of the re-emitted electric field [181]: during an absorptive phase $d\rho_{12}/dt > 0$ and E_{em} is out of phase with the driving electric field. Conversely, after reaching full population inversion, the excited state population will decrease, giving $d\rho_{12}/dt < 0$: the emitted and driving field are now in phase, giving rise to an enhancement of the transmitted field.
To describe the build up of Rabi oscillations we define the pulse area Θ:

$$\Theta(\Omega_R) = \frac{\pi}{2} \int |\Omega_R(t)| dt \tag{4.23}$$

A pulse strong enough to drive the system to full population inversion will have a pulse area of 1π. A pulse area of 2π corresponds to a full Rabi oscillation, from absorption to emission, an excitation which drives a full de-excitation and achieves a second population inversion has a 3π area, and so forth.

4.2.2 Nonresonant perturbation of a QW potential

We will now consider the effect of a small linear perturbation on the quantum wells potential. This is a similar problem to the Autler-Townes effect, but in this case instead of using the dressed state picture we can directly consider the effect of the perturbation on the shape of the potential well. This amounts to a different gauge choice: a resonant field exciting the IS transition will interact with a distorted potential, which already includes the quasi static field as a small perturbation.
The effect of nonresonant radiation on a QW potential has also long been of interest: calculations predicted changes in dipole moment and absorption frequency [184], which were soon observe by FTIR in good agreement with theory [185]. More detailed calculations for have been carried out by different authors [186–188] using a laser-dressed potential model to describe distortions to the QWs potential due to electric fields of different strength. By expanding the time-periodic potential in Floquet states they derive analytic solutions for the wave functions in highly distorted potentials, retrieving again an expected blue shift of the transitions for fields of moderate strength. They expect a decrease in infrared absorption and coupling to the electric field, together with a Stark blue shift. For higher laser dressing parameters $\alpha \propto \mathcal{E}/\omega_{ext}^2$, higher field intensities or frequencies are able to create transient double quantum well structures.
The effect of applying a small static bias $V_0(x) = \epsilon \cdot x$ to the QWs potential can be evaluated through first order perturbation theory, using as a starting point the wave functions and energy levels of a simple finite well potential as $E_n = E_n^{(0)} + \langle \psi_n^0 | V_0 | \psi_n^{(0)} \rangle$ and $\psi_n = \psi_n^{(0)} + \sum_{m \neq n} \frac{\langle \psi_m^0 | V_0 | \psi_n^{(0)} \rangle}{E_n^{(0)} - E_n^{(0)}} \psi_m^{(0)}$. The results are

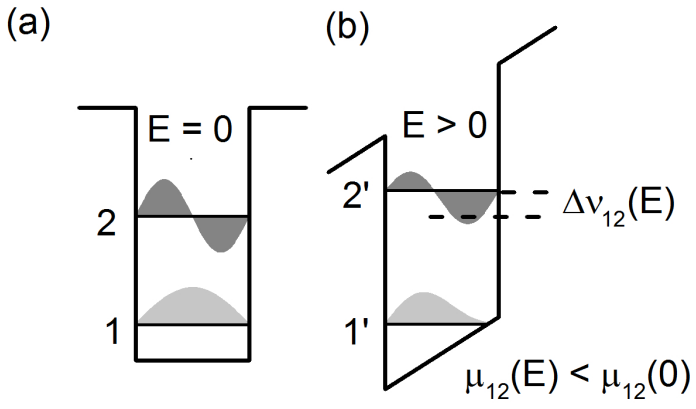

Figure 4.4: Schematic view of a quantum well with two bound states, with position on the horizontal axis and energy on the vertical. (a) Wave functions of the unperturbed IS levels (b) Tilted QW under a quasi static linear perturbation: the transition frequency is changed by $\Delta\nu_{12}$, and the dipole moment $\mu = \langle 1|z|2\rangle$ is decreased due to a reduced overlap between the levels wave functions (shown as grey shaded areas).

shown schematically in Fig.4.4: the static electric field tilts the bottom of the well, causing the ground state to drop to lower energy, while the excited state energy is slightly raised. Overall the external electric field causes a blue shift of the IS transition energy [184].

At the same time the wave functions are displaced from their original sinusoidal form (represented in Fig.4.4.(a) as grey shaded areas), becoming asymmetric (Fig.4.4.(b)): the overlap between the probability density in space of the first and second intersubband level is decreased. This reduces the dipole moment $\mu = \langle 1|z|2\rangle$, and consequently the absorption probability.
For a small linear distortion of the QW potential, the change in transition frequency and dipole moment are in first approximation:

$$\hbar\Delta\omega_{12}(\mathcal{E}) = 2\frac{(\mu^0\mathcal{E})^2}{\hbar\omega_{12}^0} \tag{4.24}$$

$$\mu(\mathcal{E}) = \mu^0\left(1 - 2\frac{\mu^0\mathcal{E}}{\hbar\omega_{12}^0}\right) \tag{4.25}$$

Here the superscript ^{0} indicates the unperturbed value of frequency and dipole moment, while $\omega_{12}(\mathcal{E})$ and $\mu(\mathcal{E})$ are affected by the external bias.
One would expect that the decrease in dipole moment would lead to a corresponding change in Rabi frequency: however, since the transition frequency is

equally affected, the detuning of the instantaneous IS transition needs to be accounted for. The generalized Rabi frequency Ω_R is:

$$\Omega_R(\mathcal{E}) = \sqrt{(\mu(\mathcal{E}) \cdot \mathcal{E}(t))^2 + (\hbar\Delta\Omega_R(\mathcal{E}))^2} \sim \mu^0(1 + 4(\mu^0\mathcal{E}/\hbar\Omega_R^0)^4)\mathcal{E} \quad (4.26)$$

This simple picture of a static electric field superimposed on the quantum wells potential is not entirely adequate to describe the effect of a time dependent electric field: to fully address that case we need to calculate the full time evolution of the density matrix of the system, treating both nonresonant perturbation and the resonant radiation exciting the IS transition on equal footing.

4.2.3 Model calculations for a two-level system interacting with a nonresonant field

To give a more detailed quantitative analysis of our results we developed a simulation of the interaction of resonant and nonresonant radiation with a two level system. Since the THz pulse is strongly nonresonant to the IS transition, the Rotating Wave Approximation (RWA)does not apply. Due to the time duration of the THz pulse (∼1.5 ps), the semi-impulsive limit also has to be discarded. Finally. describing interaction at higher pulse areas implies that the amplitude of the MIR field is significantly beyond a reasonable description by a perturbative approach.

To gain full insight into the dynamics of the interaction, we need to choose a gauge where the THz and MIR field are treated equally, going beyond the dressed state picture as we previously discussed: we calculate the full time evolution of the system's density matrix in the interaction picture. The Hamiltonian H is the same as Eq.4.16, with an electric field $E = E_{THz} + E_{MIR}$ including the resonant MIR and the nonresonant THz pulse. Both electric fields are described as dampened sinusoidal waves with an appropriate central frequency ν_0 and damping time T:

$$E(t) = E_0 \sin(2\pi\nu_0 t + \phi)e^{-t/T} \quad (4.27)$$

For the THz wave, particular care was taken in choosing the phase ϕ of the sine wave, since out of the semi impulsive limits details of the pulse envelope shape can be expected to influence the interaction.

We calculate the time evolution of the Hamiltonian by solving the Liouville equation with a phenomenological dephasing:

$$\frac{d}{dt}\rho = [H, \rho] - \gamma\rho \quad (4.28)$$

where γ is the dephasing time. The elements density matrix at time t acquire an exponential term $e^{-\gamma t}$ which accounts for the damping, with the transverse damping rate γ_1 applied to diagonal terms and the longitudinal damping rate γ_2 to the non-diagonal terms. In our calculations we use $1/\gamma_1 = 200$ ps and $1/\gamma_2 = 400$ ps.
As we have seen, the induced polarization is calculated as Eq.4.21, $P_E(t) = 2n_e\mu Re(\rho(t)_{1,2})$: the electric field E can be set to be either the THz, MIR pulse, so that the nonlinearly induced polarization is simply:

$$P_{NL}(t,\tau) = P_{THz-MIR}(t,\tau) - P_{THz}(t,\tau) - P_{MIR}(t) \tag{4.29}$$

where τ is the time delay between the THz and MIR pulses.
From the polarization we can retrieve the macroscopic current nonlinearly excited in the sample $j = \partial P/\partial t$, and finally the emitted field $E_{em} = j/(2\epsilon_0 cn)$. Here $n = 2.5$ is the refractive index for MIR radiation. Using the polarization excited by the MIR probe field by itself we are able to retrieve the field emitted by the IS polarization, showing the characteristics Rabi oscillations, while from P_{NL} we calculate E_{NL} emitted from the nonlinear interaction of THz pump and MIR probe fields.
As a last step we can also account for the influence of the current densities in the sample on the local electric field. For a strong radiative coupling regime, the field E_{loc} acting on a quantum wells is strongly affected by the motion of neighboring electrons [189]: if this is the case the current density j needs to be taken into account when calculating the local field acting on a quantum well. The local field is then calculated as:

$$E_{loc}(t) = E_{ext}(t) + \gamma_{rad}\frac{\partial P(t)}{\partial t} \tag{4.30}$$

where the damping rate γ_{rad} will be discussed in Sec.4.5. We are now able to calculate all the relevant quantities we measure in our 2D spectroscopy set up: to gain insight on the effects of the THz interaction we can perform any analysis in parallel on the experimental and simulated data.

4.3 Rabi oscillations in n-doped GaAs QWs

To study intersubband excitations we used 20 layers GaAs quantum wells grown by molecular beam epitaxy at the Paul Drude Institute Berlin. As a substrate we use GaAs, which is a III-V direct gap semiconductor with an energy gap of $E_g = 1.42$ eV at room temperature and $E_g = 1.53$ V at T = 10 K at the Γ point. Near the Γ point, the effective mass of an electron in GaAs conduction

band is $m_{eff} = 0.067m_e$.
The wells have an 11 nm width, separated by 20 nm of $Al_{0.35}Ga_{0.75}As$ as a barrier. The barriers have been δ-doped with Si atoms at a concentration $N = 3 \cdot 10^{17}$ cm^{-3}, resulting in a sheet carrier density $n_e = 5 \cdot 10^{11}$ cm^{-2} in the conduction band for each of the 20 QWs layers. Fig.4.5.(a) shows the quantum wells sample structure.
Fig.4.5.(b) shows a schematic view of the wells: the vertical direction represents energy, and the horizontal is real space in the confinement direction z. At the bottom, the valence band energy structure is shown in black, the blue line at the top shows the conduction band. The energy gap of the AlGaAs barriers is 2 eV at 10 K, larger then that of GaAs: the resulting well depth in the conduction band is 300 meV.

The quantized energy levels in the conduction band are shown in Fig.4.5.(c). The energy levels and wave functions of the intersubband states have been calculated by ($\mathbf{k} \cdot \mathbf{p}$) theory [190]: the 300 meV barrier can support three confined levels. The ground state of the subband lies 30 meV above the bottom of the potential well at T = 10 K. Thanks to the doping, the ground state of the conduction band is already populated and we can study their transition to the higher lying states in the well, with transition frequencies $\nu_{12} = 21$ THz and $\nu_{23} = 27$ THz. The dotted red lines represent $|\psi(z)|^2$, the probability density for an electron position in each level: a high overlap between the wave functions increases the transition probability.
In panel Fig.4.3.(d) the linear absorption spectrum of the $1 \rightarrow 2$ transition measured with an FTIR spectrometer: the $1 \rightarrow 2$ IS transition is centered at 21 THz and has a bandwidth of 1 THz at room temperature.

Prism Geometry

The 20 QWs layers in our sample stack up to a thickness of only 600 nm: they are grown in a GaAs substrate with a total thickness of 350 μm and a 900 μm width. The sample was then polished down to a 45° prism to ensure optimal coupling of the fields to the IS transition dipole moment [191].

The stack lays just 100 nm from the bottom surface of the prism, and the IS transition is coupled to electric fields perpendicular to the base surface (z direction). The prism bottom surface is coated with a thin Gold layer by chemical vapor deposition to achieve optimal coupling of the external field to the QWs IS transition.An electric field E_i, with an in-plane p polarization,and its reflection on the metallic surface $E_r = E_i e^{i\Delta\phi(z)}$ interfere creating a standing wave with the E field along z. The phase is a function of the reflection angle $\gamma = 55°$ as

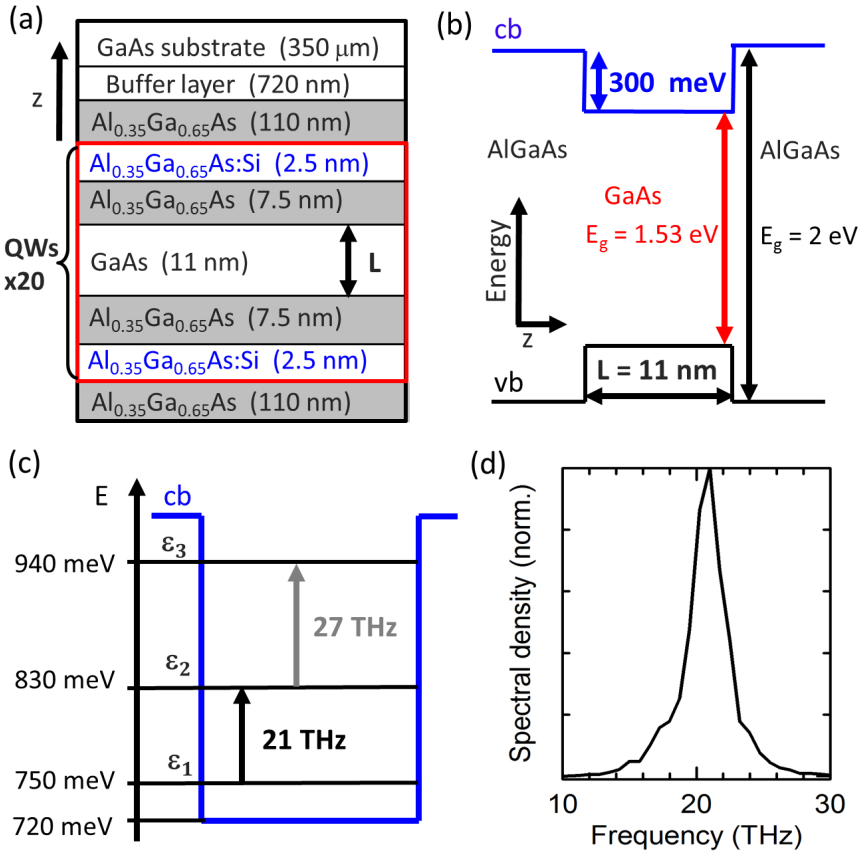

Figure 4.5: (a) Structure of GaAs QWs (b) Energy structure of the valence band (vb) and conduction band (cb, in blue) of the QWs (c) Energy levels in the conduction band: the probability density $|\psi|^2$ of the level wave function is shown as dotted red lines as a function of well depth z (d) Linear absorption spectrum of the sample 1→2 IS transition

$\Delta\phi(z) = 4\pi z\cos(\gamma)/\lambda$. The electric field intensity as a function of z is then

$$I_P(z) = |E_i + E_r|^2 = |E_i|^2 I_0 \left[1 + r_P^2 + 2Re(r_P e^{i\Delta\phi(z)})\right] \qquad (4.31)$$

where the reflection coefficient is $r_p = +1$ for metallic reflections (Fig.4.6.(a)). The p-polarized radiation then has a maximum near the reflection surface where the quantum well layers are placed. Since the QWs layers are considerably thinner than the wavelength of both THz and MIR radiation, all the layers lay close to the maximum field position.

Only half of the prism surface is gold coated: on the other half of the sample, we exploit the properties of internal reflection to suppress the coupling to the IS

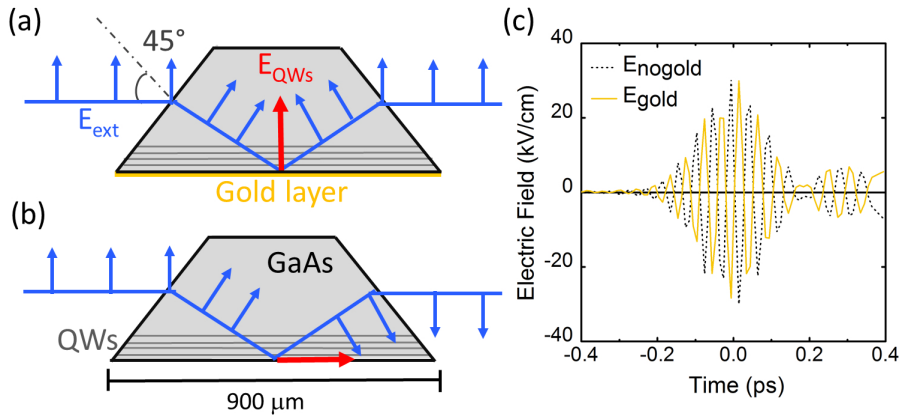

Figure 4.6: Schematic view of the sample geometry used in our setup. The Quantum Wells layers are embedded close to the base of a prism-shaped GaAs substrate. Half of the base surface (a) is covered by a thin gold layer, so that the incident and reflected electric field interfere constructively at the QWs, thus optimizing the coupling with the IS transition. (b) On the uncoated part of the prism, the electric field undergoes total internal reflection at the interface with vacuum: in this case the electric field will be parallel to the QWs plane, destroying the IS coupling.(c) Example of transient electric fields reflected on the gold coated (solid yellow line) and uncoated (dashed black line) parts of the sample.

transition. Indeed, if the bottom surface is uncoated, the field will undergo total internal reflection on the GaAs-vacuum interface (r = -1): in this case however, due to the different boundary conditions, the electric field z-component at the QWs layers is zero, so that coupling to the IS transition is suppressed [192]. The electric field at the QWs is directed in plane (Fig.4.6.(b)), where the their dispersion $E(k_{x,y})$ is flat. Thus, comparing the electric field transmitted from the coated and uncoated halves of the sample allows to isolate the effect of the intersubband transition from any other interaction of the field in the GaAs surface, while at the same time ensuring an optimal coupling to the transition.
Fig.4.6.(c) shows an example of transient electric fields transmitted on the coated (solid yellow line, E_{gold}) and uncoated (dashed black line, E_{nogold}) halves of the sample: they have a π phase mismatch due to different reflection conditions.

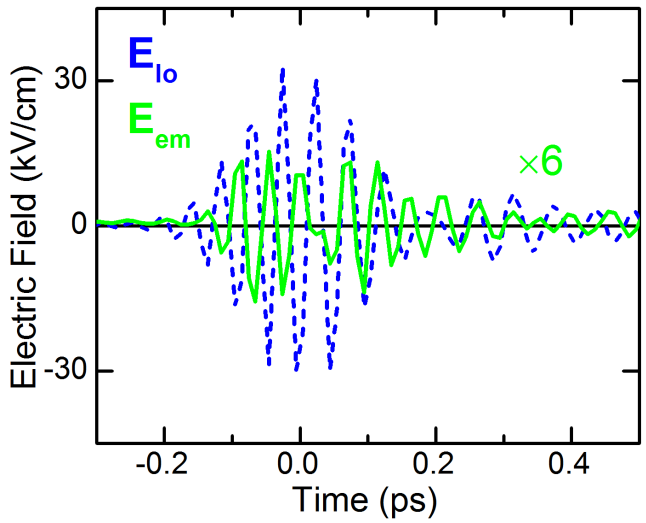

Figure 4.7: Example of a 2π Rabi flop oscillation: the nonlinearly emitted field (solid green line) at first shows an absorptive behavior, 90° out of phase with the local driving field (dashed blue line). After the IS excitation is saturated the emitted field E_{em} is in phase with the driving field, corresponding to an emitting behavior.

Observation of Rabi oscillations

Having measured the MIR infrared field transmitted through the coated and uncoated parts of the sample, the field emitted from the IS transition can be calculated as $E_{em} = E_{nogold} + E_{gold}$. Since the different reflection conditions determine a change of sign for the transmitted electric field, to isolate the contribution from the IS transition the fields have to be added to each other. The local field acting on the quantum wells, enhanced by constructive interference, can be calculated as $E_{loc} = \alpha(E_{gold} - E_{nogold})$. The coefficient α accounts for reflection losses at the prism facets, the projection of the incident field on the z direction and effective interaction length due to oblique incidence. In our sample geometry, $\alpha = 0.43$.

By comparing E_{em} to E_{loc} we can directly observe how Rabi oscillations affect the phase of the emitted field. In Fig.4.7 we show a MIR pulse (dashed blue line) resonant with the IS transition and with a 2π pule area, together with the corresponding emitted field (solid green line). At the beginning of the interaction, the IS transition is absorbing, and the driving and emitted fields are 180° out of phase. As the interaction proceeds, the transition saturates, and the local field starts driving the de-excitation of the IS transition: E_{em} shows a

net emittive character and is in phase with the driving field. This is the typical behavior of a 2π Rabi oscillation, with a Rabi frequency $\nu_R \sim \mu E_{loc} = 4.5$ THz. By performing measurements at different MIR intensities we were able to characterize the field strengths needed to achieve different pulse areas of $1\pi = 50$ kV/cm, $2\pi = 70$ kV/cm,$3\pi = 100$ kV/cm.

4.4 Two-color 2D experiments

After measuring Rabi oscillations by comparing measurements from the coated and uncoated halves of the sample, we set out to perform two color experiments to evaluate the influence of strongly off resonant THz radiation on the nonlinear behavior of the IS transition. Time integrated measurements show a clear signature of THz induced absorption, while time resolved 2D spectroscopy illuminates the effect if the THz field on the phase of the nonlinearly emitted field. All results presented in this section were acquired under cryogenic condition, Helium-cooling the sample to 20 K to reduce thermal noise.

4.4.1 Spectrally integrated experiments: THz induced absorption

At first, the effect of a nonresonant field on the overall mid-infrared transmission through the sample was investigated by THz pump-MIR probe experiments on an MCT detector. For this set of measurements we wanted to keep the interaction in a low intensity regime, to avoid saturating the IS transition. We used a weak MIR pulse (3 kV/cm), with a pulse area much lower than 1π.
The relative change in transmitted amplitude with and without THz field is shown in Fig.4.8 as a function of delay time between the two pulses. Right after the overlap with a strong THz pulse (30 kV/cm) at $\tau = 0$ ps the signal shows a marked transmission decrease. The transmission change $\Delta T/T_0 = (T_{THz} - T_0)/T_0$ is modulated proportionally to the square of the THz field (dashed blue line in the figure): the nonresonant field does not lead to a bleach of the transition through tunneling, but instead drives THz induced absorption.

At later delay time the signal exhibits a step-like increase in transmission: this effect is not related to the IS transition, but rather to electron-hole pair excitation in the GaAs substrate. Even though the THz radiation frequency is far from the transition resonance ($E_g = 1.52$ eV at 20 K), the MIR field drives an interband excitation. Due to the low decoherence rate at cryogenic temperature, electron-hole pairs are created through nonresonant Zener tunneling [25]. At

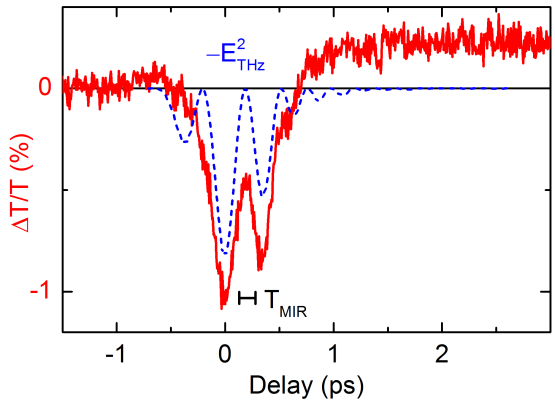

Figure 4.8: Spectrally integrated measurement of the transmitted MIR radiation: change of the transmitted intensity (red solid line) as a function of THz pulse delay. The transmitted intensity is modulated with the same period of the nonresonant THz field (blue dashed line).

room temperature, since the decoherence rate is much higher, the absorptive feature at positive time delays disappears. The step-like signal decay time is of the order on 1 ns, consistent with values for carrier recombination time found in literature [193].

4.4.2 Time-resolved experiments

To gain further insight into the dynamics of nonresonant perturbations on the IS transition we performed time resolved 2D experiments. We measured the transmitted electric field along two temporal axes: the real time t, corresponding to the delay between the EOS probe and the incoming pulses, and the delay time τ between the THz and MIR pulses. Using synchronized choppers we the beams are measured either separately (E_{THz}, E_{MIR}) or together ($E_{THz+MIR}$). To reduce noise, a blank scan is also collected (E_{none}) when both choppers are closed. The nonlinearly emitted signal can then be retrieved as:

$$E_{NL} = E_{THz+MIR} - E_{THz} - E_{MIR} - E_{none} \tag{4.32}$$

A typical measurement of $E_{THz+MIR}$ is shown in Fig.4.9.(a) and (d): the MIR field arrives on the detector at a fixed time (t = 0 was set to the maximum MIR field amplitude) and has vertical phase fronts; the THz field, with diagonal phase fronts, arrives with variable delay ($\tau = 0$ ps at the overlap between the pulses maxima). In the figure, the two rows show measurement at different MIR field strengths: panels (a)-(c) correspond to a low MIR intensity of 3 kV/cm, so that

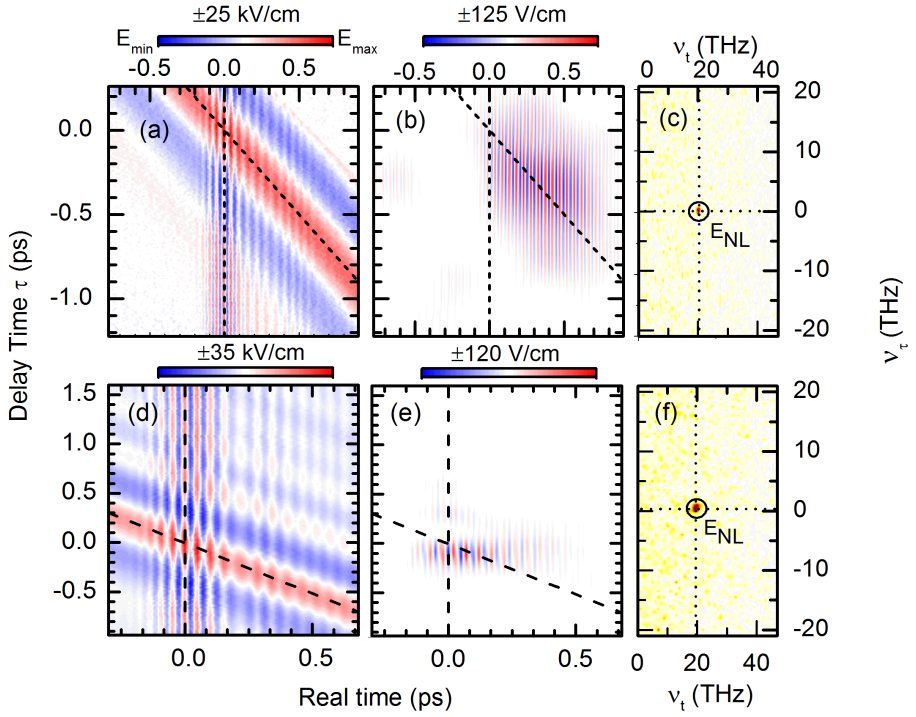

Figure 4.9: (a),(d) 2D spectroscopy transients. The horizontal axis is the real time delay of the probe to the driving fields, while the vertical axis is the delay time between the MIR and THz beam. In the picture, the resonant MIR field has vertical phase fronts, while the nonresonant THz field has diagonal phase fronts and occurs at different delays. (b),(e) Nonlinear signal E_{NL} extracted from the 2D transients. (c),(f) Double Fourier transform of the time dependent nonlinearly emitted field, showing the spectral signature of the nonlinear signal at $\nu_t = 20$ THz and $\nu_\tau = 0$ THz.
The first row (a)-(c) shows result for a low MIR probe intensity of 3 kV/cm, the second row (d)-(f) for a higher field of 30 kV/cm, corresponding to a 2π pulse area.

the IS transition is far from saturation, and panels (d)-(f) to a MIR pulse area of 2π.

By Fourier transforming both time axes, the nonlinear signal can be analyzed in the frequency plane as a function of detection frequency ν_t and excitation frequency ν_τ. In Fig.4.9(c),(f) are shown the nonlinear signal spectra. In both cases only one peak is present, at $\nu_t = 21$ THz and $\nu_\tau = 0$ THz, corresponding to a THz pump-MIR probe pulse sequence.

By applying a 2D gaussian filter around the signal, we can now filter out all

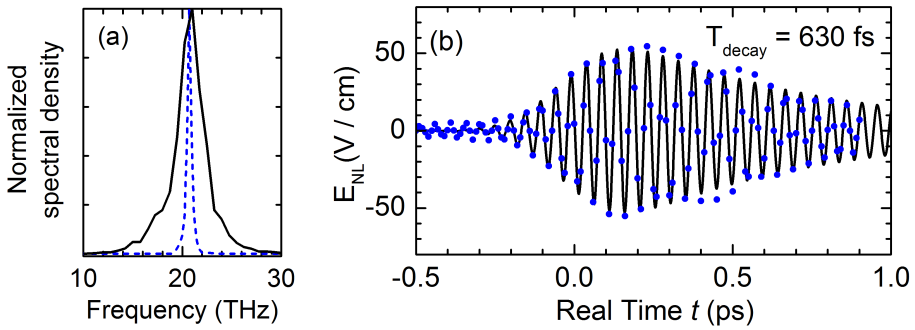

Figure 4.10: (a) Linear absorption spectrum (black solid line) of the IS transition, and Fourier transform of the perturbed free induction decay (dashed blue line) for low MIR amplitude (b) Measured PFID (blue dots), and corresponding fit (black solid line), as used for calculating the polarization decay time.

the noise collected in the 2D matrix for all other frequencies: we then extract even comparatively low signals (120 V/cm in the relevant example) with a high degree of accuracy.
By transforming the nonlinear signal back to the time domain we obtain the plots shown in Fig.4.9.(b),(e). In both panels the dashed lines mark the center of the MIR and THz beams, highlighting how the nonlinearly emitted fields are found either in the overlap between the pulses or in the causal range (top right corner of the panels). Both fields have vertical phase fronts, consistent with $\nu_\tau = 0$ THz.

The low-intensity signal in Fig.4.9.(b) is most prominent for $\tau < 0$ and after the pulse overlap, a time signature consistent with perturbed free induction decay (PFID). Fig.4.10(a) shows the spectrum of the nonlinear signal at $\tau = 0$ (blue dashed line), together with the linear absorption spectrum of the IS transition. The PFID signal is perfectly resonant with the transition, and appears much narrower due to the higher spectral resolution of the measurement. In panel (b) the transient electric field of the PFID signal is plotted as a function of time t. After 1 ps, long after the interaction with the MIR pulse, the IS polarization is still emitting: the total decay time ca be estimated as $T_{decay} = 630$ fs. For a higher MIR intensity the nonlinear signal appears mostly in the overlap region, and as we will see it affects the phase of the Rabi oscillations.

4.5 Discussion

Using the full intensity and phase information contained in the 2D spectroscopy measurements we are now in a position to discuss the effect of nonresonant THz fields on IS transitions. In particular, we will explore its effect on Rabi oscillations, and how a high radiative coupling regime can explain the net increase in absorption from the resonant MIR field.

THz effect on the Rabi oscillations

The Autler-Townes model predicts that, under the effect of a lower-frequency nonresonant field, the emission from an IS transition will show a blue shift and a concomitant phase shift of the emitted field (cfr. Fig.4.2(c)). Through our 2D experiment we are able to investigate how this effect will translate to a nonlinear interaction regime involving Rabi oscillations.

To account for the change in dipole moment and transition energy, the Rabi frequency needs to be rewritten in its generalized form, as in Eq.4.26. That can be rewritten in term of an effective dipole moment as $\hbar\Omega_R = \mu_{eff}(\mathcal{E})\mathcal{E}$ with

$$\mu_{eff}(E) = \mu_0 \left[1 + 4\left(\frac{\mu_0 E}{h\nu_0}\right)^4\right] \tag{4.33}$$

In our experiment we have $\mu_0 = e_0 \cdot 11$ nm, $\nu_0 = 21$ THz and applied electric field amplitude of at most 50 kV/cm. This leads to an estimate value $\frac{\mu_0 E}{h\nu_0} \sim 0.1$ even for the highest field strength employed. The expected change in the Rabi frequency is than less then 10^{-3}.

Indeed we do not observe any significant change in the measured Rabi frequency. In the first row ((a)-(c)) of Fig.4.11 we show the driving field E_{lo}, the emitted field E_{em} resulting from the MIR excitation of the IS transition, and the nonlinearly emitted field E_{NL} in presence of the THz (rescaled for visibility), for different driving field pulse amplitudes. The main effect we detect is not related to emitted field amplitude or to modified Rabi frequency, but to a field dependent variation in transition frequency, best observable by its effect on the emitted field phase.

This effect is apparent in 4.11 second row ((d)-(f)). The phase shift of E_{em} to the driving field E_{lo} (green dashed line) shows the expected switching between net emission and absorption: in the first column, a 1π pulse area leads to IS transition saturation (phase $= +1\pi$), in the second a 2π pulse completes a cycle of absorption and emission (phase $= -1\pi$), and in the third column a 3π pulse shows a second absorptive phase leading again to population inversion. In the same plot we show the change in relative phase brought on by the THz pulse

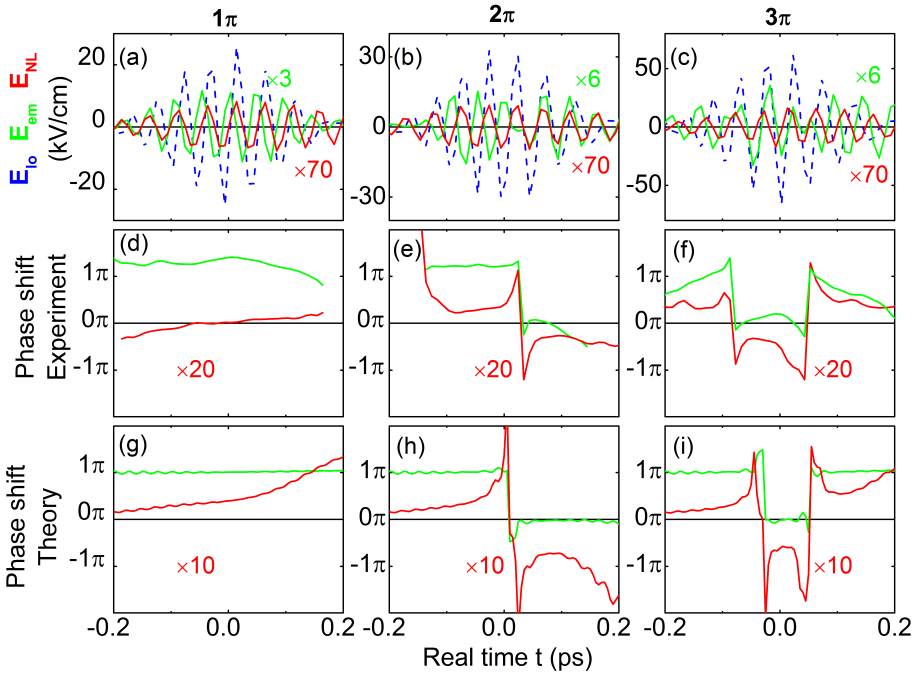

Figure 4.11: Summary on the effect of the nonresonant THz field on the nonlinearly emitted field phase. The leftmost panels show results for a probe pulse area of 1π (20 kV/cm) at $\tau = -0.18$ ps, the center panel of 2π (30kV/cm) at $\tau = -0.09$ ps and the right panel of 3π (50 kV/cm) at $\tau = -0.34$ ps. (a)-(c) MIR probe field $E_{lo}(t)$ (dashed-dotted blue line), field E_e emitted from the IS transition (dashed green line)and THz induced nonlinear signal E_{NL} (solid red line). (d)-(f) Phase shift between the driving field E_{LO} and the emitted electric field E_{em} (dashed green line), showing the phase jumps characteristics of Rabi oscillations, and THz induced change of phase shift (red solid line). (g)-(i) Corresponding calculated phase shifts.

(red solid line). For the 1π panel the change in phase shift rises linearly, as expected from Autler-Townes. For higher pulse areas the effect does not keep building up with each MIR oscillation cycle, because it gets reversed at the switching point, where indeed the change in phase is the highest.
These results are qualitatively retrieved by our calculation with a model two-level system, as show in Fig.4.11((g)-(i)). The calculated phase shift is about twice as large as our measured results: this is due to neglecting higher levels in the Quantum Wells.

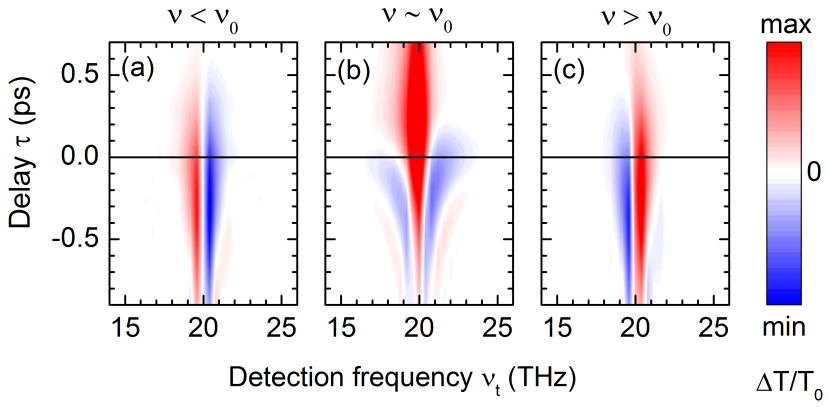

Figure 4.12: Spectrally resolved pump-probe signal for different pump frequencies: (a) pump frequency lower then IS transition frequency, displaying blue-shifted induced absorption; (b) resonant pump field, showing a symmetrical signal with a prominent bleaching at $\nu_t = \nu_0$ for $\tau > 0$; (c) higher frequency pump field, showing a red shifted induced absorption.

Spectrally resolved pump-probe experiments

The THz-induced Stark blue shift perturbs the intensity radiated by the IS transition $|E_{NL}(\nu_t, \tau)|^2$ as a function of frequency and time delay between the pulses. To asses the change in radiated energy due to the THz field, we consider the spectrally resolved pump-probe signal

$$\frac{\Delta T}{T_0} = \frac{E_{NL}(\nu_t, \tau) E^*_{MIR}(\nu_t)}{|E^*_{MIR}(\nu_t)]|^2} \tag{4.34}$$

We use our model 2-level system to predict what would be the spectrally resolved pump-probe for a pump field with different frequencies and a resonant probe of moderate intensity. Fig.4.12.(b) shows that for a resonant pump-probe experiment we would expect a bleaching at the transition frequency $\nu_t = \nu_0 = 21$ THz at positive delay times, with symmetrical induced absorption at $\tau < 0$. For a lower-frequency pump such as our THz beam, the expected blue shift would manifest as a dispersive signal both at positive and negative delays, with a bleaching at lower frequencies and increased absorption for $\nu_t > 21$ THz (Fig.4.12(a)). For a high-frequency pump (Fig.4.12(c)) the model predicts a similar dispersive signature, but with inverted sign, as expected from a red-shifted transition.

Fig.4.13.(a) shows the spectrally resolved pump-probe measured for a 3 kV/cm MIR probe field, low enough to avoid any saturation of the IS transition. The signal exhibits exactly the signature expected from theoretical calculations,

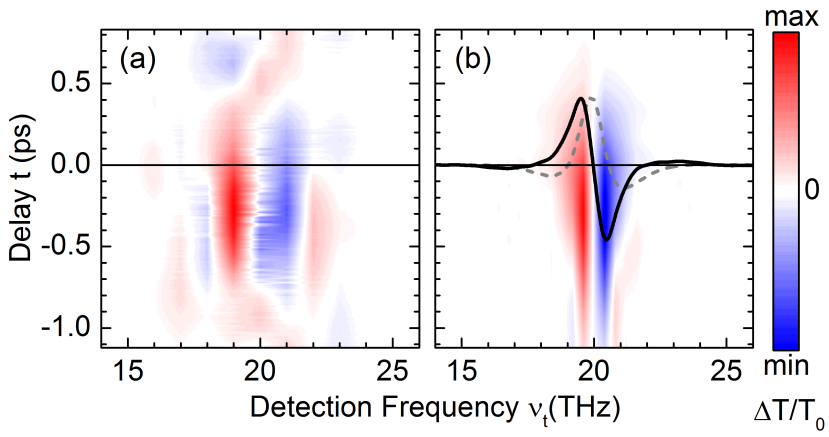

Figure 4.13: (a) Spectrally resolved pump-probe signal for a low MIR probe amplitude (3 kV/cm) as a function of delay time τ and detection frequency ν_t (b) Calculated spectrally resolved pump-probe. At $\tau < 0$ the signal is dispersive (black solid line), while for a fully resonant pump-probe experiment the corresponding signal at $\tau = 0$ (grey dashed line) would be symmetric.

shown in panel (b) for comparison. Note that the amplitude of the dispersive signal (solid black in panel (b) for $\tau = 0$ ps) is not symmetrical in its positive and negative components: while for a resonant pump we would expect a central bleaching with symmetrical absorption wings (dashed gray line), the instantaneous absorptive component in our experiment appears larger than the low frequency bleaching for $\tau > 0$. At negative delay time, on the other hand, the dispersive signal is symmetrical, and does not modify the net energy balance of the system. Indeed, in our time resolved absorption measurement (Fig.4.8) we only see THz induced absorption becoming relevant at the overlap and after, for $\tau > 0$.

The pump-probe signal shows some interesting features also for higher pulse areas: in Fig.4.14(a)-(b) are shown respectively the experimental and calculated results for a probe pulse area of 2π (30 kV/cm). While the THz field is present, the MIR radiation goes through rapid cycles of reduced and absorption both above and below 21 THz. In panel (c) we plot a cut of the experimental signal at $\nu_t = 20$ THz as a function of τ (solid red line), together with the intensity of the THz field (dashed black line). The peaks of induced absorption correspond to the antinodes of the THz field, clearly marking this effect as a result of non-resonant THz interaction, even though for higher pulse areas the THz does not lead to an overall change in absorbed MIR intensity.

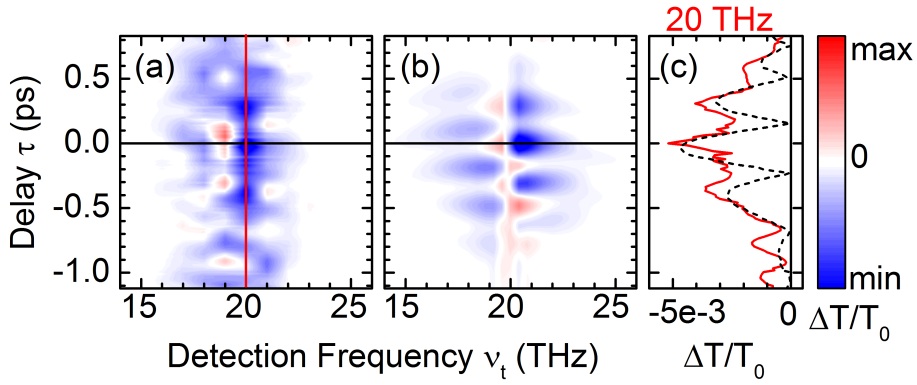

Figure 4.14: (a) Spectrally resolved pump-probe for a high MIR probe (30 kV/cm, 2π pulse area) and (b) corresponding calculated signal. (c) Cut of the measured signal at $\nu_t = 20$ THz (solid red line), showing the same oscillation period as the THz field intensity (dashed black line)

The effect of radiative coupling

As a final step, to explain the induced absorption measured in spectrally integrated experiments (cfr. Section 4.4.1) we need to take into account radiative damping. The energy irreversibly absorbed by the sample $W_{abs}(t)$ can be calculated by time integrating the instantaneously absorbed energy $I_{abs}(t)$ [189]:

$$W_{abs}(t) = \int_{-\infty}^{t} I_{abs}(s)ds \tag{4.35}$$

$$I_{abs}(t) = -\alpha^{-1}\epsilon_0 c E_{em}(t)E_{loc}(t) \tag{4.36}$$

here $\alpha = 0.43$ connects the local field to the transmitted field we can measure. The energy irreversibly absorbed by the sample is then $W_{abs}(\infty)$, which still has not been re-emitted after all radiative processes are over. In Eq.4.36 we can see that the instantaneously absorbed energy depends on the instantaneous local field in the sample, which in a strong radiative coupling regime is influenced as much by the field re-emitted by the QWs polarization then by the applied external field.

$$E_{loc}(t) = E_{tr}(t) = E_{ext}(t) + E_{em}(t) \tag{4.37}$$

To test whether we are in a strong radiative damping regime we can estimate the radiative damping rate and compare it with the total decay rate of the polarization, measured from the PFID signal (Fig.4.10.(b)) as γ_{tot} =(0.63 ps)$^{-1}$. We calculate the radiative damping rate from the equation of motion for the coherence ρ_{12}, derived by solving the Bloch equations Eq.4.18 and Eq.4.19 [194].

We rewrite the equation of motion of the polarization using the abbreviation $\gamma_1 = \mu/\hbar$ and $\gamma_2 = \frac{N_D \mu^2}{\hbar \epsilon_0 c}$:

$$\frac{d^2x}{dt^2} = -\left(2\gamma_{tot} + \omega_{12}\gamma_2(1-2\rho_{22})\right)\frac{dx}{dt} + \left(\gamma_{tot}^2 - \omega_{12}^2\right)x + \omega_{12}\gamma_1 E_{in}(1-2\rho_{22}) \tag{4.38}$$

where we called $\mathrm{Re}(\rho_{12}) = x$. Noting that γ_2 is an adimensional quantity, the radiative damping term can then be recognized as:

$$\frac{1}{2}\omega_{12}\gamma_1 = \frac{\omega_{12} n_e \mu^2}{2\hbar\epsilon_0 c} \tag{4.39}$$

This expression is correct for a pass through a single quantum well layer. To account for the prism reflection geometry the radiative damping rate has to be modified as such:

$$\gamma_{rad} = \frac{\omega_{12} N_e \mu^2 \sin(\theta)\tan\theta}{\hbar\epsilon_0 c n_{sub}} \tag{4.40}$$

Here $N_e = n_e N_{layers}$ is the total sheet electron density in all 20 quantum wells layers and n_{sub} is GaAs refractive index. The angular terms account for the oblique propagation direction in the sample, which affects the interaction area and for the field projection on the z direction. Using this expression we estimate $\gamma_{rad} = (0.9\ \mathrm{ps})^{-1}$, which accounts for most of the total damping: this confirms that in this geometry we are indeed in a strong radiative coupling regime.

To see how this affect THz induced absorption, we performed simulations at both low and high radiative damping rates. Let us discuss the high radiative coupling regime first.

In Fig.4.15 the local field acting on the QWs IS polarization is shown in panel (a) in a dotted black line: at first $E_{loc}(t)$ is mainly determined by the weak external MIR field, but as the Emitted field E_{em}^0 (dashed blue line) grows stronger it becomes the most prominent contribution to the local field.

In panel (b) the corresponding instantaneously absorbed energy is plotted (dashed blue line): in the first part of the interaction the system stores a large amount of energy, which is however for the most part radiatively emitted later on, as the local field becomes dominated by the quantum wells emission. As such, the energy stored in the sample (panel (c), dashed blue line) increases during the MIR pulse and then drops again to zero after the pulse, while the quantum wells polarization is emitting radiatively.

The presence of the THz field affects both the local and emitted field, strongly affecting the absorbed energy. To illustrate its effect we consider a gaussian half cycle pulse $E_{THz}(t)$ (dashed red line, panel (a)) interacting with the sample together with the MIR pulse at $\tau = 0$. As we have seen, due to the THz pulse $E_{em}(t)$ (solid red line) is blue-shifted compared to E_{em}^0, thus reducing its

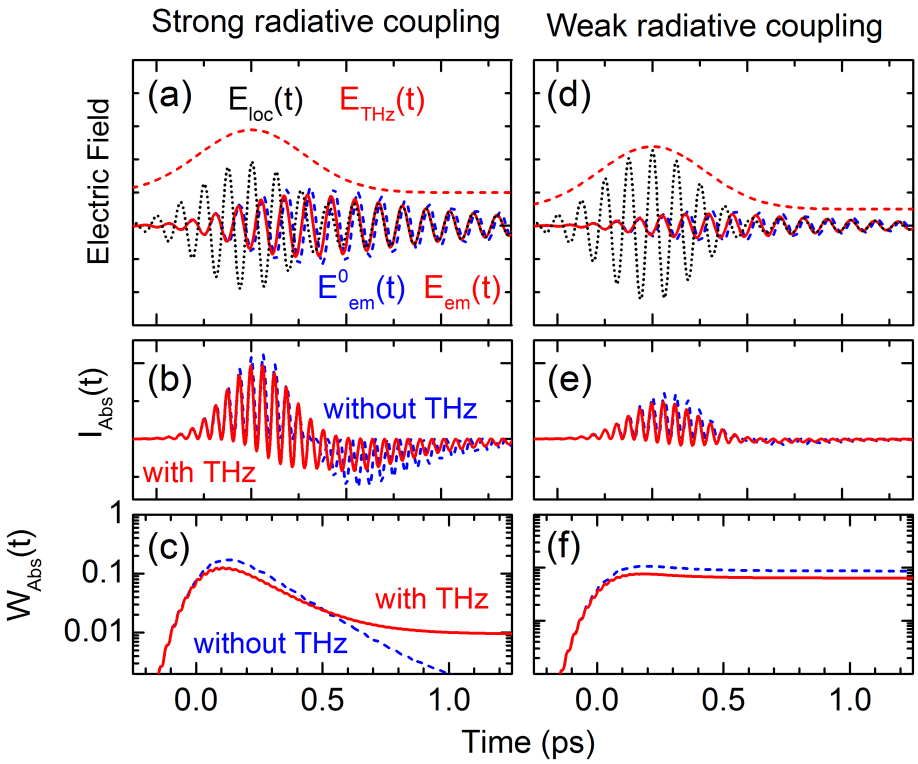

Figure 4.15: The first column shows results in the case of strong radiative coupling, the second column for weak radiative coupling.
(a),(d) A resonant driving field E_{loc} (dotted black line) excites an IS transition emitting the E^0_{em} (dashed blue line). A nonresonant THz field (dashed red line) leads to a different emitted field E_{em} (solid red line). (b),(e) Instantaneous energy absorption in the sample, with (solid red line) and without (dashed blue line) the THz field. (c),(f) Energy deposited in the sample as a function of time. In a strong radiative coupling regime the THz field results in a higher irreversibly absorbed energy.

effectiveness in exchanging energy with the IS polarization: after the MIR pulse net energy emission is suppressed. We can see in Fig.4.15.(b) that when the THz is present the instantaneous energy absorption (red solid line) is at first mostly unaffected as the phase shift is building up, but in contrast the energy re-emitted later is strongly reduced: this increases the net energy transfer to the sample (panel (c), solid red line), even if the THz pulse is not directly exchanging energy with the IS polarization.
If on the other hand the system were in a regime of weak radiative coupling, we could not explain the net change in MIR transmission: in Fig.4.15.(d)-(e) we

can see that, since now $E_{loc}(t)$ does not extend after the end of the MIR pulse, light emission from the IS polarization is strongly suppressed after the interaction with the pulse, and the THz-induced blue shift has almost no influence on energy absorption. The total absorbed energy (panel (f)) is higher overall, since less light is being re-emitted, but its not enhanced by THz radiation. On the contrary, since the THz slightly reduces direct absorption through the reduced overlap between the states wave functions, the net THz effect in a regime of weak radiative coupling is a slight bleaching of the transition. Since our system is indeed in a strong radiative coupling regime, we can explain the net MIR light absorption measured in Fig.4.8.

4.6 Conclusion and outlook: coherent control of IS emission

In this chapter we studied the interplay of resonant and nonresonant interaction of ultrashort electric fields with GaAs QWs. First we measured Rabi oscillations of the population excited by 21 THz MIR pulses resonant to the first IS transition, exploiting our sample prism geometry and the different interference conditions due to metallic and total internal reflection to isolate both the local driving field and the radiation emitted by the quantum wells themselves.
By adding a nonresonant THz pulse we retrieved a blue shift in the the IS transition frequency, as expected from the Autler-Townes model, which manifested itself in a phase shift of the nonlinearly emitted field. This phase shift is most intense at the switching point of Rabi oscillations. Even though the THz field induces a decrease of the transition dipole moment by tilting the well potential, we found that the Rabi frequency is not reduced by the presence of the THz field, since the change in dipole moment is compensated by the transition blue shift.
Due to strong radiative coupling in the highly doped QWs, the local field driving the excitation is dominated by the field radiated by neighboring quantum-wells. In this regime, after excitation by a short MIR pulse, the re-emitted field keeps driving the IS transition after the MIR pulse has gone. In presence of the THz field, the induced blue shift causes a detuning which hampers coherent light re-emission: overall, the energy stored in the sample after the end of radiative interaction is increased. In this sense, not only the reduction of dipole moment does not inhibit MIR absorption, but the THz field results in enhanced absorption. Though re-emission is prevented by the interaction of the THz field, the stored energy comes entirely from resonant MIR radiation, without any direct

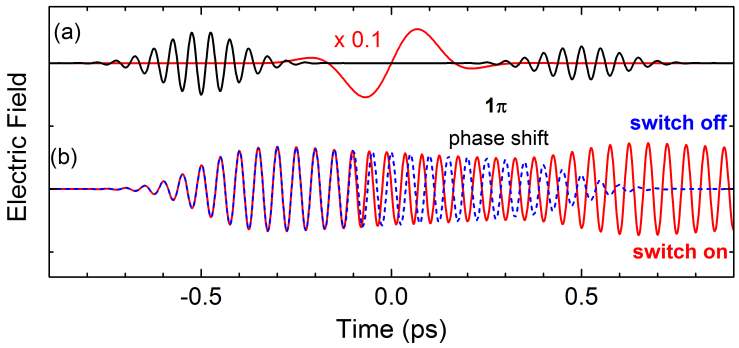

Figure 4.16: A high enough nonresonant THz field can act as an all-optical switch of an IS emitter: (a) Two mid-infrared fields resonant with an IS transition (black line) and a strong nonresonant THz field (red line). (b) The emitted field (dashed blue line) generated by the first MIR pulse is switched off by the second MIR pulse. The field emitted in the presence of the THz field (solid red line) builds up a significant phase shift between the two mid-infrared pulses, so that the second one enhances the emission instead of switching it off.

energy transfer from the nonresonant THz beam.

The THz-induced phase shift of the IS emission builds up over the course of the THz pulse interaction: with a strong enough nonresonant pulse it could be possible to use it to control the phase of the emitted field, switching from emittive to absorptive behavior. In Fig.4.16 a possible switching system is presented: the solid black lines in (a) represent two MIR pulses resonant with an IS transition. The emission driven by the two pulses is shown in (b) by the blue dashed line: the timing between the two pumps in our calculation has been chosen so that the second interaction switches off the IS emission.
We can now calculate the effect of a very strong low frequency pulse (red line in Fig.4.16.(a)) which builds up a phase shift in the nonlinear interaction in the interval between the MIR pulses: if by the time the second pulses reaches the sample the emitted field has built up a 1π phase shift (solid red line in Fig.4.16.(b)), the MIR pump will not turn off the emission, but instead restore it to its maximum amplitude.
This simple scheme shows that it is feasible to use a nonresonant pulse as a switch of the MIR emission. No direct exchange of energy between the IS polarization and the THz pulse is necessary, so the switching process is entirely lossless: since the THz pulse is unchanged by the interaction, it could be recycled and utilized in a subsequent cycle, making this scheme attractive for optoelectronic switching applications.

Chapter 5

Two-dimensional THz spectroscopy of crystalline Aspirin

The long wavelength of THz radiation makes it particularly well suited to study collective phenomena involving a large number of oscillators. Materials like molecular crystals, which can exhibit intricate dipole-dipole interactions between their closely-packed components, are a particularly interesting system to study in this frequency range. The strong coupling of dipoles through the local field resembles the description of soft modes in ferroelectrics, polar lattice vibrations whose frequency lowers when approaching a phase transition, as their vibrational dipole strength is enhanced by contributions from the neighboring electronic dipoles.

Such interactions can easily become the most prominent component of the local electric field, resulting in nonlinear effects largely controlled by the induced macroscopic polarization in the material. The nonlinearity of local field effects has been explored for excitons in semiconductors [133, 150, 195], while among ferroelectrics only the nonlinear response of strontium titanate thin films has been explored [196, 197]. To study the nonlinear response of a soft mode, we will use a molecular crystal as a model system, and apply 2D THz time domain spectroscopy to gain insight in the dynamics of the interaction. The aspirin crystal, which displays a highly collective hybrid electronic-vibronic oscillation at 1.1 THz, is the ideal system to analyze.

In this chapter we will first discuss the structure of aspirin in its crystalline form, which can not be correctly predicted without accounting for the influence of its

low frequency hybrid rotational-electronic mode. The next section will describe Cochran theory of soft modes in displacive ferroelectrics, and how a similar phenomenon can appear in molecular crystals, where a strong Lorentz field provides strong coupling between electronic and nuclear motions. The effect of dipole-dipole coupling on the predicted nonlinear response will be discussed, based on theoretical and computational models, identifying a soft mode blue shift as the main nonlinear response of such a system. Finally the predictions of our models will be compared with the results of 2D THz spectroscopy experiment we performed on aspirin powder tablets, showing multiple signatures of the expected nonlinear blue shift.

5.1 Crystalline aspirin

The physical and chemical properties of the aspirin molecule have been widely studied thanks to its utmost importance to the pharmaceutic industry. The next section will give a brief overview of the structure of aspirin in its crystalline form, the controversy surrounding the existence of aspirin polymorphs, and finally discuss how the preferred aspirin structure relates to its optical properties in the THz region.

Crystal structure

Acetylsalicylic acid ($C_9H_8O_4$) is composed of a benzene ring connected to two functional groups: on one side a carboxyl group, from salicylic acid, and on the other two oxygens and a methyl group from acetic anhydride (Fig.5.1.(a)). Since the exact form of active pharmaceutical ingredients can affect their solubility, bioavailability and formulation [198, 199], the structure of aspirin in crystalline form has been widely studied.

The first report of a structure from X-ray diffraction dates back to *Wheatley et al.* [201], describing a monoclinic crystal ($P2_1/c$ space group) structure with 4 molecules in the unit cell. Their result were later revised to improve the calculation of solubility and elastic constants, resulting in the currently accepted

Lattice Constants			**Angle**	**Volume**
a	b	c	β	V
11.430 Å	6.591 Å	11.394 Å	95.68°	854.23 Å^3

Table 5.1: Aspirin form I unit cell dimensions [200]

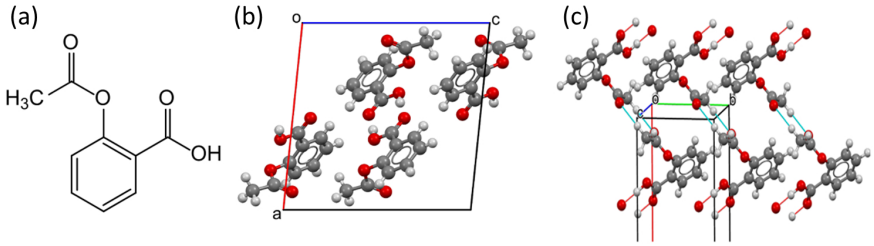

Figure 5.1: (a) Aspirin molecular structure (b) Unit cell of the Aspirin crystal, containing four molecules. Carbon atoms are shown in grey, oxygens in red and hydrogens in white (c)Three dimensional view of the crystal structure, highlighting the interlayer hydrogen bonds in light blue (crystal structure from [202])

structural description by *Kim et al.* [200]. The unit cell parameters are summarized in Tab.5.1.
The crystal structure is represented in 3D in Fig.5.1.(b)-(c), with the panels showing respectively a top view and a front view of the unit cell. Within a crystal plane, hydrogen-bonded cyclic dimers of carboxylic acid form between pairs of aspirin molecules (blue circle in panel (b)). The light blue lines in panel (c) mark the hydrogen bonds connecting hydrogen atoms in a methyl group to an oxygen atom of an acetic group in a different molecular plane. These weak hydrogen bonds allow for high plasmon-phonon coupling between the methyl groups and the electrons in the benzene rings [202]: they will prove crucial for the THz range absorption of aspirin, solving a long standing controversy on the natural abundance of aspirin polymorphs.

Polymorphism

Aspirin molecules crystallize spontaneously in the structure we have just described, typically called form I. A second metastable structure (form II) has appeared in various report since the Sixties [203, 204], and was predicted by molecular dynamics computation [205, 206]: the expected polymorph was described with a very similar structure to the common form I, differing mainly for a small displacement between alternate crystal planes.

Experimental characterization of form II however proved to be elusive: a first claim [204] was heavily disputed [207] due to the difficulty of isolating purely form II crystals (with ABAB stacking) from the more easily synthesized form

I (AAAA stacking). The second form has since been more clearly identified, and a few methods of form II synthesis have been developed [208, 209]. Aspirin form II, even when it can be isolated, remains unstable and fragile:pressure or temperature changes, and mechanical stress cause the crystal planes slide on each other, returning to the form I stacking configuration [210].
The rarity and instability of aspirin form II are somewhat surprising in light of its almost degenerate lattice energy, which would lead to a similar natural occurrence of the two structures: careful molecular dynamics calculations from the group of Alexander Tkatchenko, including many-body van der Waals interaction and zero-point energy contributions, predict a lattice energy difference of 0.35 kJ/mol [202].
Their analysis of many-body interactions at low frequencies can offer an explanation: the phonon density of states of form I has a peak at 33 cm^{-1} = 1 THz which is lacking in form II. This phonon corresponds to a concerted motion of different methyl groups in the unit cell shown in Fig.5.2.(b), coupled to electronic oscillations in the benzene rings. Due to its highly collective character, the mode only appears in molecular calculations considering the full many-body interaction dynamics, while it is absent in models including only pair-wise interaction.
Conversely in form II interplanar hydrogen bonds form a different pattern, with an asymmetric separation between methyl groups on adjacent molecules, which prevents the plasmon-phonon coupling responsible for the low frequency hybrid mode of form I. The thermal population of excited phonon states raises the entropy of form I, leading to a lower free energy and explaining its natural abundance.

Linear absorption spectrum

The rotational motion of aspirin methyl groups, shown in Fig.5.2.(b) has been observed by neutron diffraction [211] and has been reported in THz absorption spectroscopy at cryogenic temperatures. An absorption at 1.1 THz is observed in measurements at 4 K [212] and even more clearly at 77 K using aspirin tablets as a sample [213]. Some room-temperature measurement have been reported in the framework of chemicals and drug recognition [214], but they do not resolve the 1.1 THz hybrid mode.

Before proceeding to 2D THz spectroscopy we wished to observe the hybrid mode absorption in our samples, tablets of pressed aspirin powder. To measure a linear absorption spectrum at high resolution we used a commercial THz spectrometer (*Menlo System's TERA K15*). It uses a femtosecond fiber laser,

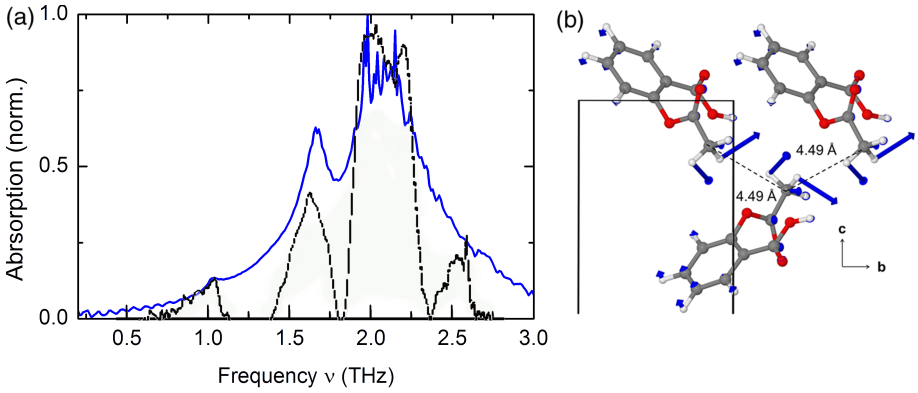

Figure 5.2: Room temperature absorption spectrum of a pressed aspirin powder tablet (solid blue line), showing the weak absorption from the 1.1 THz hybrid mode. The black line show an aspirin tablet spectrum from literature, collected at 77 K by Grischkowski and collaborators [213] (in arbitrary units) (b) Methyl groups motion associated with the 1.1 THz mode, which is coupled to electronic oscillations in the benzene rings (from [202])

fiber-coupled to photoconductive antennas used as a THz source and detector, the output beam is centered at 0.5 THz with an overall bandwidth of ∼3.5 THz. Compared to our 2D set-up it offers a longer available scan length, which in an EOS detection scheme is limited by reflections in the detection crystal, resulting in a frequency resolution of 1 GHz. The transmission spectrum was measured in a clean Nitrogen atmosphere to avoid water vapor absorption, focusing the TERA K15 beam with a polymer lens onto a 1.5 mm thick pure aspirin tablet. The measurement was carried out at room temperature; cryogenic spectra collected in the EOS set-up present similar features but have poorer resolution.
Our linear absorption spectrum is shown in blue in Fig.5.2.(a): the 1.1 THz mode appears as a small shoulder on top of a larger peak at 1.6 THz. To show consistency with previous results, the same graph shows also the aspirin tablet spectrum at 77 K reported by Grischkowsky and coworkers in Ref.[213] (black dashed line).
From the absorption line we can give a rough estimate of the transition dipole moment when interacting with a weak electric field: the absorption coefficient is $\alpha = 2.3$ cm^{-1} while the linewidth gives a dephasing time $\tau = 3.1$ ps. The dipole moment can be calculated as [215]:

$$\mu = \sqrt{\frac{\hbar\epsilon_0 c\alpha}{\omega n\tau}} = 160 \text{ fm} \cdot e \tag{5.1}$$

where $n = 4/V$ is the density of oscillators. The coupling to the external electric

field is quite weak, but as we will show in the next section it can be significantly enhanced in presence of a strong local field.

5.2 Soft modes in molecular crystals

Soft modes are phonons whose frequency tends to zero as a structural phase transition is approached, typically in ferroelectric materials nearing the Curie temperature T_C. After the first observation by Raman [216] in quartz, they have been studied in a wide range of ferroelectrics: typical materials are in the perovskite group - e.g. $BaTiO_3$, $KNbO_3$, $PbTiO_3$, etc. - or closely related substances like $LiNbO_3$, and hydrogen-bonded ferroelectrics like those in the KDP family.

Copious experimental work has been carried out on ferroelectric soft modes, via IR and Raman spectroscopy, neutron scattering and X-Ray diffraction among others [217]. Theoretical work (Cochran [218], Cowley [219]) has focused on understanding the mechanism for the structural transition. A displacive transition involves a potential energy surface shifting to a different minimum with temperature, which is the preferred model for the perovskites class of ferroelectrics, while an order-disorder transition, which a jump to a different minimum among many, represent a different physical class of materials. The displacive transition is driven by the instability of the soft mode phonon, while an order-disorder transition happens through collective tunneling: soft modes then seem to appear naturally in displacive transition, but not in the order-disorder type, with time resolved Raman scattering having been used to explore this issue [220]. The dynamics of the nonlinear response of soft modes has remained largely unexplored: previous work on $SrTiO_3$ thin films [196] reports a hardening of the mode due local polarization near the thin film defects.

In this section Cochran's theory of ferroelectricity will be described, highlighting how the soft mode instability at low frequencies is related to a large coupling between ionic and electronic motions: the coupling enhances the phonon oscillator strength as the crystal approaches its phase transition. This so called polarization catastrophe stems from a preponderant effect of the local field corrections, described by the Clausius-Mossotti relation. A similar coupling through an enhancement of the local field can be found also in molecular crystals, making them a good model system to study the nonlinear response of a soft mode.

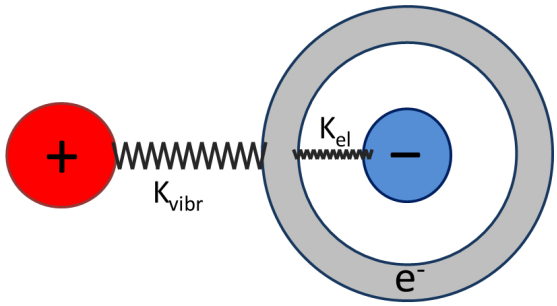

Figure 5.3: Ionic crystal structure in the Cochran theory of ferroelectricity: the negative ion (blue) is polarizable and connected to its external electron shell (grey) by a force constant k_{el}, and to the positive ion (red) by a restoring force K_{vibr}

Cochran theory of soft modes

Cochran's theory of ferroelectric transitions [218], which spurred widespread interest in the subject after its proposal in 1960, treats a displacive phase transition as a problem of dynamical lattice stability. The theory considers a ionic crystal with a simple cubic structure (CsCl or NaCl type) and it sets out to establish dynamical stability conditions under small deformations of its lattice. The crystal model consists of three elements shown in Fig.5.3.(a): the positive and negative ionic cores, shown as a red and a blue sphere, and an electron cloud, shown in grey. Each element form its own Bravais lattice, connected to the others by restoring elastic forces. Only the negative ion is assumed to be polarizable, for simplicity, and it is connected to its outer electronic shell by a force constant k_{el}. The ionic cores are coupled together through an elastic force constant K_{vibr}.

Cochran writes the classical equations of motion for the positive ion, negative ions and electronic shells lattices, calling their displacement from equilibrium position respectively u_1, u_2, v_2, and their charges Z, X, Y (with $X+Y+Z=0$ to ensure overall charge neutrality):

$$m_1\ddot{u}_1 = K_{vibr}(v_2 - u_1) + \frac{p}{3\epsilon_0}Ze \tag{5.2}$$

$$m_2\ddot{u}_2 = k_{el}(v_2 - u_w) + \frac{p}{3\epsilon_0}Xe \tag{5.3}$$

$$0 = K_{vibr}(u_1 - v) + k_{el}(u_2 - v_2) + \frac{p}{3\epsilon_0}Ye \tag{5.4}$$

Here m_1, m_2 are the ions' masses and $p = Pe^{\imath\omega t}$ is the polarization. Now, by assuming an harmonic behavior of the displacement, i.e. $u = Ue^{\imath\omega t}$, the

equations can be rewritten as:

$$m_1\omega^2 U_1 = K'(U_1 - U_2) - \frac{iP}{3\epsilon_0}Z'e \tag{5.5}$$

$$m_1\omega^2 U_2 = K'(U_2 - U_1) + \frac{P}{3\epsilon_0}Z'e \tag{5.6}$$

where $K' = k_{el}K_{vibr}/(k_{el} + K_{vibr})$ and $Z' = Z + Yk_{el}/(k_{el} + K_{vibr})$ and V is the unit cell volume. The polarization definition $P = e/V(ZU_1 + Xu_2 + YV_2)$ can been used to rewrite the third equation as:

$$P\left(1 - \left[\frac{(Ye)^2}{3\epsilon_0 V(k_{el} + K_{vibr})}\right]\right) = \frac{Z'e}{V}(U_1 - U_2) \tag{5.7}$$

Now we consider the effect of an external electric field of amplitude E_0 and frequency high enough to only move the electronic shell. The shell equilibrium is fixed by:

$$E_0 Y = (k_{el} + K_{vibr})V_2 \tag{5.8}$$

and the polarization is:

$$P = \frac{eYV_2}{V} \tag{5.9}$$

The electronic polarizability $\alpha = pV/E_0$ is then:

$$\alpha = \frac{(Ye)^2}{k_{el} + K_{vibr}} = \frac{3V}{4\pi}\frac{\epsilon_\infty - 1}{\epsilon_\infty + 2} \tag{5.10}$$

where the Clausius-Mossotti expression [221] connects the polarizability to the high frequency dielectric constant ϵ_∞. The polarization can then be rewritten as:

$$p = \frac{Z'e(\epsilon_\infty + 2)(U_1 - U_2)}{3V} \tag{5.11}$$

This expression can finally substituted in the coupled equations 5.5-5.6, retrieving the frequency of the lowest transverse phonon:

$$m'\omega_T^2 = K' - \frac{(\epsilon_\infty + 2)(Z'e)^2}{9\epsilon_0 V} \tag{5.12}$$

where m' is the reduced mass of the ions. Now, the condition for lattice stability of a cubic crystal is that the frequencies of its normal modes are strictly positive. When $\omega_T \to 0$, the crystal restoring forces become weak, and it can lead to a ferroelectric phase transition.

The electronic shell motion is related to the ionic displacement:

$$V_2 - U_2 = \frac{K' + Z/Y\alpha/3\epsilon_0 V}{1 - \alpha 3\epsilon_0 V}(U_1 - U_2) \tag{5.13}$$

Here the fraction denominator diverges for $\alpha/3\epsilon_0 V \to 1$: for a large polarizability, the electronic motion contributes disproportionately to the soft mode

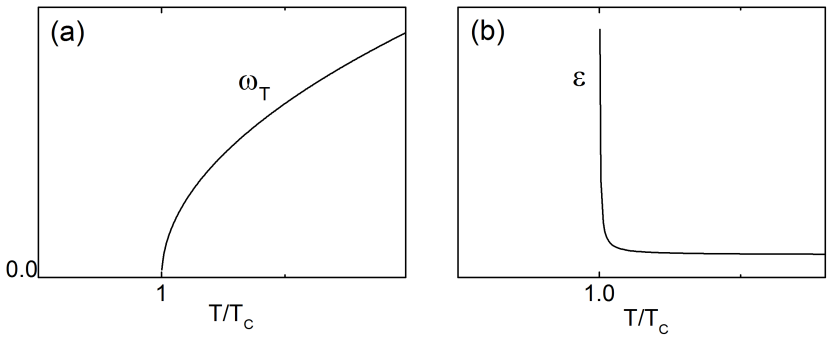

Figure 5.4: Behavior of the soft mode frequency (a) and of the dielectric constant (b) as a function of temperature near the polarization catastrophe

dipole compared to the ionic displacement, as observed in X-Ray diffraction on KDP [222]. To calculate the frequency of the lowest longitudinal mode, the local Lorentz field has to be included: the local field $E_{loc} = P/3\epsilon_0$ stems from the average field of all neighboring dipoles in a solid [223]. The longitudinal mode is then:

$$m'\omega_L^2 = K' + \frac{2(\epsilon_\infty + 2)(Z'e)^2}{9\epsilon_0\epsilon_\infty V} \tag{5.14}$$

The static dielectric constant can be then derived through the Lyddane-Sachs-Teller relation [224] $\epsilon(0)/\epsilon_\infty = (\omega_L/\omega_T)^2$. The static dielectric function diverges when $K' \to \frac{(\epsilon_\infty+2)(Z'e)^2}{9\epsilon_0 V}$: certain conditions for the short range forces described by K' can lead to an exploding dielectric function.

In a ionic crystal, lattice vibration anharmonicity results in a linear dependence of the force constants on temperature, as is the unit cell volume. The temperature dependence of the soft mode then becomes:

$$\mu\omega_T^2 = K'\gamma(T - T_C) \tag{5.15}$$

The dielectric constant follows the Curie-Weiss law:

$$\epsilon(0) = \epsilon_\infty + \frac{C}{T - T_C} \tag{5.16}$$

$$C = \frac{(\epsilon_\infty + 2)^2(Z'e)^2}{9\epsilon_0 K'\gamma} \tag{5.17}$$

Near the critical temperature the soft mode frequency gets lower and lower approaching the critical temperature, the dielectric constant diverges, and so does the polarizability (Fig.5.4). As the restoring forces soften and the long range interaction become predominant, the crystal approaches the polarization catastrophe: now we will show how a similar situation can arise in a molecular crystal, when strong local field correction lend the large dipole strength of electronic oscillators to low frequency ionic motions.

Local field corrections in molecular crystals

We consider a dense medium as an array of n interacting dipoles μ interacting with an external field E_{ext}: the local field experienced by each atom is made up of E_{ext}, the emission from the polarized dipoles, and the delta spikes at each dipole position $\frac{p}{3\epsilon_0}\delta(r)$. The local Lorentz field is the spatial average of these contribution. The dipoles however do not feel any effect from the delta spikes on the dipole them selves, which averages out to $P/3\epsilon_0$ where $P = np$ is the macroscopic polarization [225]. The local field can then be calculated simply as the average electric field, minus the delta contribution:

$$E_{loc} = E_{ext} + \frac{P}{3\epsilon_0} \tag{5.18}$$

so that the polarization and the linear susceptibility $\chi^{(1)}$ read:

$$P = n\alpha E_{loc} = n\alpha(E_{ext} + \frac{P}{3\epsilon_0}) \tag{5.19}$$

$$\chi^{(1)} = \frac{n\alpha}{1 - \frac{n\alpha}{3\epsilon_0}} = n\alpha\left(\frac{\epsilon/\epsilon_0 + 2}{3}\right) \tag{5.20}$$

In the last passage the Clausius-Mossotti relation was employed to introduce the dielectric function ϵ. The local field corrections result in a higher linear susceptibility.

We can now assess the effect of local field corrections on the nonlinear polarization contribution [223]. Dividing the polarization in its linear and nonlinear components as $P = P^L + P^{NL}$, the previous expression becomes:

$$P^L = n\alpha\left(E + \frac{P^L}{3\epsilon_0} + \frac{P^{NL}}{3\epsilon_0}\right) = \epsilon_0(\epsilon/\epsilon_0 - 1)\left(E + \frac{P^{NL}}{3\epsilon_0}\right) \tag{5.21}$$

When substituted into the expression for the $D = E + P/\epsilon_0$ the result is:

$$D = \epsilon/\epsilon_0 E + \left(\frac{\epsilon/\epsilon_0 + 2}{3\epsilon_0}\right) P^{NL} \tag{5.22}$$

The nonlinear polarization is preceded by a factor greater than 1, enhancing the nonlinear contribution. If one goes on to calculate the higher order nonlinear susceptibilities in the perturbative regime, the same enhancement factor appears each time the local field is involved, plus one additional contribution stemming from the nonlinear term in the displacement field. As an example, considering a third harmonic generation process where $P(3\omega) = n\alpha(3\omega)E_{loc}(3\omega) + n\gamma(3\omega,\omega,\omega,\omega)E^3_{loc}(\omega)$, the third-order susceptibility would read:

$$\chi^{(3)}(3\omega,\omega,\omega,\omega) = \left(\frac{\epsilon/\epsilon_0(\omega) + 2}{3}\right)^3\left(\frac{\epsilon/\epsilon_0(3\omega) + 2}{3}\right) n\gamma(3\omega,\omega,\omega,\omega) \tag{5.23}$$

A similar result can be derived more rigorously in the language of quantum mechanics using the density matrix formalism [226–228]: calling $S(k, \omega)$ the factor containing the local field correction due to dipole interaction, the nonlinear susceptibilities involve higher and higher power of S, with $\chi^{(2)} \propto S^3$, $\chi^{(2)} \propto S^5$ and so forth. If the local field corrections are significant, not only the dipoles involved get a boost, but the enhancement is stronger for nonlinear processes, due to the cascading nature of the correction to the susceptibilities.

Soft mode nonlinearity

As we have seen, the local field corrections provide a mechanism for coupling the vibrational dipoles to the electronic degrees of freedom. Not only this enhances the local field, providing a larger driving force for the transition, but since the dipole terms appear multiple times in the higher order interaction Hamiltonian, resulting in a cascading increase of the nonlinear response. However, for a nonlinear response to exist it is not enough to have enhanced dipole-dipole coupling, the transition must have a nonlinear character to begin with.
In low frequency transitions in a nonlinear crystal, such nonlinearity could stem from the inherent anharmonicity of rotational modes, or from saturation effects. Indeed, the polarization inside the material can not increase indefinitely, being limited by the polarizability and by the density of oscillators. Polarization saturation is indeed of crucial importance in this scenario, since the local field amplitude depends directly on the polarization amplitude. A very large external field is able to drive the system in to saturation, so that if the polarization can not increase any further the local field ends up decreasing, consequently reducing the dipole-dipole interaction: the net result is a reduction in the soft mode red shift, i.e. a polarization dependent dynamical blue shift not dissimilar from those previously observed in excitonic systems [150, 195]. We can now proceed to explore the expected behavior and the experimental signatures of such a response.

5.3 Modeling the nonlinear response of the soft mode

To understand the nonlinear response of a soft mode in a molecular crystal we performed two different kinds of theoretical calculations. On one hand, we built a toy model for a system of harmonic oscillators coupled through the Lorentz field, and we calculated its response when interacting with external

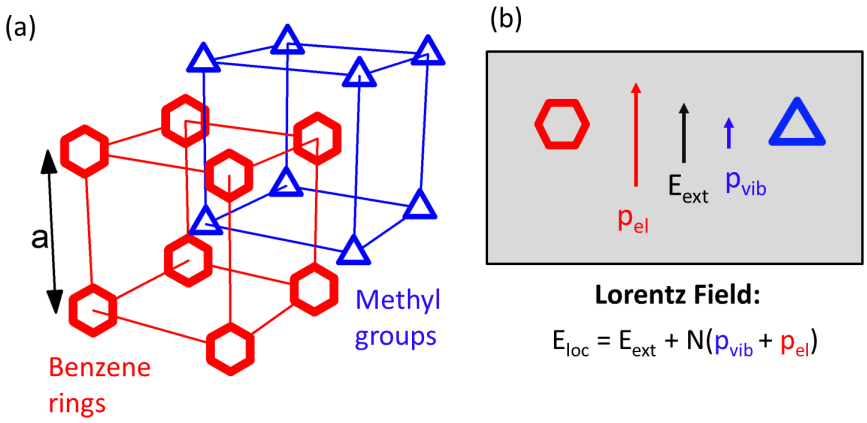

Figure 5.5: Toy model of the aspirin structure as coupled electronic (benzene rings, red hexagons) and vibronic (methyl groups, blue triangles) oscillators in a CsCl double cubic structure. The Lorentz field in the crystal depends on the polarization through the Clausius-Mossotti relation, acting as a coupling mechanism between the oscillators

electric fields. On the other hand, we explored the specific response of an aspirin crystal by calculating from first principles its response in the THz range when perturbing the dipole coupling of its phonon system. Both models will be discussed in detail in the following section.

5.3.1 Coupled Oscillators Model

Our coupled-oscillators model aims at describing a system of vibrational and electronic modes, coupled to each other by the local electric field. Since no other nonlinearity is included, the nonlinear response predicted for such a system can only be caused by the effect of the dipole-dipole coupling. Instead of modeling the complex structure of the aspirin molecular crystal, we chose a simplified picture which still describes the most relevant motions involved: the vibrational degrees of freedom, corresponding to the rotation of aspirin methyl group, and electronic degrees of freedom, corresponding to plasmonic oscillations in the benzene rings. The crystal is described by these two ensembles of oscillators, each forming a simple cubic lattice, and each object occupies the center of a cube of the other lattice as in the CsCl crystal structure (Fig.5.5.(a)).

The methyl groups are only weakly polarizable, but subject to the same Lorentz field as the benzene rings, where a large polarization can be excited by

an external field. As shown in Fig.5.5.(b), a large polarization on the electronic degrees of freedom can be the strongest contribution in the local field, allowing the methyl groups to benefit from the high dipole coupling of their neighbors. The two ensembles have transition frequencies respectively ν_v and ν_e, and are described by creation (a_v^+,a_e^+) and destruction operators (a_v,a_e) operating in orthogonal spaces. The operators are built using the Pauli matrices:

$$\sigma_x = \begin{bmatrix} 0 & 1 \\ 1 & 0 \end{bmatrix}, \quad \sigma_y = i \begin{bmatrix} 0 & -1 \\ 1 & 0 \end{bmatrix}, \quad \sigma_z = \begin{bmatrix} 1 & 0 \\ 0 & -1 \end{bmatrix} \tag{5.24}$$

with the operators being defined as:

$$\sigma^+ = \frac{\sigma_x + i\sigma_y}{2} = 1/2 \begin{bmatrix} -1 & 0 \\ 0 & 1 \end{bmatrix}, \quad \sigma^- = \frac{\sigma_x - i\sigma_y}{2} = 1/2 \begin{bmatrix} 1 & 0 \\ 0 & -1 \end{bmatrix} \tag{5.25}$$

The electronic and vibrational operators then read:

$$a_v^+ = \sigma_v^+ \otimes \mathbf{1}_e, \quad a_v = \sigma_v^- \otimes \mathbf{1}_e, \quad a_e^+ = \mathbf{1}_v \otimes \sigma_e^+, \quad a_e = \mathbf{1}_v \otimes \sigma_e^- \tag{5.26}$$

where **1** represents the identity matrix in the relevant Hilbert space.
The systems of oscillators are then made to interact with an external electric field through the Hamiltonian:

$$H = H_0 + H_{dip-dip} = (\hbar\omega_v a_v^+ a_v + \hbar\omega_e a_e^+ a_e) - E_{loc}(t)[\mu_v(a_v^+ + a_v) + \mu_e(a_e^+ + a_e)] \tag{5.27}$$

The first two terms represent the straightforward excitation of vibrational or electronic degrees of freedom, while the third term, involving the dipole moments μ_v and μ_e, couples the systems to each other.
The coupling is realized through the local Lorentz field, which is calculated from the external field $E_{ext(t)}$ and the instantaneous polarization P(t):

$$E_{loc} = E_{ext}(t) + L \cdot P(t) = E_{ext}(t) + \frac{n}{3\epsilon_0} \mathrm{Tr}[\mu_v(a_v^+ + a_v) + \mu_{el}(a_e^+ + a_e)]\rho(t) \tag{5.28}$$

where $\rho(t)$ is the system density matrix and n is the crystal specific volume. The local field correction factor for the CsCl crystal structure is L = $1/3\epsilon_0$ [225]. The strength of the dipole-dipole coupling can be tuned by adjusting the lattice constant $a = n^{-1/3}$: in particular we set our coupling parameters so that the frequency of the methyl group hindered rotation is shifted from 10 THz (for a single aspirin molecule with no coupling) to the observed 1.1 THz.
We calculate the temporal evolution of the density matrix interacting with the external field by solving the Liouville equation:

$$\frac{\partial \rho}{\partial t} = \frac{1}{i\hbar}[H(E_{loc}(t)), \rho] - \Gamma(t) \tag{5.29}$$

	$1/\Gamma_e$	$1/\gamma_e$	$1/\Gamma_n$	$1/\gamma_n$
Optimal value	1 ps	200 fs	1 ps	2 ps

Table 5.2: Coupled oscillator model of low frequency modes in a molecular crystal: damping parameters

The term $\Gamma(t)$ contains the phenomenological amplitude and phase relaxation terms, calculated following [229].

$$\Gamma(t) = \frac{\Gamma_e}{2}(2a_e\rho a_e^+ - a_e^+ a_e\rho - \rho a_e^+ a_e) \quad + \tag{5.30}$$

$$\frac{\gamma_e}{2}(2a_e^+ a_e\rho a_e^+ a_e - a_e^+ a_e a_e^+ a_e\rho - a_e^+ a_e a_e^+ a_e\rho) \quad + \tag{5.31}$$

$$\text{Vibrational terms} \tag{5.32}$$

Here the terms in Γ describe amplitude damping of an oscillator, while terms in γ correspond to a phase damping with no energy damping [230]. The damping parameters are in principle unknown. They have been chosen to retrieve the correct frequency shift, and to optimize the correspondence to experimental results: the damping rates used in the simulations presented in the following sections are listed in Tab.5.2. The phase damping rate in particular regulates the loss of coherence in the system, so a large value of γ is essential to have long lived coherent local fields.

At each step, the local field is calculated from the instantaneous value of the polarization $P(t) = \mathrm{Tr}\rho(t)(\mu_e + \mu_v)$. The current density in the sample is the time derivative of the polarization, including its electronic and vibrational components: $J = \mathrm{Tr}\rho(t)(\omega_v\mu_v + \omega_e\mu_e)$. For the chosen coupling strength the electronic component of the current dominates over the vibrational, confirming that the soft mode is close to the polarization catastrophe.
If we consider a sample interacting with two THz fields we can then calculate the nonlinearly emitted field $E_{NL}(t,\tau)$ by comparing the radiated field E_{em} with and without the pump, and we can compare it directly to the nonlinear field observed in our 2D experiments.
To better understand the soft mode nonlinear response, however, it is useful to begin by observing the coupled oscillator model response to a single beam, before moving on to the effects of two beams of varying intensity. In the next paragraph both situations will be analyzed.

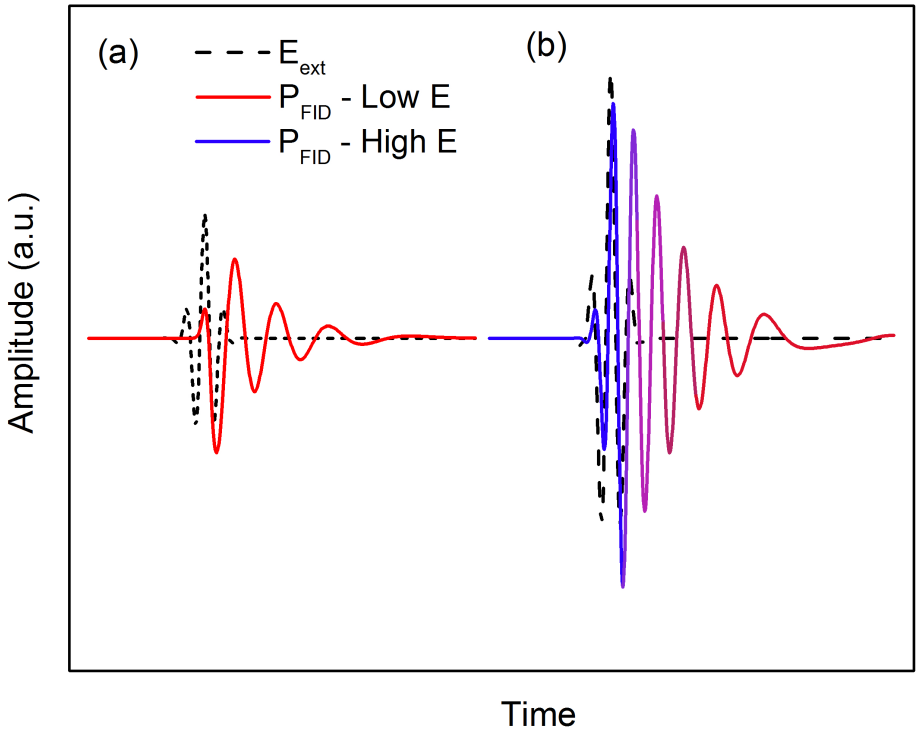

Figure 5.6: Free induction decay of the polarization created by a low (a) or high (b) external driving field (dashed black line): for a strong excitation, the FID first is strongly blue shifted and returns to the unperturbed lower frequency as the excitation relaxes.

Polarization-dependent emission frequency

In a regime of strong dipole-dipole coupling, the free induction decay (FID) of the induced polarization can dominate the local Lorentz field. A high polarization can result in saturation, if the external field is strong enough, reducing the local field. The observable outcome is a blue shift of the transition frequency for a high enough driving electric field, stemming from a less marked softening of the mode. As the polarization recovers, however, the local field can again increase, so that the soft mode gradually shifts back to its original frequency. The electric field emitted by the FID of the polarization, having the same instantaneous frequency as the soft mode, is down-chirped.

The FID caused by external fields of different amplitude is shown in Fig.5.6: panel (a) describes the effect of a weak driving field (dashed black), resulting in a FID (solid red line) at the frequency of the soft mode "at rest". Panel (b) on the other hand shows a the effect of a driving field strong enough to bring

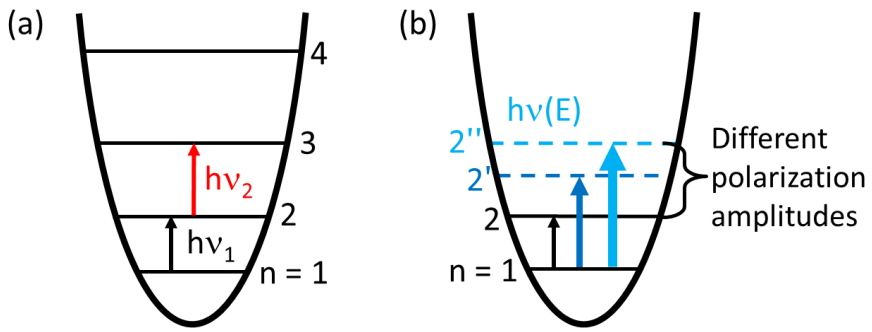

Figure 5.7: Comparison between the anharmonic ladder and the nonliearity due to dipole dipole interaction: for the anharmonic ladder of levels (a) the emission frequency is set by the levels spacing, and a dispersive signal stems from changes in the level population. For dipole-dipole nonlinearity, the emission frequency of the FID depends on the polarization amplitude: a larger pulse amplitude (different arrow size) results in a larger blue shift.

the system to the nonperturbative regime: at first the FID emission is strongly blue shifted compared to panel (a), but it reverts back to its original frequency as the polarization relaxes.

The chirp on FID electric field highlights an important difference between the soft mode nonlinearity and the more conventional nonlinear response of an anharmonic ladder, e.g. the response of a rotational excitation. The scheme in Fig.5.7 illustrates the crucial difference between the two nonlinearities. Panel (a) shows an anharmonic ladder, with uneven spacing between the different excited stated ($E \propto n^2$). If a pump pulse (black arrow) creates an excited population on the first excited state, the nonlinear response to a subsequent probe pulse (red arrow) will consist of a bleaching of the $1 \rightarrow 2$ transition and induced absorption on the $2 \rightarrow 3$ transition, stemming from the interference of the excited polarizations with the probe electric field. The positive and negative nonlinear signal will appear at characteristic frequencies ν_1 and ν_2, fixed by the anharmonic potential which sets the levels spacing. The shape of the dispersive signal, away from saturation, is set by the population created by the pump, and not by the probe amplitude.

The nonlinear response driven by dipole-dipole interaction, shown in panel (b), is more complicated. The pump induces both a population and a polarization: the population excitation causes a bleaching at the transition frequency similar to that of the anharmonic ladder. induced absorption however does not appear at a fixed frequency position, but at a field dependent frequency $\nu(E)$

determined by the amplitude of the induced polarization. For a strong external driving filed, the local field is reduced by polarization saturation: the larger the polarization, shown in the figure as thicker arrows, the higher the frequency shift.
Crucially, also the probe induced polarization drives the system closer to saturation, causing a dynamic blue shift: the amplitude of the probe polarization, and not only the population created by the pump, determine the bandwidth of the transmitted field. Normally, the nonperturbative regime would be reached when the population excited by the pump is close to saturation. For this soft mode nonlinearity, the polarization saturation created by the probe pulse can drive the system to the nonperturbative regime by inducing a blue shift of the transition frequency larger then the bandwidth of the soft mode itself: in that case we would observe a dispersive nonlinear signal, strongly dependent on the probe field amplitude, even at intensities far from population saturation.

In a 2D experiment we go on to measure the difference in the probe FID with an without a pump pulse present: out of the perturbative regime, the pump-probe response is the interference of the down-chirped FIDs. The dynamic dependence of the emitted field frequency on the local field amplitude can give rise to complex behaviors varying the pulses amplitude or delay.
Fig.5.8 shows such difference for a weak (a) or intense (b) probe pulse, shown as black dashed line. The solid red line shows the difference between the emitted field with and without a pump pulse: for a weak probe it does not show any chirp, much as the signal from an anharmonic ladder. Its frequency resolved transmission change (red line in panel (c)) has the expected dispersive signature of a blue shifted transition.
The situation is quite different for a strong probe (dashed black line, Fig.5.8.(b)), taking the interaction in the perturbative regime: due to the chirp of the probe FID, the difference signal (solid blue line) also shows a downchirp. The envelope shape of both pump and probe in this regime can strongly affect the nonlinear signal, even resulting in an inverted dispersive signal for certain pump-probe time delays: the blue line in panel (c) shows the calculated transmission change for strong pump and probe pulses of equal amplitude, demonstrating the inverted dispersion.

5.3.2 Ab-initio calculations

The coupled oscillator model we presented is quite powerful in describing the nonlinear response of a highly-coupled system, but it does not specifically describe an aspirin crystal. To gain a more quantitative understanding of the re-

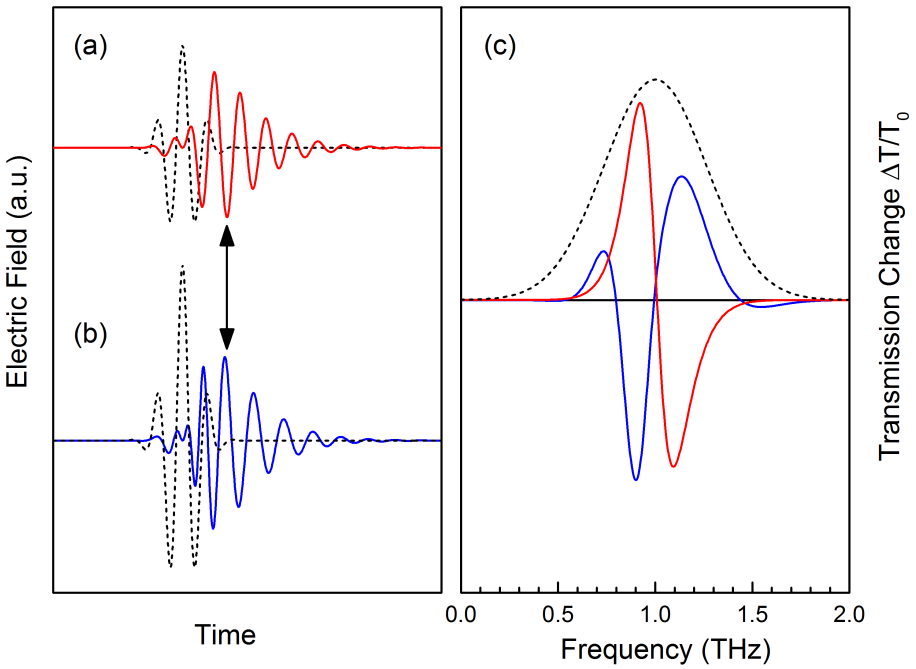

Figure 5.8: Difference in the probe polarization FID with and without a pump pulse for a weak (a) or high (b) probe field, shown as a dashed black line. In the weak case, the nonlinear field (solid red line) is not chirped, and shows a typical dispersive pattern for a blue shift in transmission change (red line in panel (c)). For a stronger probe, the nonlinear signal is chirped and exhibits inverted dispersion (blue line). The dashed black line represents the probe pulse spectrum.

sponse of our sample, we collaborated with Alexander Tkatchenko and coworkers to describe the aspirin response with first-principle calculation.

Their previous work on aspirin [202], which pointed to the collective nature of aspirin low frequency mode and to its importance for crystal structure stability, focuses on capturing the long range many-body interaction typical of condensed phase matter, and molecular crystal in particular. Their description of aspirin crystal structure starts from DFT calculations based on the Perdew-Burke-Ernerzhof functional (PBE) [231], within the all-electron code *FHI-aims* [232] to describe molecular orbitals. However, semi-local functionals such as the PBE can be lacking in their description of long range electron correlations: the inclusion of van der Waals interaction through the Tkatchenko-Scheffler method (TS-vdW) [233], which computes the van der Waals interaction energy by summing over pairwise contributions, improves results for polarizability and free

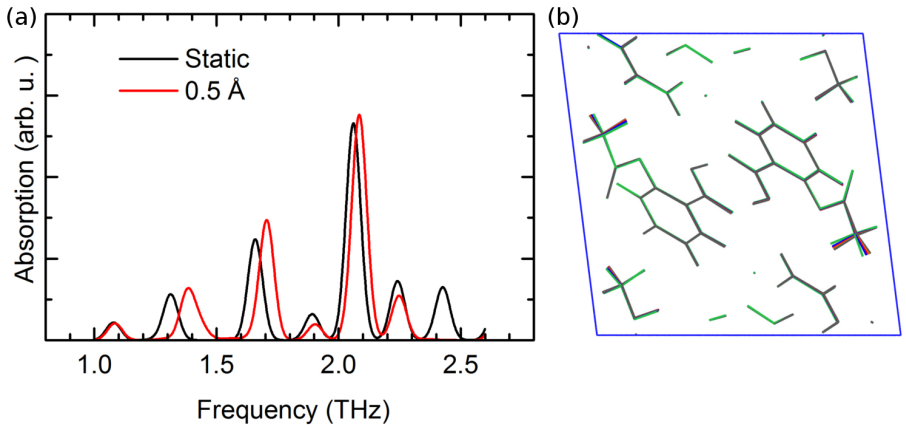

Figure 5.9: (a) Ab initio calculation of aspirin absorption spectrum for the optimized aspirin crystal structure (black) and for a small displacement on the normal coordinate associated with the soft mode (red). The displacement corresponds to a reduced coupling, resulting in a blue shift of the low frequency hybrid mode (b) Calculated aspirin structure for different methyl group displacements: the static structure is shown in grey, the smallest displacement is 0.5 $\mathring{A}$ in red and the highest 4 $\mathring{A}$ in green.

energy of diluted or small-scale systems, but systematically overestimates the stability of larger structures by neglecting higher order screening effects.

The more recent development of the Many Body Dispersion method (MBD) [234] allows for very precise description of molecular crystals. It calculates crystal structures by efficiently separating correlations on different spatial ranges [235]. in a first step, the bare atomic polarizabilities are calculated using a PBE-TS technique, considering each atom as a single quantum oscillator. The long range interactions can then be described in terms of dipole interactions among the oscillators. A screening term is first computed self-consistently describing how the bare polarizabilities are modified by dipole-dipole interactions. Finally, correlation energy is calculated separately for long and short range interactions: the short range component is provided by semi-local DFT calculations, while long range contributions are calculated starting from the screened polarizabilities and describing their Coulomb interaction in the dipole approximation. This strategy ensures good results both in materials characterized by short range interactions like small molecules, as well as low absolute errors for condensed phase and molecular crystals.
The PBE-MBD code as been used to calculate the aspirin crystal structure to a high degree of accuracy: the 1.1 THz hybrid mode in particular, which involves

concerted motions of methyl groups in different molecules, appears at the correct frequency only when accounting for many-body van der Waals interactions. To model its nonlinear response, however, some mechanism to tune the phonons dipole coupling must be included. Phonon calculations were performed by finite difference method using the FHI-aims code for electronic orbitals together with the first principle phonon calculator *phonopy* [236]. The model calculates assumes the motions are harmonic, using harmonic constants from DFT calculation, without anharmonic effects. It also neglects any effect on the phonons and momentum frequency coming from electronic motions.

In this framework, the soft mode stems from the sum of two components, a purely rotational contribution centered at 1.1 THz, and the hybrid contribution which in the theory appear at 1.3 THz. The inclusion of anharmonicity and electronic effects leads to the correct 1.1 THz mode in static calculations. Higher lying vibrational modes are also nonlocal, involving concerted motions of many groups in the unit cell.

Since in a periodic unit cell only changes of dipole moments are well defined, the modulation of dipole moments μ_j were calculated by recording their change upon displacing the crystal structure along a normal coordinate Q_j. The intensity of the THz response of a vibrational mode is then given by:

$$I_j \propto \left(\frac{\partial \mu_j}{\partial Q_j}\right)^2 \tag{5.33}$$

The displacement of each atom in the structure is then calculated as:

$$\delta_i = \frac{A}{\sqrt{N m_i}} e_i \tag{5.34}$$

where N is the number of atoms in the cell, m is the atomic mass, e_i the eigenvector of the phonon mode and A the displacement amplitude. After calculating each atom displacement, the crystal structure was optimized for the new geometry, corresponding to a different value of the dipole coupling. The THz response was calculated for different values of maximum displacement A_{max}, from 0.5 to 4 Å$\sqrt{\text{amu}}$. Figure 5.9.(a) shows the THz spectra for the optimized aspirin crystal structure (black line) and for a small displacement of 0.5 Å$\sqrt{\text{amu}}$: all the modes appear shifted to higher frequencies, confirming that an increase a modulation in coupling strength will result in a dynamic shift of the THz response frequency. Larger and larger displacements correspond to higher frequency shifts. Applying a very small displacement of 0.1 Å$\sqrt{\text{amu}}$, only the 1.3 THz mode is affected, and for higher perturbations it exhibits the highest amount of frequency shift: as one would expect, the soft mode frequency is most sensitive.

The different structures are shown in Fig.5.9.(b). The peak shift can be ex-

plained in terms of geometry of the aspirin structure: increasing displacements correspond to different torsion angles of the methyl groups, ranging from 0.6° to 11° for maximum displacement. At high torsion angles, the plasmon phonon coupling responsible for the soft mode enhancement is deactivated, resulting in the observed blue shift.

5.4 2D THz spectroscopy

To look for experimental signatures of the soft mode nonlinear response, aspirin samples were studied in our 2D spectroscopy set-up described in 3.4.1. As a sample we used pure crystalline aspirin, in order to maximize collective effects which rely on closely packed aspirin molecules. The material was ground to a fine powder and then pressed in tablets, since commercially available aspirin crystal don't offer an interaction volume large enough to overcome the comparatively small coupling to radiation in this spectral range. A powder sample however means that the orientation of the soft mode axis with respect to the electric field is randomized, making effective field highly variable with the local geometry.
A sample thickness of 450 μm was chosen: we selected the thinnest tablets where the 1.1 THz feature could still be observed clearly by linear spectroscopy, maximizing the transmitted field compared to thicker tablets. To reduce thermal noise, the sample was kept at cryogenic temperatures (∼30 K) using a closed-circuit liquid helium cryostat.

2D experiments

To isolate the soft mode nonlinear response we sent on our sample two collinear beams centered around 1.5 THz, with a variable delay between them. A typical 2D measurement in shown in Fig.5.10.(a): the horizontal axis corresponds to the real time t, the delay between the beams and the EOS probe, while the vertical axis is the coherence time τ, the delay between the two pulses. We define the delay time as $t_B - t_A$, assuming positive values when pulse A reaches the sample first. The two beams, focused by a parabolic mirror, show different field amplitude on sample due to the focusing geometry: the THz field B, coming at a fixed time, has a field amplitude of 50 kV on sample, while beam A, coming at a variable delay, has a peak field amplitude of 25 kV/cm.

The nonlinearly emitted electric field is extracted from the transmitted field by subtraction: $E_{NL}(t,\tau) = E_{A,B}(t,\tau) - E_A(t) - E_B(t,\tau)$. Due to the strong electric fields on the detector, some DC nonlinear response from the ZnTe crystal appears at the pulse overlap, but knowing the response function of the EOS

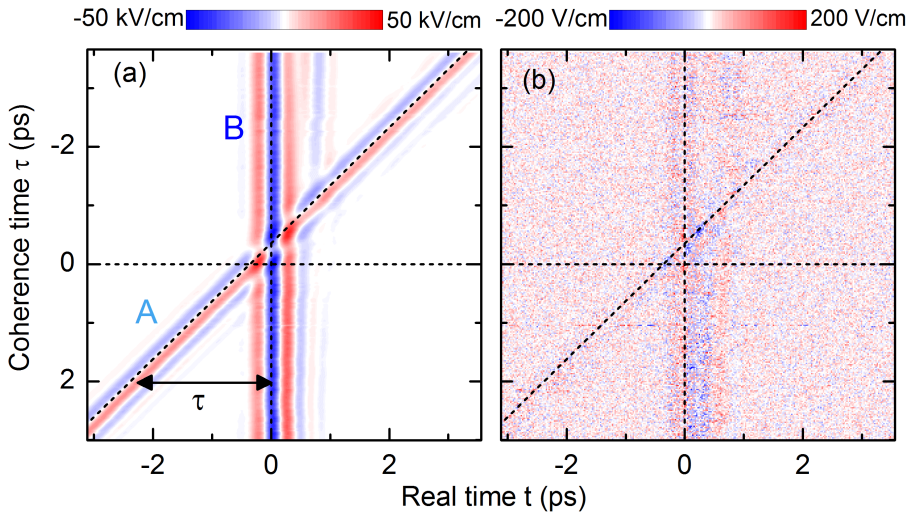

Figure 5.10: (a) Transmitted field through 450 μm thick aspirin sample, as a function of real time (horizontal axis) and delay time (vertical axis). The dashed lines mark zero time delay and the position of the two THz pulses (b) Nonlinearly emitted field, extracted by subtraction

detection system this spurious signal can be eliminated by tuning the arc sine filter function used to calibrate the electric field measurement. The retrieved nonlinear field, shown in Fig.5.10.(b), is close to the noise level, due to the weak coupling of the effective electric field to the powdered molecular crystal. Careful analysis in the frequency domain still allows us to retrieve the different nonlinear signal components and to analyze them independently.

Nonlinear signal

By applying a Fourier transform along both time axes, the nonlinear signal can be studied in the frequency plane, where different spots can be linked to different pulse interaction sequences (Sec.3.3). Fig.5.11.(a) shows a typical nonlinear signal for aspirin. The horizontal axis shows the detection frequency ν_t, corresponding to oscillations along the real time axis, while the vertical axis along the excitation frequency ν_{tau}, corresponding to oscillations along the coherence time.

The nonlinear signal shows three main features related to the low frequency soft mode: the A pump-B probe signal at ($\nu_t = 1.5$, $\nu_{tau} = 0$) THz (red circle), non-rephasing components of the B pump-A probe signal at ($\nu_t = 1.5$, $\nu_{tau} = 1.5$) THz (light blue) and the rephasing A-B-B photon echo at ($\nu_t = 1.5$, $\nu_{tau} =$

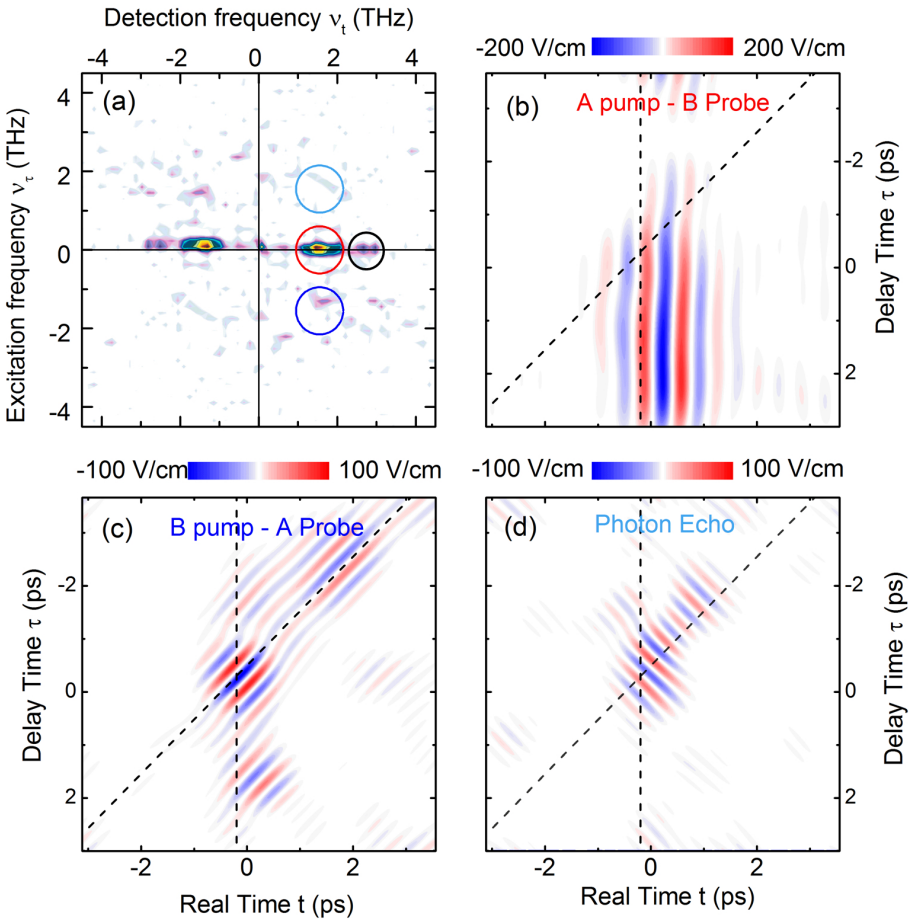

Figure 5.11: (a) Nonlinear signal in the Fourier plane: the major contributions come from the pump-probe signals. After selecting each signal with a gaussian filter, the electric fields are retrieved in the time domain as a function of real time and coherence time, as shown in the other panels (b) A pump-B probe signal (red circle in the frequency plane) (c) B pump-A probe signal, non-rephasing component (dark blue circle) (d) Rephasing photon echo component (light blue circle)

-1.5) THz (dark blue). The B-A-A photon echo, at (ν_t = 1.5, ν_{tau} = -3) THz, can not be separated from the noise. One additional spot can be observed at (ν_t = 2.6, ν_{tau} = 0) THz (black circle), showing the nonlinear response of higher lying absorption lines in the THz spectrum.

Each signal has been isolated using a 2D gaussian filter, thus excluding contributions from other effects and all the noise stored in the rest of the two-dimensional frequency matrix. By back transforming into the time domain the weak non-

linearly emitted fields can be resolved with a high degree of accuracy even at field amplitudes of tens of V/cm. The electric fields corresponding to different spots are shown in panels (b)-(d) in the time domain. The dashed black lines indicate the position of the driving fields, delimiting the causal range.

5.5 Discussion: experimental signatures of the blue shift

In this section the different signals appearing in the nonlinearly emitted field will be analyzed one by one looking for fingerprints of the dynamic blue shift of the soft mode, in particular in the dispersive behavior of the spectrally resolved pump-probe signals. The role of the long lived local field driving the interaction will emerge from the photon echo signal defying strict time ordering rules. Finally, even absorption lines at higher frequencies show a blue shifted nonlinear response, although weaker than that of the soft mode.

5.5.1 A pump-B probe signal

The pump-probe signal E_{pp}^{AB} (Fig.5.11.(b), red circle) is given by:

$$S_{PP}^{AB} = 2\mathrm{Re}\left(\frac{E_{pp}^{AB}(\nu_t,\tau)E_B^*(\nu_t)}{|E_B(\nu_t)|^2}\right) \tag{5.35}$$

and shown in Fig.5.12.(a) as a function of detection frequency ν_t on the horizontal axis and delay time τ on the vertical axis: in the color scale red denotes a transmission increase and blue a decrease. The peak value of the pump-probe signal is of the order of $5 \cdot 10^{-4}$.

It is interesting to note that from our linear absorption measurement (Fig.5.2) we can estimate a very low dipole moment for the 1.1 THz mode, of the order of 0.1 pm: this would only support an excited electron density of the order of $5 \cdot 10^{-8} \cdot e$, corresponding to a pump-probe signal of a similar order of magnitude. Even from this rough estimate, it is apparent that in presence of strong electric fields an enhancement of the transition dipole enables detection of a pump-probe signal: without cascading dipole strength enhancement, a nonlinear response would hardly be detectable.

As expected from a blue shifted transition, the pump-probe spectrum shows a bleaching of the original transition frequency at 1.1 THz and induced absorption at 1.5 THz. The dispersive behavior can be seen more clearly in Fig.5.12.(c), showing the transmission change as a function of ν_t for a fixed time delay $\tau = 1.6$

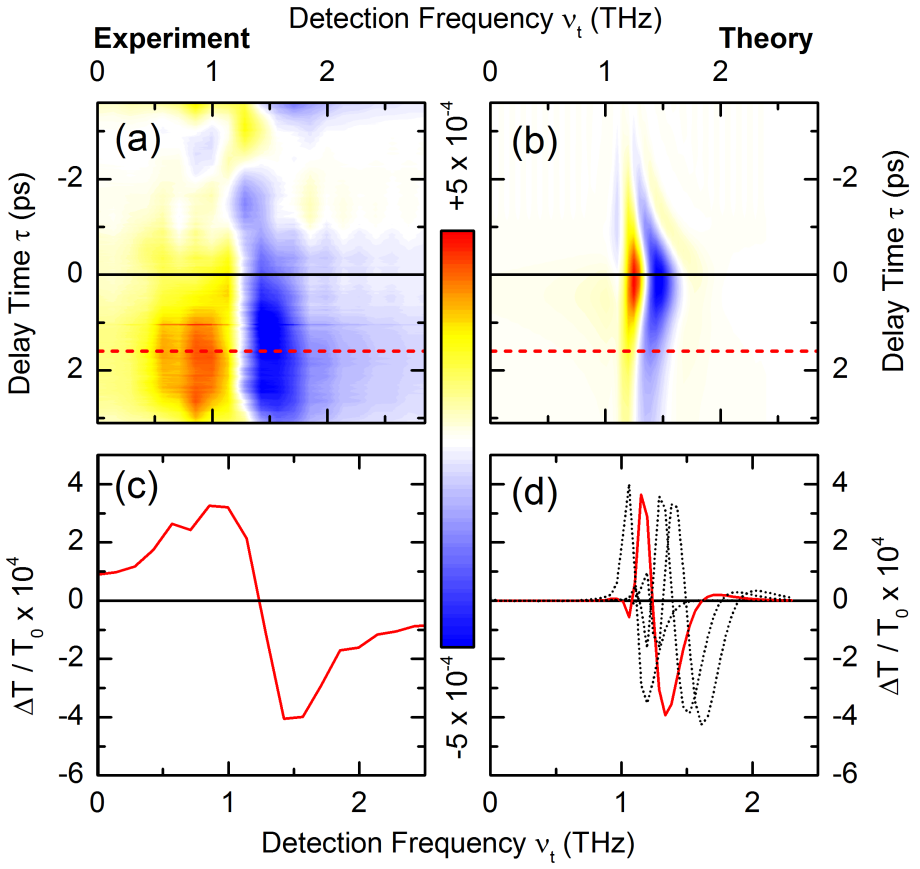

Figure 5.12: A pump-B probe signal: the spectrally resolved pump-probe in panel(a) shown the experimental transmission change as a function of detection frequency and delay between the pulses. Panel (c) shows a cut at 1.7 ps time delay, showing a blue shift in the absorption frequency. Panels (b) and (d) show the corresponding results simulated using the coupled oscillators model. The dotted black lines in panel (d) represent the pump-probe response for slightly different local electric fields, which results in different frequency shifts: a superposition of responses in crystallites with a different orientation explains the large broadening in the experimental data

ps (dashed red line in the above panel). The observed 0.4 THz frequency shift is quite large, 40% of the stationary transition frequency.
In the same figure, panel (b) and (d) show the corresponding signal calculated using our coupled oscillator model: the experimental signal is well reproduced, in terms of retrieving the transition blue shift. The best fit for our experimental result was obtained for field strengths $E_B = 30$ kV/cm and $E_A = E_B/2$.

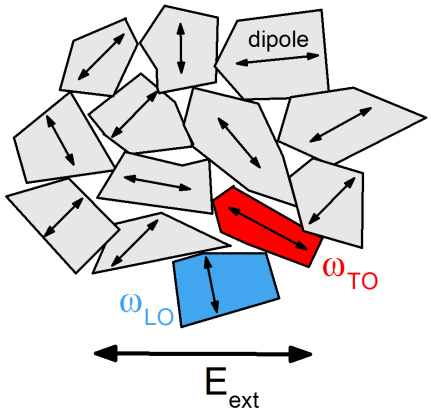

Figure 5.13: The orientation of crystallites in a powder samples influences the phonon frequency depending on the relative orientation of the soft mode dipole (black arrows) with respect to the symmetry axis of each crystal. For an oblate crystallite (light blue), the phonon will appear at ω_{LO}, while for a prolate crystallite (red) at ω_{TO}. The coupling to an external electric field is also affected by the geometry, depending on the orientation of the dipole compared to the field polarization.

The bandwidth of the calculated pump-probe signal (panel (d)) is considerably narrower than in the experiment: this might be due to inhomogeneous broadening in our pressed powder sample, which is not accounted for in the theoretical model. More important, the randomized orientation of the molecule in the powder affects the amplitude of the external electrical field projected on the molecular axis with the most efficient coupling: since the blue-shift is field-dependent, this further enhances the line broadening in the experiment. In Fig.5.12.(d), the dashed black lines represent spectrally resolved pump-probe signals at the same $\tau = 1.6$ ps delay, for different driving fields strengths (E_B =20, 40, 60 kV/cm): the contributions coming from the field projection for different crystallites add up to a much broader overall signal. A lower effective field can also account for the mismatch between the experimental field amplitude and the best fit in out theoretical model.
Furthermore, the frequency of the phonon itself might be influenced by the shape of the crystallite (Fig.5.13): the fundamental lowest phonon frequency varies in a range between the LO and TO mode depending on the orientation of the longest dimension in the crystal [237]. If the soft mode axis is parallel to the symmetry axis of a prolate crystallite (colored in red in the figure) it will oscillate at the transverse frequency ω_{TO}, at the longitudinal frequency ω_{LO} for

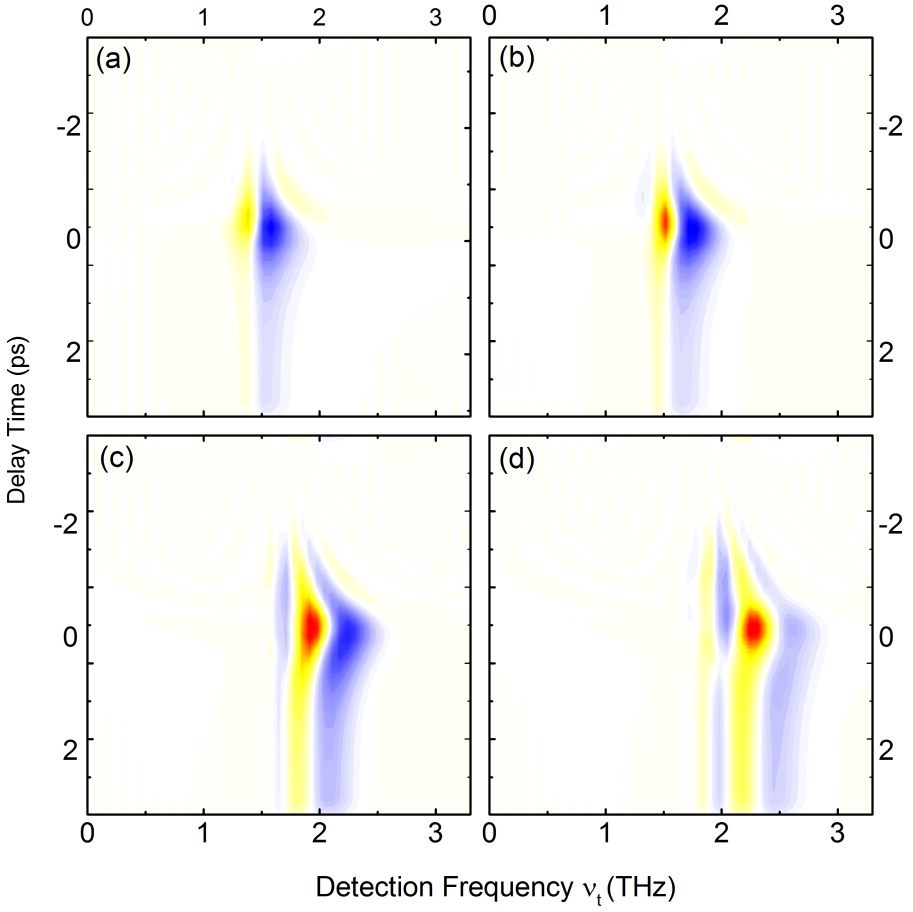

Figure 5.14: Comparison between the calculated A pump-B probe signal probe field strengths of 10,20,40 and 60 kV/cm (a)-(d). In panel (a), which is still in the perturbative regime, no blue shift is present, while in panel (d) the blue shift is most pronounced.

an oblate crystallite(light blue), and at intermediate frequencies for in-between cases [238, 239].

The amount of soft mode blue shift depends directly on the probe field amplitude: Fig.5.14 shows the pump-probe signal calculated for different probe strengths (using lower dephasing time), increasing from panel (a) to panel (d). As the probe field is increased, the nonlinear signal appears at higher and higher frequencies, and the pump-probe shows multiple modulations from bleaching to induced absorption. The lowest amplitude field corresponds to an interaction still in the perturbative regime, where the frequency shift is smaller than the soft mode bandwidth. In this interaction regime, the pulses envelope, and the

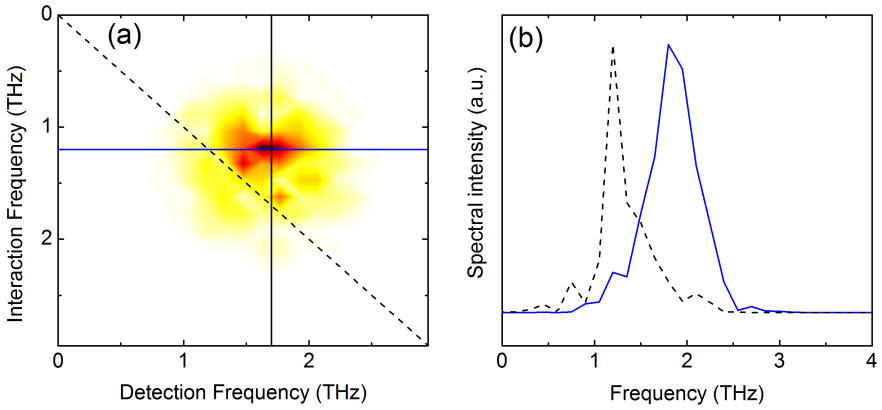

Figure 5.15: (a) Non-rephasing component of the B pump-A probe signal, lying off the diagonal of the frequency plane (b) Cut of the 2D signal at the maximum position along the detection and emission frequency, showing a shift of the peak frequency from 1.1 THz in the interaction frequency to 1.8 THz long the detection frequency

exact probe amplitude do not affect the nonlinear response: the B pump-A probe signal would be identical to this one, only at opposite time delays.
Our experimental situation however is strongly nonperturbative, and due to the different probe amplitude the B pump A probe signal looks markedly different: since in our case pulse A is less intense and has a different temporal envelope than pulse B, the B pump-A probe signal is both less intense and qualitatively different then the one we just analyzed.

5.5.2 B pump-A probe signal

The B pump-A probe signal can be found at the (+1.5, -1.5) THz spot in the frequency plane (Fig.5.11.(a), dark blue circle, and Fig.5.11.(c) in the time domain) corresponding to the non-rephasing component of the FWM signal. By taking a closer look at the spot in the frequency domain we notice that the nonlinear response involves a blue shift: the spot is not exactly on the Fourier plane diagonal, as would be expected for a classic pump-probe response, but lays slightly above it (Fig.5.15.(a)): the black and blue lines identify the peak position respectively on the detection and excitation frequency axis. The cuts along those lines are shown in Fig.5.15.(b): the peak shifts from light being absorbed at 1.9 THz (solid blue line), to being transmitted at 1.1 THz (dashed black line).

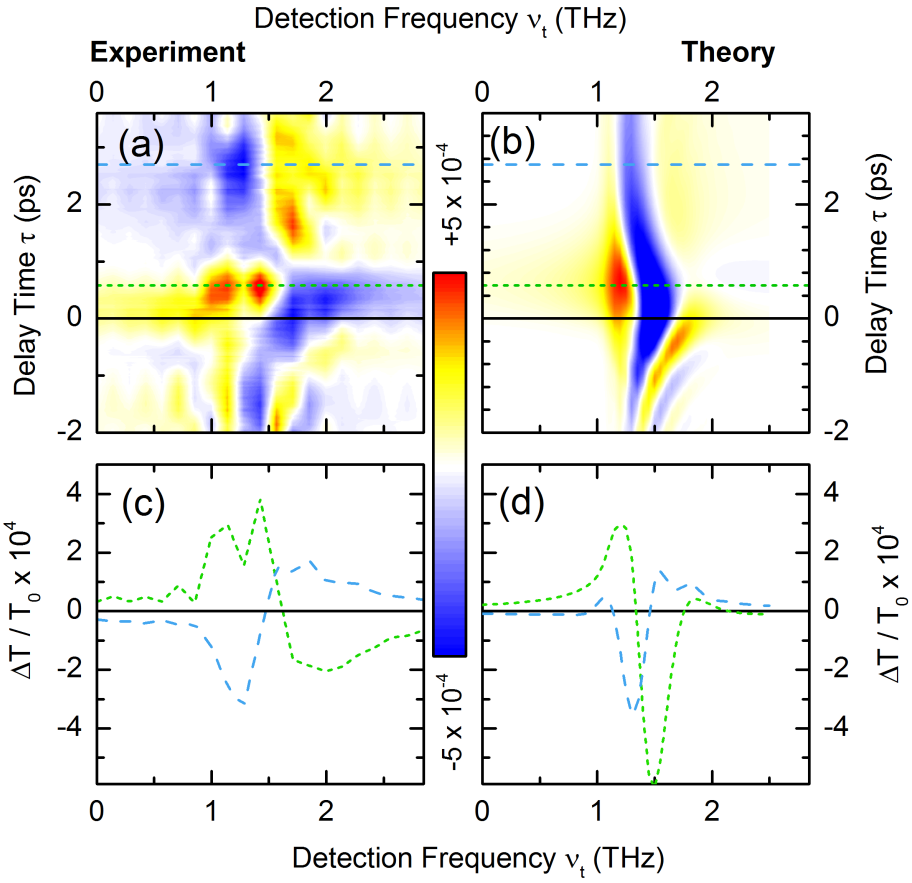

Figure 5.16: Spectrally resolved transmission change for the B pump- A probe signal, as measured (a) an calculated from our coupled oscillator model (b). Panels (c) and (d) show cut at different time delays: the light green line at a delay near the pulse overlap shows a strong blue shift, while the light blue line at a later delay time, when the probe interacts with the down-chirped polarization decay, shows inverted dispersion.

The 0.8 THz frequency shift is larger than for the A pump-B probe, since in this case the interaction is driven by the stronger pulse B. To gain more insight into the dynamics of the response, we can look again at the full spectrally resolved pump-probe signal, shown in Fig.5.16.(a) as a function of detection frequency and time delay.

Compared to the A pump-B probe, the signal has a more intricate structure: shortly after the pulse overlap we observe the expected blue shift, with a bleaching at 1.1 and 1.5 THz, and induced absorption at 1.9 THz. The dashed green line denotes a cut at $\tau = 0.6$ ps, shown in Fig.5.16.(c) in the same color: the

bleaching peaks at the unperturbed transition frequency, with a second smaller peak in the same position as the A pump-B probe signal.
At later delays, the nonlinear response acquires an inverted dispersive behavior, with a bleaching at higher frequencies and induced absorption around the original 1.1 THz line, as shown by a cut at 2.7 ps delay (light blue line). This can be interpreted in light of the dynamical relationship between the frequency of the polarization FID, and the amplitude of the polarization itself. The strong B pump initially creates a highly blue shifted FID, acting as the driving local field, and as the polarization decays the transition line gets closer and closer to the unperturbed frequency resulting in a sharply down-chirped free induction decay field. At an early delay time the probe interacts with an highly blue shifted pump, resulting in two peaks for the bleaching, while at a later time the probe will mix with the less intense, down chirped part of the FID: this can indeed result in inverted dispersion for a strong enough pump pulse.
As for the A pump-B probe, here panels (b) and (d) show the results of a simulation with our coupled oscillator model: using the same pulse amplitudes we can achieve a good qualitative agreement with the experimental data. In particular, the inverted dispersion at later delay time can only be achieved with strong enough driving pulses, while for weaker field the pump-probe shows only a blue shift a short delays.

5.5.3 A-B-B photon echo

The photon echo field (Fig.5.11.(d), light blue circle in the frequency plane) is very weak, but showcases an interesting feature. Its spectral position at (1.5, 1.5) THz links it to the A-B-B pulse sequence, which due to time ordering of the pulses should only be present for $\tau > 0$, in the lower half of the panel. However the photon echo signal in the time domain (Fig.5.17.(a)) is clearly present also at negative time delays.
Furthermore, in more conventional IR spectroscopy we would expect its spot in the frequency plane to lie on the diagonal, but in the close up in Fig.5.17.(c) the spot appears quite short along the diagonal (dotted line), and extended mostly perpendicularly to it.
As we discussed in Sec.3.5 when the fields driving the interaction are long lived beyond the semi impulsive limit, strict time ordering of the pulses can not be applied. Indeed this points to the polarization FID, which lasts for picoseconds after the external field has passed through the material, acting as the main local driving field. In this case, even if pulse B arrives first on the sample, the field radiated by its induced polarization can interact with the local field due to pulse

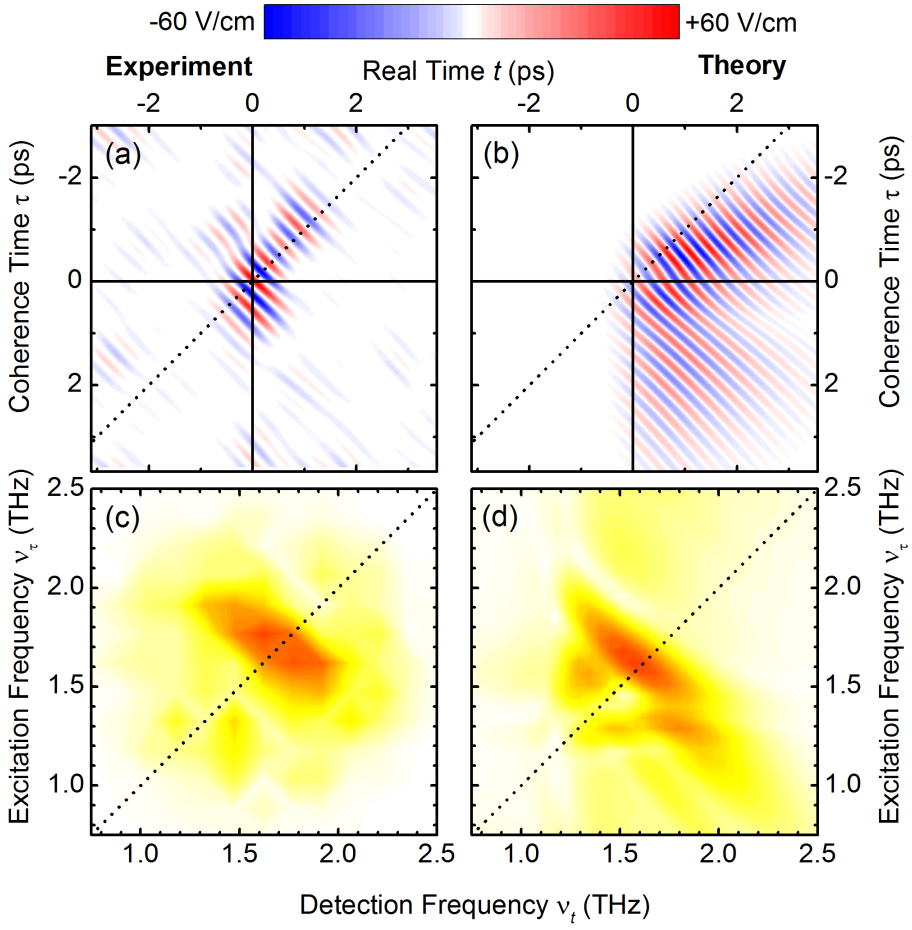

Figure 5.17: The photon echo signal extends to negative delay times (a), as in the frequency domain it extends mainly across the frequency plain diagonal (b). Our coupled oscillator model can reproduce this effect (panels (b) and (d))

A in an A-B-B pulse sequence even at negative time delays.

Figure 5.17.(b) shows the photon echo signal calculated with our coupled oscillator model, again appearing at both positive and negative delay times. Two impulsive driving fields can not produce such a response.

The peculiar shape of the spot in the frequency plane can be easily understood if we consider the down-chirped FID of the polarization in presence of a strong driving field. The mechanism is similar to that driving the change in dispersion shown in the B pump-A probe signal: for the A-B-B photon echo too, the local fields have a different frequency at different time delays, resulting in a looser relationship between detection and excitation frequency. The dynamical dependence of the driving field frequency on the strength of the induced polarization

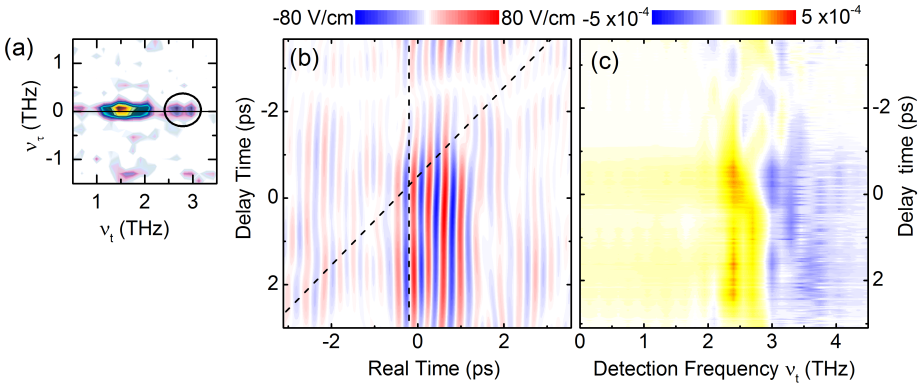

Figure 5.18: Nonlinear signal at 2.4 THz in the frequency domain (black circle,(a)), and corresponding time domain (b) electric field. (c) Spectrally resolved pump-probe, showing a dispersive behavior consistent with a small blue shift of the 2.4 THz absorption line

results in a signal shape across the frequency plane diagonal, which is well reproduced by our calculations (Fig.5.17.(d)).
In the time domain, the simulated signal is quite long-lived along the real time direction, contrary to the measured photon echo. This can also be accounted for by the inhomogeneity introduced by the powder sample. The echos emitted by differently oriented molecules, exhibiting varying degrees of blue shift, are not phase locked: they interfere destructively shortening the signal on the t axis.

5.5.4 Effect on the 2.4 THz mode

The soft mode at 1.1 THz experiences the strongest dynamic frequency shift, however the ab-initio calculations we performed predict that also higher-lying vibrational modes will be similarly affected, albeit less significantly. The smaller size of the effect could be attributed to multiple factors: first of all, the collective enhancement of dipole strength relies on contributions from polarizable modes at higher frequencies, favoring a larger effect on the lowest phonon. Furthermore, the methyl group rotation has a high degree of anharmonicity, fostering a higher nonlinear response, while signal from more harmonic modes will predictably be weaker.

Even though it is at the very edge of our pulses' spectrum, we can observe a small blue shift on the 2.4 THz mode. In Fig.5.18.(a), the black circle shows a nonlinear signal in the frequency plane at (2.5,0) THz: Figure 5.18.(b) shows the corresponding electric field in the time domain. The signal has two peaks in

the frequency domain, one at 2.4 THz, corresponding to an electric field mostly in the pulses overlap, and one at 2.8 THz extending also to higher time delays. Since the nonlinear electric field is very weak, we analyzed both peaks at the same time.
The spectrally resolved pump-probe signal is shown in Fig.5.18.(c): as for the 1.5 THz mode, it displays a blue shift signature with a bleaching at 2.4 THz and induced absorption at higher frequency-even though the decrease in transmission appears quite weak, since in that spectral range we detect very little light.

5.6 Conclusions: soft mode nonlinear response in molecular crystals

In this chapter we explored the behavior of aspirin vibrations in the THz range. The lowest lying aspirin phonon lies at 1.1 THz, and it stems from a hybrid vibrational-electronic motion: the concerted motion of methyl groups in the 4 aspirin molecules in the crystal unit cell is coupled to electronic oscillations in the benzene rings. The dipole-dipole coupling stems from local field corrections: the highly polarizable electronic degrees of freedom create a high local field dominated by the polarization FID, which lends the dipoles' oscillator strengths to the vibrational modes. This behavior is strikingly similar to a soft mode close to the polarization catastrophe, as the dipole-dipole coupling pushes the hybrid mode frequency to its low frequency.
This nonlinearity was analyzed theoretically both through ab initio calculations on the phonon system of the aspirin crystal, and by a model involving two sets of coupled harmonic oscillators. The response to a strong external field is dominated by saturation of the polarization, which reduces the local field responsible for the coupling. When the coupling decreases, the mode hardens and its response is blue shifted. As the polarization recovers the coupling can increase again, restoring the mode to its original frequency. As a result, the emitted field from the polarization FID is down-chirped. Since the mode frequency depends dynamically on the instantaneous polarization in the material, this nonlinear response is quite different from that a more conventional anharmonic ladder with fixed transition frequencies. Here, the response becomes highly nonperturbative as soon as the frequency shift bandwidth is larger then the transition line, regardless of the amplitude of the excited population.
Experimentally, our two dimensional THz time domain spectroscopy set up provided THz pulses centered at 1.5 THz, with enough field amplitude and bandwidth to pick up on the subtle nonlinear effects even as their frequency

was shifted to higher values. In particular, both pump-probe signal displayed clear hallmarks of the expected blue shift: the A pump-B probe and B pump-A probe signals however proved to be markedly different from each other in the details of their time resolved-response, confirming the nonperturbative nature of the interaction. As expected, the strongest blue shift appears on the lowest frequency mode, with minor contribution from higher lying phonons. Furthermore, the presence of a photon echo signal at negative time delays indicates that the driving fields are very long-lived, as expected for a local fields dominated by the polarization response.

The powder sample results in a high degree of inhomogeneity, since the random orientation of the crystallites corresponds to a range of effective fields coupled to the soft mode transition: this can be observed both in the large bandwidth of the pump-probe signal and in the short duration of the photon echo emission. Even though our model calculations do not account for inhomogeneity, they are in overall good agreement with the experimental results.

Aspirin proves to be a very interesting system to explore soft mode nonlinearities, thanks to its highly collective vibrational mode at a very low frequency. Such collective effects characterize many molecular crystals, which present a high oscillator density and complex collective motions involving large portions of their molecular base components. The particular nonlinearity we observed, where long range collective effect dominate the optical response through enhanced dipole-dipole interaction, may be a prominent feature in the low frequency behavior of wide range of molecular crystals.

Summary and outlook

The development of powerful THz sources and ultrafast field resolved detection techniques opened up THz spectroscopy as a vibrant field of research. This frequency range, bridging optics and electronics, hosts many phenomena of interest, such as vibrations and rotations in solid state matter and solutions, field induced tunneling and transport in semiconductors, electronic excitation in low-dimensional nanostructures, soft modes in ferroelectrics and molecular crystals. A coherent multidimensional THz spectroscopy, based on a collinear interaction geometry and a fully field resolved detection scheme, allows to explore the nonlinear response of these disparate systems. A particular focus on nonperturbative interactions affords us the chance to explore highly collective behaviors, strong electronic-vibrational couplings, multiple quantum coherences, nonresonant coherent interactions.

Broadband THz spectroscopy of hydrated DNA

Organic crystals such as DAST, DSTMS and OH1, when pumped at 800 nm, provide a novel octave-spanning THz source [23]. By tailoring the spectral phase of the pump pulse, a very broad spectrum from 0.5 THz to 35 THz can be achieved. The large nonlinear coefficient of these organic materials allows to reach considerable peak field values, as large as 800 kV/cm, even at the relatively moderate pumping energy required to avoid thermal damage to the fragile organic materials. Owing to the extremely large detection bandwidth of our field resolved EOS set-up we are able to exploit this source to the fullest.
This spectral range fully covers the librational band of water, which extends from 10 to 30 THz, peaking at 21 THz. Using OH1 as a source, we performed linear absorption spectroscopy of pure liquid water, water droplets confined in micellar structures and interfacial water bonded to hydrated DNA strands [21]. When water molecules bond with phosphate groups on the DNA backbone instead than to the water hydrogen bond network, sidebands appear at 15 and 25 THz. These can be associated to different bond sites with respectively a

softer or harder potential, as confirmed by measurements on micelles at different hydration levels.

Non-resonant coherent control in GaAs quantum wells

Two-color THz-MIR coherent spectroscopy has been demonstrated on n-doped GaAs quantum wells [28]. Phase matched generation in ZnTe and GaSe crystals provided radiation at 2 THz (30 kV/cm) and 20 THz (up to 50 kV/cm) - the latter resonant to the intersubband transition of the sample - which could be detected in a fully phase resolved fashion in a broadband EOS setup, using an ultrafast 12 fs EOS probe.

The mid-infrared pump beam drove the transition to multiple cycles of Rabi oscillation. The rapidly varying THz electric field induces an Autler-Townes blue shift of the intersubband transition frequency, which results in an accumulated phase shift of the emitted field phase. Furthermore, an overall decrease in total mid-infrared transmission was observed, following the time dependence of the THz field intensity: even though the highly nonresonant THz beam can not directly exchange any energy with the material it can induce mid-infrared absorption. By dynamically deforming the well potential, the THz field inhibits re-emission of energy deposited in the sample by the resonant mid-infrared field - provided that the system is in a high radiative coupling regime.

The nonlinear field phase shift builds up during the absorptive and emittive halves of a Rabi oscillation, reaching its highest value at the switching points: this suggests that coherent control of the switching between absorptive and emittive behavior of mid-infrared devices can be achieved by lossless interaction with intense nonresonant THz pulses.

Nonlinear soft mode response in crystalline aspirin

Molecular crystals, with a large numbers of oscillators closely packed together allowing for a wide range of collective motions, exhibit a high degree of dipole-dipole coupling. As such, their low-frequency excitation have a similar character to the soft modes in ferroelectrics, where large couplings between electronic and vibrational modes leads to a very large polarizability at low frequencies: as the coupling increases, the mode softens to a lower and lower frequency.

Aspirin crystals display a hybrid rotational-electronic mode at 1.1 THz, which not only explains the natural abundance of aspirin crystalline form I, but is also an ideal model system to study soft mode nonlinear response. We probed the hybrid mode in a 2D THz-THz setup, using 2 THz beams generated in GaSe crystals with peak electric fields at 50 kV/cm and 30 kV/cm [27]. The main nonlinear response is characterized by frequency shift of the mode emission fre-

quency.
In this instance, the main component of the local field inside the material is not the external THz field, but more so the long-lived free induction decay of the induced polarization: as the polarization changes, so does the strength of dipole-dipole coupling through the local field, resulting in an instantaneous shift of the transition frequency. For a strong driving field, saturation leads to a blue-shift of the transition frequency, which returns to its original value as the polarization relaxes. In a pump-probe set-up, the complex interaction between strongly blue-shifted and down-chirped electric fields exacerbates the non-impulsive, collective character of the response.
The interaction regime becomes nonperturbative even for moderate external field strengths, as soon as the transition frequency shift becomes larger of the natural line-width resulting in a nonlinear response starkly different from that of e.g. an anharmonic ladder. We observe a signature of the expected frequency shift in both pump-probe signals even at moderate pumping field strengths, confirming the vibrational dipole enhancement by the electronic degrees of freedom. The rephasing photon echo component, appearing at both positive and negative time delays, can only stem from long lived local field driving the interaction. Its highly inhomogeneously broadened line shape points to a wide range of effective field strengths in the crystalline powder sample: since the extent of the instantaneous frequency shift is proportional to the excited polarization, this creates very broad nonlinear signals in frequency space.

In this thesis, the first applications to linear absorption spectroscopy of a novel ultrabroadband source have been presented, opening the possibility of multidimensional broadband THz spectroscopy. A high peak field combined with intense low frequency components is also ideal to study field-induced tunneling in metamaterials: future projects involve the development of broadband 2D spectroscopy to investigate both biological and nanostructured samples.
Our large bandwidth detection made it possible to perform two-color spectroscopy using beams at 2 THz and 20 THz: nonresonant coherent control of intersubband transitions in quantum wells has been demonstrated, paving the way for THz control of devices in the infrared range.
Lastly, intense THz pulses have been used to elicit a nonlinear response of the soft mode in an aspirin molecular crystal, shedding light on a field dependent shift of its frequency. This kind of nonlinearity, which concerns all systems with high degrees of dipole-dipole coupling, could be dominant for molecular crystals at low frequency.

List of publications

The work presented in this thesis is based on the following articles in refereed journals:

- G. Folpini, D. Morrill, C. Somma, K. Reimann, M. Woerner, T. Elsaesser, and K. Biermann, "Nonresonant coherent control: intersubband excitations manipulated by a nonresonant terahertz pulse", *Phys. Rev. B*, **92**, p. 085306, 2015.

- C. Somma, G. Folpini, J. Gupta, K. Reimann, M. Woerner, and T. Elsaesser, "Ultra-broadband terahertz pulses generated in the organic crystal DSTMS", *Opt. Lett.*, **40**, pp. 3404-3407, 2015.

- G. Folpini, K. Reimann, M. Woerner, T. Elsaesser, J. Hoja, and A. Tkatchenko, "Strong local-field enhancement of the nonlinear soft mode response in a molecular crystal", *Phys. Rev. Lett.*, **119**, p.097404, 2017.

- G.Folpini, T. Siebert, M. Woerner, T. Elsaesser, S. Abel and D. Laage, "Water librations in the hydration shell of phospholipids and DNA", *J. Phys. Chem. Lett.* **8**, pp.4492-4497, 2017.

Other peer-reviewed publications:

- C. Somma, G. Folpini, K. Reimann, M. Woerner, and T. Elsaesser, "Twophonon quantum coherences in indium antimonide studied by nonlinear two-dimensional terahertz spectroscopy", *Phys. Rev. Lett.*, **116**, p. 177401, 2016.

- C. Somma, G. Folpini, K. Reimann, M. Woerner, and T. Elsaesser, "Phase-resolved two-dimensional terahertz spectroscopy including off-resonant interactions beyond the $\chi^{(3)}$ limit" *J. Chem. Phys.*, **144**, p. 184202, 2016.

Conference proceedings:

- G. Folpini, D. Morrill, C. Somma, K. Reimann, M. Woerner, T. Elsaesser, and K. Biermann, "Coherent control of intersubband excitations by a nonresonant THz pulse.", Optical Terahertz Science & Technology Conference, San Diego 2015.

- G. Folpini, D. Morrill, C. Somma, K. Reimann, M. Woerner, T. Elsaesser, and K. Biermann, "Coherent control of intersubband transitions measured by two-dimensional THz/MIR spectroscopy.", German THz Conference 2015, Dresden.

- G. Folpini, K. Reimann, M. Woerner, and T. Elsaesser, "Two-Dimensional Terahertz-Spectroscopy on Aspirin.", 8th International Conference on Coherent Multidimensional Spectroscopy, Groningen 2016.

- G. Folpini, K. Reimann, M. Woerner, T. Elsaesser, J. Hoja, and A. Tkatchenko, "Ultrafast two-dimensional THz spectroscopy on aspirin.", Optical Terahertz Science & Technology Conference, London 2017.

List of Figures

List of Tables

Bibliography

[1] K. Reimann, R. P. Smith, A. M. Weiner, T. Elsaesser, and M. Woerner, "Electro-optic sampling of THz transients with MV/cm amplitudes," in *Trends in Optics and Photonics Vol. 89, Conference on Lasers and Electro-Optics, Baltimore 2003, Technical Digest*, (Washington DC), pp. 132–133, Optical Society of America, 2003.

[2] M. C. Hoffmann and J. A. Fülöp, "Intense ultrashort terahertz pulses: generation and applications," *J. Phys. D*, vol. 44, p. 083001, 2011.

[3] C. Vicario, M. Jazbinsek, A. Ovchinnikov, O. Chefonov, S. Ashitkov, M. Agranat, and C. Hauri, "High efficiency thz generation in dstms, dast and oh1 pumped by cr: forsterite laser," *Optics express*, vol. 23, no. 4, pp. 4573–4580, 2015.

[4] Q. Wu and X.-C. Zhang, "Free-space electro-optic sampling of terahertz beams," *Appl. Phys. Lett.*, vol. 67, pp. 3523–3525, 1995.

[5] C. A. Schmuttenmaer, "Exploring dynamics in the far-infrared with terahertz spectroscopy," *Chem. Rev.*, vol. 104, pp. 1759–1780, 2004.

[6] T. Kampfrath, K. Tanaka, and K. A. Nelson, "Resonant and nonresonant control over matter and light by intense terahertz transients," *Nature Photon.*, vol. 7, pp. 680–690, 2013.

[7] M. Woerner, K. Reimann, and T. Elsaesser, "Multidimensional Terahertz Spectroscopy," in *Encyclopedia of Modern Optics*, Elsevier, 2017.

[8] C. Somma, K. Reimann, C. Flytzanis, T. Elsaesser, and M. Woerner, "High-field terahertz bulk photovoltaic effect in lithium niobate," *Phys. Rev. Lett.*, vol. 112, p. 146602, 2014.

[9] J. D. Cruzan, M. R. Viant, M. G. Brown, and R. J. Saykally, "Terahertz laser vibration- rotation tunneling spectroscopy of the water tetramer," *The Journal of Physical Chemistry A*, vol. 101, no. 48, pp. 9022–9031, 1997.

[10] J. Savolainen, S. Ahmed, and P. Hamm, "Two-dimensional Raman-terahertz spectroscopy of water," *Proc. Natl. Acad. Sci. USA*, vol. 110, pp. 20402–20407, 2013.

[11] P. Gaal, W. Kuehn, K. Reimann, M. Woerner, T. Elsaesser, and R. Hey, "Internal motions of a quasiparticle governing its ultrafast nonlinear response," *Nature*, vol. 450, pp. 1210–1213, 2007.

[12] W. Kuehn, P. Gaal, K. Reimann, M. Woerner, T. Elsaesser, and R. Hey, "Coherent ballistic motion of electrons in a periodic potential," *Phys. Rev. Lett.*, vol. 104, p. 146602, 2010.

[13] F. Junginger, B. Mayer, C. Schmidt, O. Schubert, S. Mährlein, A. Leitenstorfer, R. Huber, and A. Pashkin, "Nonperturbative interband response of a bulk InSb semiconductor driven off resonantly by terahertz electromagnetic few-cycle pulses," *Phys. Rev. Lett.*, vol. 109, p. 147403, 2012.

[14] K. Shinokita, K. Reimann, M. Woerner, T. Elsaesser, R. Hey, and C. Flytzanis, "Strong amplification of coherent acoustic phonons by intraminiband currents in a semiconductor superlattice," *Phys. Rev. Lett.*, vol. 116, p. 075504, 2016.

[15] C. W. Luo, K. Reimann, M. Woerner, T. Elsaesser, R. Hey, and K. H. Ploog, "Phase-resolved nonlinear response of a two-dimensional electron gas under femtosecond intersubband excitation," *Phys. Rev. Lett.*, vol. 92, p. 047402, 2004.

[16] T. Shih, K. Reimann, M. Woerner, T. Elsaesser, I. Waldmüller, A. Knorr, R. Hey, and K. H. Ploog, "Nonlinear response of radiatively coupled intersubband transitions of quasi–two-dimensional electrons," *Phys. Rev. B*, vol. 72, p. 195338, 2005.

[17] W. Kuehn, K. Reimann, M. Woerner, T. Elsaesser, R. Hey, and U. Schade, "Strong correlation of electronic and lattice excitations in GaAs/AlGaAs semiconductor quantum wells revealed by two-dimensional terahertz spectroscopy," *Phys. Rev. Lett.*, vol. 107, p. 067401, 2011.

[18] G. Günter, A. A. Anappara, J. Hees, A. Sell, G. Biasiol, L. Sorba, S. De Liberato, C. Ciuti, A. Tredicucci, A. Leitenstorfer, *et al.*, "Sub-cycle switch-on of ultrastrong light-matter interaction," *Nature*, vol. 458, no. 7235, p. 178, 2009.

[19] J. Keller, C. Maissen, J. Haase, G. L. Paravicini-Bagliani, F. Valmorra, J. Palomo, J. Mangeney, J. Tignon, S. S. Dhillon, G. Scalari, *et al.*, "Coupling surface plasmon polariton modes to complementary thz metasurfaces tuned by inter meta-atom distance," *Advanced Optical Materials*, vol. 5, no. 6, 2017.

[20] C. Somma, G. Folpini, J. Gupta, K. Reimann, M. Woerner, and T. Elsaesser, "Ultra-broadband terahertz pulses generated in the organic crystal DSTMS," *Opt. Lett.*, vol. 40, pp. 3404–3407, 2015.

[21] G. Folpini, T. Siebert, M. Woerner, S. Abel, D. Laage, and T. Elsaesser, "Water librations in the hydration shell of phospholipids," *The Journal of Physical Chemistry Letters*, vol. 8, no. 18, pp. 4492–4497, 2017.

[22] W. Kuehn, K. Reimann, M. Woerner, and T. Elsaesser, "Phase-resolved two-dimensional spectroscopy based on collinear n-wave mixing in the ultrafast time domain," *J. Chem. Phys.*, vol. 130, p. 164503, 2009.

[23] C. Somma, G. Folpini, K. Reimann, M. Woerner, and T. Elsaesser, "Phase-resolved two-dimensional terahertz spectroscopy including off-resonant interactions beyond the $\chi^{(3)}$ limit," *J. Chem. Phys.*, vol. 144, p. 184202, 2016.

[24] C. Somma, G. Folpini, K. Reimann, M. Woerner, and T. Elsaesser, "Two-phonon quantum coherences in indium antimonide studied by nonlinear two-dimensional terahertz spectroscopy," *Phys. Rev. Lett.*, vol. 116, p. 177401, 2016.

[25] W. Kuehn, P. Gaal, K. Reimann, M. Woerner, T. Elsaesser, and R. Hey, "THz-induced interband tunneling of electrons in GaAs," *Phys. Rev. B*, vol. 82, p. 075204, 2010.

[26] W. H. Zurek, "Decoherence and the transition from quantum to classical—revisited," *Los Alamos Science*, vol. 27, pp. 86–109, 2002.

[27] G. Folpini, K. Reimann, M. Woerner, T. Elsaesser, J. Hoja, and A. Tkatchenko, "Strong local-field enhancement of the nonlinear soft-mode response in a molecular crystal," *Physical review letters*, vol. 119, no. 9, p. 097404, 2017.

[28] G. Folpini, D. Morrill, C. Somma, K. Reimann, M. Woerner, T. Elsaesser, and K. Biermann, "Nonresonant coherent control—intersubband excitations manipulated by a nonresonant terahertz pulse," *Phys. Rev. B*, vol. 92, p. 085306, 2015.

[29] D. H. Auston, K. P. Cheung, and P. R. Smith, "Picosecond photoconducting Hertzian dipoles," *Appl. Phys. Lett.*, vol. 45, pp. 284–286, 1984.

[30] P. U. Jepsen, D. G. Cooke, and M. Koch, "Terahertz spectroscopy and imaging–modern techniques and applications," *Laser & Photonics Reviews*, vol. 5, no. 1, pp. 124–166, 2011.

[31] B. Sartorius, H. Roehle, H. Künzel, J. Böttcher, M. Schlak, D. Stanze, H. Venghaus, and M. Schell, "All-fiber terahertz time-domain spectrometer operating at 1.5 μm telecom wavelengths," *Optics Express*, vol. 16, no. 13, pp. 9565–9570, 2008.

[32] C. H. Bates, W. B. White, and R. Roy, "New high-pressure polymorph of zinc oxide," *Science*, vol. 137, p. 993, 1962.

[33] I. Wilke and S. Sengupta, "Nonlinear optical techniques for terahertz pulse generation and detection—Optical rectification and electrooptic sampling," in *Terahertz Spectroscopy: Principles and Applications* (S. L. Dexheimer, ed.), (Boca Raton), pp. 41–72, CRC Press, 2007.

[34] A. Sell, A. Leitenstorfer, and R. Huber, "Phase-locked generation and field-resolved detection of widely tunable terahertz pulses with amplitudes exceeding 100 MV/cm," *Opt. Lett.*, vol. 33, pp. 2767–2769, 2008.

[35] K. Reimann, R. P. Smith, A. M. Weiner, T. Elsaesser, and M. Woerner, "Direct field-resolved detection of terahertz transients with amplitudes of megavolts per centimeter," *Opt. Lett.*, vol. 28, pp. 471–473, 2003.

[36] M. Shalaby and C. P. Hauri, "Demonstration of a low-frequency three-dimensional terahertz bullet with extreme brightness," *Nature communications*, vol. 6, 2015.

[37] J.-H. Jeong, B.-J. Kang, J.-S. Kim, M. Jazbinsek, S.-H. Lee, S.-C. Lee, I.-H. Baek, H. Yun, J. Kim, Y. S. Lee, *et al.*, "High-power broadband organic thz generator," *Scientific reports*, vol. 3, p. 3200, 2013.

[38] M. Shalaby, C. Vicario, K. Thirupugalmani, S. Brahadeeswaran, and C. P. Hauri, "Intense THz source based on BNA organic crystal pumped at Ti:sapphire wavelength," *Opt. Lett.*, vol. 41, pp. 1777–1780, 2016.

[39] J. Hebling, G. Almasi, I. Z. Kozma, and J. Kuhl, "Velocity matching by pulse front tilting for large-area thz-pulse generation," *Optics Express*, vol. 10, no. 21, pp. 1161–1166, 2002.

[40] J. Hebling, K.-L. Yeh, M. C. Hoffmann, B. Bartal, and K. A. Nelson, "Generation of high-power terahertz pulses by tilted-pulse-front excitation and their application possibilities," *J. Opt. Soc. Am. B*, vol. 25, pp. B6–B19, 2008.

[41] J. A. Fülöp, Z. Ollmann, C. Lombosi, C. Skrobol, S. Klingebiel, L. Pálfalvi, F. Krausz, S. Karsch, and J. Hebling, "Efficient generation of thz pulses with 0.4 mj energy," *Optics express*, vol. 22, no. 17, pp. 20155–20163, 2014.

[42] M. D. Thomson, M. Kreß, T. Löffler, and H. G. Roskos, "Broadband THz emission from gas plasmas induced by femtosecond optical pulses: From fundamentals to applications," *Laser & Photon. Rev.*, vol. 1, pp. 349–368, 2007.

[43] D. J. Cook and R. M. Hochstrasser, "Intense terahertz pulses by four-wave rectification in air," *Opt. Lett.*, vol. 25, pp. 1210–1212, 2000.

[44] I. Babushkin, W. Kuehn, C. Köhler, S. Skupin, L. Bergé, K. Reimann, M. Woerner, J. Herrmann, and T. Elsaesser, "Ultrafast spatio-temporal dynamics of terahertz generation by ionizing two-color femtosecond pulses in gases," *Phys. Rev. Lett.*, vol. 105, p. 053903, 2010.

[45] T. Bartel, P. Gaal, K. Reimann, M. Woerner, and T. Elsaesser, "Generation of single-cycle THz transients with high electric-field amplitudes," *Opt. Lett.*, vol. 30, pp. 2805–2807, 2005.

[46] C. Sirtori, S. Dhillon, C. Faugeras, A. Vasanelli, and X. Marcadet, "Quantum cascade lasers: The semiconductor solution for lasers in the mid- and far-infrared spectral regions," *Phys. Status Solidi A*, vol. 203, pp. 3533–3537, 2006.

[47] M. S. Vitiello, G. Scalari, B. Williams, and P. De Natale, "Quantum cascade lasers: 20 years of challenges," *Opt. Express*, vol. 23, pp. 5167–5182, 2015.

[48] Y. Bai, N. Bandyopadhyay, S. Tsao, S. Slivken, and M. Razeghi, "Room temperature quantum cascade lasers with 27% wall plug efficiency," *Applied Physics Letters*, vol. 98, no. 18, p. 181102, 2011.

[49] Y. Liu, A. Houard, B. Prade, S. Akturk, A. Mysyrowicz, and V. T. Tikhonchuk, "Terahertz radiation source in air based on bifilamentation of femtosecond laser pulses," *Phys. Rev. Lett.*, vol. 99, p. 135002, 2007.

[50] L. Li, L. Chen, J. Zhu, J. Freeman, P. Dean, A. Valavanis, A. Davies, and E. Linfield, "Terahertz quantum cascade lasers with¿ 1 w output powers," *Electronics Letters*, vol. 50, no. 4, pp. 309–311, 2014.

[51] M. Rösch, G. Scalari, M. Beck, and J. Faist, "Octave-spanning semiconductor laser," *Nature Photonics*, vol. 9, no. 1, pp. 42–47, 2015.

[52] F. Wang, K. Maussang, S. Moumdji, R. Colombelli, J. R. Freeman, I. Kundu, L. Li, E. H. Linfield, A. G. Davies, J. Mangeney, *et al.*, "Generating ultrafast pulses of light from quantum cascade lasers," *Optica*, vol. 2, no. 11, pp. 944–949, 2015.

[53] H.-T. Chen, W. J. Padilla, J. M. O. Zide, A. C. Gossard, A. J. Taylor, and R. D. Averitt, "Active terahertz metamaterial devices," *Nature*, vol. 444, pp. 597–600, 2006.

[54] H. Tao, W. J. Padilla, X. Zhang, and R. D. Averitt, "Recent progress in electromagnetic metamaterial devices for terahertz applications," *IEEE Journal of Selected Topics in Quantum Electronics*, vol. 17, pp. 92–101, Jan 2011.

[55] F. Zhou, Y. Bao, W. Cao, C. T. Stuart, J. Gu, W. Zhang, and C. Sun, "Hiding a realistic object using a broadband terahertz invisibility cloak," *Scientific reports*, vol. 1, 2011.

[56] G. Scalari, C. Maissen, D. Turčinková, D. Hagenmüller, S. De Liberato, C. Ciuti, C. Reichl, D. Schuh, W. Wegscheider, M. Beck, *et al.*, "Ultrastrong coupling of the cyclotron transition of a 2d electron gas to a thz metamaterial," *Science*, vol. 335, no. 6074, pp. 1323–1326, 2012.

[57] H. Y. Hwang, S. Fleischer, N. C. Brandt, B. G. P. Jr., M. Liu, K. Fan, A. Sternbach, X. Zhang, R. D. Averitt, and K. A. Nelson, "A review of non-linear terahertz spectroscopy with ultrashort tabletop-laser pulses," *J. Mod. Opt.*, vol. 62, pp. 1447–1479, 2015.

[58] I. Wilke, A. M. MacLeod, W. Gillespie, G. Berden, G. Knippels, and A. Van Der Meer, "Single-shot electron-beam bunch length measurements," *Physical review letters*, vol. 88, no. 12, p. 124801, 2002.

[59] G. L. Carr, M. C. Martin, W. R. McKinney, K. Jordan, G. R. Neil, and G. P. Williams, "High-power terahertz radiation from relativistic electrons," *Nature*, vol. 420, pp. 153–156, 2002.

[60] G. Gallerano, S. Biedron, *et al.*, "Overview of terahertz radiation sources," in *Proceedings of the 2004 FEL Conference*, no. 1, pp. 216–221, 2004.

[61] O. Schubert, M. Hohenleutner, F. Langer, B. Urbanek, C. Lange, U. Huttner, D. Golde, T. Meier, M. Kira, S. W.

Koch, and R. Huber, "Sub-cycle control of terahertz high-harmonic generation by dynamical Bloch oscillations," *Nature Photon.*, vol. 8, pp. 119–123, 2014.

[62] F. Langer, M. Hohenleutner, U. Huttner, S. Koch, M. Kira, and R. Huber, "Symmetry-controlled temporal structure of high-harmonic carrier fields from a bulk crystal," *Nature Photonics*, vol. 11, no. 4, pp. 227–231, 2017.

[63] P. Richards, "Bolometers for infrared and millimeter waves," *Journal of Applied Physics*, vol. 76, no. 1, pp. 1–24, 1994.

[64] S. Kono, M. Tani, and K. Sakai, "Ultrabroadband photoconductive detection: Comparison with free-space electro-optic sampling," *Appl. Phys. Lett.*, vol. 79, pp. 898–900, 2001.

[65] M. Ashida, "Ultra-broadband terahertz wave detection using photoconductive antenna," *Japanese Journal of Applied Physics*, vol. 47, no. 10S, p. 8221, 2008.

[66] F. R. Giorgetta, E. Baumann, M. Graf, Q. Y. C. Manz, K. Kohler, H. E. Beere, D. A. Ritchie, E. Linfield, A. G. Davies, Y. Fedoryshyn, H. Jackel, M. Fischer, J. Faist, and D. Hofstetter, "Quantum cascade detectors," *IEEE J. Quantum Electron.*, vol. 45, pp. 1039–1052, 2009.

[67] N. Karpowicz, J. Dai, X. Lu, Y. Chen, M. Yamaguchi, H. Zhao, X.-C. Zhang, L. Zhang, C. Zhang, M. Price-Gallagher, *et al.*, "Coherent heterodyne time-domain spectrometry covering the entire "terahertz gap"," *Applied Physics Letters*, vol. 92, no. 1, p. 011131, 2008.

[68] D. Auston and P. Smith, "Generation and detection of millimeter waves by picosecond photoconductivity," *Applied Physics Letters*, vol. 43, no. 7, pp. 631–633, 1983.

[69] F. Pockels, *Lehrbuch der Kristalloptik*. Leipzig: Teubner, 2006.

[70] R. W. Boyd, "Chapter 11 - the electrooptic and photorefractive effects," in *Nonlinear Optics (Third Edition)* (R. W. Boyd, ed.), pp. 511 – 541, Burlington: Academic Press, third edition ed., 2008.

[71] Q. Wu and X.-C. Zhang, "7 terahertz broadband GaP electro-optic sensor," *Appl. Phys. Lett.*, vol. 70, pp. 1784–1786, 1997.

[72] A. Leitenstorfer, S. Hunsche, J. Shah, M. C. Nuss, and W. H. Knox, "Detectors and sources for ultrabroadband electro-optic sampling: Experiment and theory," *Appl. Phys. Lett.*, vol. 74, pp. 1516–1518, 1999.

[73] Q. Wu and X.-C. Zhang, "Ultrafast electro-optic field sensors," *Appl. Phys. Lett.*, vol. 68, pp. 1604–1606, 1996.

[74] N. C. Van der Valk, W. A. van der Marel, and P. C. Planken, "Terahertz polarization imaging," *Optics letters*, vol. 30, no. 20, pp. 2802–2804, 2005.

[75] M. Bass, P. A. Franken, J. F. Ward, and G. Weinreich, "Optical rectification," *Phys. Rev. Lett.*, vol. 9, pp. 446–448, 1962.

[76] J. Hebling, A. Stepanov, G. Almási, B. Bartal, and J. Kuhl, "Tunable thz pulse generation by optical rectification of ultrashort laser pulses with tilted pulse fronts," *Applied Physics B: Lasers and Optics*, vol. 78, no. 5, pp. 593–599, 2004.

[77] J. Fülöp, G. Polónyi, B. Monoszlai, G. Andriukaitis, T. Balciunas, A. Pugzlys, G. Arthur, A. Baltuska, and J. Hebling, "Highly efficient scalable monolithic semiconductor terahertz pulse source," *Optica*, vol. 3, no. 10, pp. 1075–1078, 2016.

[78] K. L. Vodopyanov and V. G. Voevodin, "2.8 μm laser pumped type I and type II travelling-wave optical parametric generator in GaSe," *Opt. Commun.*, vol. 114, pp. 333–335, 1995.

[79] R. A. Kaindl, M. Wurm, K. Reimann, P. Hamm, A. M. Weiner, and M. Woerner, "Generation, shaping, and characterization

of intense femtosecond pulses tunable between 3 and 20 μm," *J. Opt. Soc. Am. B*, vol. 17, pp. 2086–2094, 2000.

[80] K. R. Allakhverdiev, M. Ö. Yetis, S. Özbek, T. K. Baykara, and E. Y. Salaev, "Effective nonlinear GaSe crystal. Optical properties and applications," *Laser Phys.*, vol. 19, pp. 1092–1104, 2009.

[81] P. Tournois, "Acousto-optic programmable dispersive filter for adaptive compensation of group delay time dispersion in laser systems," *Optics communications*, vol. 140, no. 4-6, pp. 245–249, 1997.

[82] S. R. Marder, J. W. Perry, and W. P. Schaefer, "Synthesis of organic salts with large second-order optical nonlinearities," *Science*, vol. 245, pp. 626–628, 1989.

[83] P.-J. Kim, M. Jazbinsek, and O.-P. Kwon, "Selective growth of highly efficient electrooptic stilbazolium crystals by sequential crystal growth in different solvents," *Crystal Growth & Design*, vol. 11, pp. 3060–3064, 2011.

[84] F. Pan, M. S. Wong, C. Bosshard, and P. Günter, "Crystal growth and characterization of the organic salt 4-N,N-dimethylamino-4'-N-methyl-stilbazolium tosylate (DAST)," *Adv. Mater.*, vol. 8, pp. 592–595, 1996.

[85] L. Mutter, F. D. J. Brunner, Z. Yang, M. Jazbinšek, and P. Günter, "Linear and nonlinear optical properties of the organic crystal DSTMS," *J. Opt. Soc. Am. B*, vol. 24, pp. 2556–2561, 2007.

[86] M. Stillhart, A. Schneider, and P. Günter, "Optical properties of 4-N,N-dimethylamino-4'-N'-methyl-stilbazolium 2,4,6-trimethylbenzenesulfonate crystals at terahertz frequencies," *J. Opt. Soc. Am. B*, vol. 25, pp. 1914–1919, 2008.

[87] P. D. Cunningham and L. M. Hayden, "Optical properties of DAST in the THz range," *Opt. Express*, vol. 18, pp. 23620–23625, 2010.

[88] A. Schneider, M. Stillhart, and P. Günter, "High efficiency generation and detection of terahertz pulses using laser pulses at telecommunication wavelengths," *Opt. Express*, vol. 14, pp. 5376–5384, 2006.

[89] P. Liu, D. Xu, Y. Li, X. Zhang, Y. Wang, J. Yao, and Y. Wu, "Widely tunable and monochromatic terahertz difference frequency generation with organic crystal DSTMS," *Europhys. Lett.*, vol. 106, p. 60001, 2014.

[90] C. Vicario, B. Monoszlai, and C. P. Hauri, "GV/m single-cycle terahertz fields from a laser-driven large-size partitioned organic crystal," *Phys. Rev. Lett.*, vol. 112, p. 213901, 2014.

[91] T. Kolev, Z. Glavcheva, D. Yancheva, M. Schuermann, D.-C. Kleb, H. Preut, and P. Bleckmann, "2-{3-[2-(4-Hydroxyphenyl) vinyl]-5, 5-dimethylcyclohex-2-en-1-ylidene} malononitrile," *Acta Crystallographica Section E: Structure Reports Online*, vol. 57, no. 6, pp. o561–o562, 2001.

[92] O.-P. Kwon, S.-J. Kwon, M. Jazbinsek, F. D. Brunner, J.-I. Seo, C. Hunziker, A. Schneider, H. Yun, Y.-S. Lee, and P. Günter, "Organic phenolic configurationally locked polyene single crystals for electro-optic and terahertz wave applications," *Advanced Functional Materials*, vol. 18, no. 20, pp. 3242–3250, 2008.

[93] C. Hunziker, S.-J. Kwon, H. Figi, F. Juvalta, O.-P. Kwon, M. Jazbinsek, and P. Günter, "Configurationally locked, phenolic polyene organic crystal 2-{3-(4-hydroxystyryl)-5, 5-dimethylcyclohex-2-enylidene} malononitrile: linear and nonlinear optical properties," *JOSA B*, vol. 25, no. 10, pp. 1678–1683, 2008.

[94] P. Y. Han, M. Tani, F. Pan, and X.-C. Zhang, "Use of the organic crystal DAST for terahertz beam applications," *Opt. Lett.*, vol. 25, pp. 675–677, 2000.

[95] D. Laage, T. Elsaesser, and J. T. Hynes, "Water dynamics in the hydration shells of biomolecules," *Chemical Reviews*, 2017.

[96] J. E. Bertie and Z. Lan, "Infrared intensities of liquids xx: The intensity of the oh stretching band of liquid water revisited, and the best current values of the optical constants of h2o(l) at 25°c between 15,000 and 1 cm−1," *Applied Spectroscopy*, vol. 50, no. 8, pp. 1047–1057, 1996.

[97] H. R. Zelsmann, "Temperature dependence of the optical constants for liquid H_2O and D_2O in the far IR region," *J. Mol. Struct.*, vol. 350, pp. 95–114, 1995.

[98] S. Ashihara, N. Huse, A. Espagne, E. T. J. Nibbering, and T. Elsaesser, "Ultrafast structural dynamics of water induced by dissipation of vibrational energy," *The Journal of Physical Chemistry A*, vol. 111, no. 5, pp. 743–746, 2007.

[99] H. D. Downing and D. Williams, "Optical constants of water in the infrared," *Journal of Geophysical Research*, vol. 80, no. 12, pp. 1656–1661, 1975.

[100] V. Kubarev, "Optical properties of cvd-diamond in terahertz and infrared ranges," *Nuclear Instruments and Methods in Physics Research Section A: Accelerators, Spectrometers, Detectors and Associated Equipment*, vol. 603, no. 1–2, pp. 22 – 24, 2009. Proceedings of the {XVII} International Synchrotron Radiation ConferenceSR-2008.

[101] N. E. Levinger, "Water in confinement," *Science*, vol. 298, no. 5599, pp. 1722–1723, 2002.

[102] D. E. Rosenfeld and C. A. Schmuttenmaer, "Dynamics of the water hydrogen bond network at ionic, nonionic, and hy-

drophobic interfaces in nanopores and reverse micelles," *The Journal of Physical Chemistry B*, vol. 115, no. 5, pp. 1021–1031, 2011.

[103] D. S. Venables, K. Huang, and C. A. Schmuttenmaer, "Effect of reverse micelle size on the librational band of confined water and methanol," *The Journal of Physical Chemistry B*, vol. 105, no. 38, pp. 9132–9138, 2001.

[104] D. E. Rosenfeld and C. A. Schmuttenmaer, "Dynamics of water confined within reverse micelles," *The Journal of Physical Chemistry B*, vol. 110, no. 29, pp. 14304–14312, 2006.

[105] R. Costard, N. E. Levinger, E. T. J. Nibbering, and T. Elsaesser, "Ultrafast vibrational dynamics of water confined in phospholipid reverse micelles," *The Journal of Physical Chemistry B*, vol. 116, no. 19, pp. 5752–5759, 2012.

[106] R. Costard, I. A. Heisler, and T. Elsaesser, "Structural dynamics of hydrated phospholipid surfaces probed by ultrafast 2d spectroscopy of phosphate vibrations," *The journal of physical chemistry letters*, vol. 5, no. 3, pp. 506–511, 2014.

[107] S. Abel, N. Galamba, E. Karakas, M. Marchi, W. H. Thompson, and D. Laage, "on the structural and dynamical properties of dopc reverse micelles," *langmuir*, vol. 32, no. 41, pp. 10610–10620, 2016.

[108] N. E. Levinger, R. Costard, E. T. Nibbering, and T. Elsaesser, "Ultrafast energy migration pathways in self-assembled phospholipids interacting with confined water," *The Journal of Physical Chemistry A*, vol. 115, no. 43, pp. 11952–11959, 2011.

[109] B. Guillot, "A molecular dynamics study of the far infrared spectrum of liquid water," *The Journal of chemical physics*, vol. 95, no. 3, pp. 1543–1551, 1991.

[110] J. M. Vargason, K. Henderson, and P. S. Ho, "A crystallographic map of the transition from b-dna to a-dna," *Proceedings of the National Academy of Sciences*, vol. 98, no. 13, pp. 7265–7270, 2001.

[111] Ł. Szyc, M. Yang, E. T. Nibbering, and T. Elsaesser, "Ultrafast vibrational dynamics and local interactions of hydrated dna," *Angewandte Chemie International Edition*, vol. 49, no. 21, pp. 3598–3610, 2010.

[112] T. Siebert, B. Guchhait, Y. Liu, R. Costard, and T. Elsaesser, "Anharmonic backbone vibrations in ultrafast processes at the DNA-water interface," *J. Phys. Chem. B*, vol. 119, pp. 9670–9677, 2015.

[113] N. Laman, S. S. Harsha, D. Grischkowsky, and J. S. Melinger, "High-resolution waveguide {THz} spectroscopy of biological molecules," *Biophysical Journal*, vol. 94, no. 3, pp. 1010 – 1020, 2008.

[114] B. Fischer, M. Walther, and P. U. Jepsen, "Far-infrared vibrational modes of dna components studied by terahertz time-domain spectroscopy," *Physics in medicine and biology*, vol. 47, no. 21, p. 3807, 2002.

[115] A. Markelz, A. Roitberg, and E. J. Heilweil, "Pulsed terahertz spectroscopy of dna, bovine serum albumin and collagen between 0.1 and 2.0 thz," *Chemical Physics Letters*, vol. 320, no. 1, pp. 42–48, 2000.

[116] E. Duboué-Dijon, A. C. Fogarty, J. T. Hynes, and D. Laage, "Dynamical disorder in the dna hydration shell," *Journal of the American Chemical Society*, vol. 138, no. 24, pp. 7610–7620, 2016.

[117] W. Aue, E. Bartholdi, and R. R. Ernst, "Two-dimensional spectroscopy. application to nuclear magnetic resonance," *The*

Journal of Chemical Physics, vol. 64, no. 5, pp. 2229–2246, 1976.

[118] R. R. Ernst, G. Bodenhausen, and A. Wokaun, *Principles of Nuclear Magnetic Resonance in One and Two Dimensions*. Oxford: Oxford University Press, 1987.

[119] P. Hamm, M. Lim, and R. M. Hochstrasser, "Vibrational energy relaxation of the cyanide ion in water," *J. Chem. Phys.*, vol. 107, pp. 10523–10531, 1997.

[120] S. Mukamel, "Multidimensional femtosecond correlation spectroscopies of electronic and vibrational excitations," *Annu. Rev. Phys. Chem.*, vol. 51, pp. 691–729, 2000.

[121] J. D. Hybl, A. W. Albrecht, S. M. Gallagher Faeder, and D. M. Jonas, "Two-dimensional electronic spectroscopy," *Chem. Phys. Lett.*, vol. 297, pp. 307–313, 1998.

[122] D. Grischkowsky, S. Keiding, M. van Exter, and C. Fattinger, "Far-infrared time-domain spectroscopy with terahertz beams of dielectrics and semiconductors," *J. Opt. Soc. Am. B*, vol. 7, pp. 2006–2015, 1990.

[123] P. Hamm and A. Shalit, "Perspective: Echoes in 2d-raman-thz spectroscopy," *The Journal of Chemical Physics*, vol. 146, no. 13, p. 130901, 2017.

[124] M. Kozina, M. Pancaldi, C. Bernhard, T. van Driel, J. M. Glownia, P. Marsik, M. Radovic, C. A. Vaz, D. Zhu, S. Bonetti, *et al.*, "Local terahertz field enhancement for time-resolved x-ray diffraction," *Applied Physics Letters*, vol. 110, no. 8, p. 081106, 2017.

[125] J. Weisshaupt, A. Rouzée, M. Woerner, M. J. J. Vrakking, T. Elsaesser, E. L. Shirley, and A. Borgschulte, "Ultrafast modulation of electronic structure by coherent phonon excitations," *Phys. Rev. B*, vol. 95, p. 081101, Feb 2017.

[126] W. Kuehn, K. Reimann, M. Woerner, T. Elsaesser, and R. Hey, "Two-dimensional terahertz correlation spectra of electronic excitations in semiconductor quantum wells," *J. Phys. Chem. B*, vol. 115, pp. 5448–5455, 2011.

[127] S. Mukamel, *Principles of nonlinear optical spectroscopy*. Oxford series in optical and imaging sciences, Oxford University Press, 1995.

[128] R. P. Feynman, "Space-time approach to quantum electrodynamics," *Physical Review*, vol. 76, no. 6, p. 769, 1949.

[129] T. K. Yee and T. K. Gustafson, "Diagrammatic analysis of the density operator for nonlinear optical calculations: Pulsed and cw responses," *Phys. Rev. A*, vol. 18, pp. 1597–1617, 1978.

[130] W. T. Pollard, S.-Y. Lee, and R. A. Mathies, "Wave packet theory of dynamic absorption spectra in femtosecond pump–probe experiments," *J. Chem. Phys.*, vol. 92, pp. 4012–4029, 1990.

[131] P. Hamm and M. Zanni, *Concepts and Methods of 2D Infrared Spectroscopy*. Cambridge: Cambridge University Press, 2011.

[132] X. Li, T. Zhang, C. N. Borca, and S. T. Cundiff, "Many-body interactions in semiconductors probed by optical two-dimensional Fourier transform spectroscopy," *Phys. Rev. Lett.*, vol. 96, p. 057406, 2006.

[133] K. W. Stone, K. Gundogdu, D. B. Turner, X. Li, S. T. Cundiff, and K. A. Nelson, "Two-quantum 2D FT electronic spectroscopy of biexcitons in GaAs quantum wells," *Science*, vol. 324, pp. 1169–1173, 2009.

[134] R. D. Mehlenbacher, T. J. McDonough, M. Grechko, M.-Y. Wu, M. S. Arnold, and M. T. Zanni, "Energy transfer pathways in semiconducting carbon nanotubes revealed using

two-dimensional white-light spectroscopy," *Nature communications*, vol. 6, p. 6732, 2015.

[135] C. J. Fecko, J. D. Eaves, J. J. Loparo, A. Tokmakoff, and P. L. Geissler, "Ultrafast hydrogen-bond dynamics in the infrared spectroscopy of water," *Science*, vol. 301, pp. 1698–1702, 2003.

[136] E. T. J. Nibbering and T. Elsaesser, "Ultrafast vibrational dynamics of hydrogen bonds in the condensed phase," *Chem. Rev.*, vol. 104, pp. 1887–1914, 2004.

[137] T. Brixner, J. Stenger, H. M. Vaswani, M. Cho, R. E. Blankenship, and G. R. Fleming, "Two-dimensional spectroscopy of electronic couplings in photosynthesis," *Nature*, vol. 434, pp. 625–628, 2005.

[138] A. Ghosh, J. S. Ostrander, and M. T. Zanni, "Watching proteins wiggle: Mapping structures with two-dimensional infrared spectroscopy," *Chemical Reviews*, 2017.

[139] V. Cervetto, J. Helbing, J. Bredenbeck, and P. Hamm, "Double-resonance versus pulsed Fourier transform two-dimensional infrared spectroscopy: An experimental and theoretical comparison," *J. Chem. Phys.*, vol. 121, pp. 5935–5942, 2004.

[140] W. P. de Boeij, M. S. Pshenichnikov, and D. A. Wiersma, "Heterodyne-detected stimulated photon echo: applications to optical dynamics in solution," *Chemical Physics*, vol. 233, no. 2, pp. 287 – 309, 1998.

[141] J. C. Vaughan, T. Hornung, K. W. Stone, and K. A. Nelson, "Coherently controlled ultrafast four-wave mixing spectroscopy," *The Journal of Physical Chemistry A*, vol. 111, no. 23, pp. 4873–4883, 2007.

[142] P. Tian, D. Keusters, Y. Suzaki, and W. S. Warren, "Femtosecond phase-coherent two-dimensional spectroscopy," *Science*, vol. 300, pp. 1553–1555, 2003.

[143] W. Xiong and M. T. Zanni, "Signal enhancement and background cancellation in collinear two-dimensional spectroscopies," *Opt. Lett.*, vol. 33, pp. 1371–1373, 2008.

[144] M. Khalil, N. Demirdöven, and A. Tokmakoff, "Obtaining absorptive line shapes in two-dimensional infrared vibrational correlation spectra," *Physical review letters*, vol. 90, no. 4, p. 047401, 2003.

[145] M. Khalil, N. Demirdöven, and A. Tokmakoff, "Coherent 2D IR spectroscopy: Molecular structure and dynamics in solution," *J. Phys. Chem. A*, vol. 107, pp. 5258–5279, 2003.

[146] M. Woerner, W. Kuehn, P. Bowlan, K. Reimann, and T. Elsaesser, "Ultrafast two-dimensional terahertz spectroscopy of elementary excitations in solids," *New J. Phys.*, vol. 15, p. 025039, 2013.

[147] G. Folpini, D. Morrill, C. Somma, K. Reimann, M. Woerner, T. Elsaesser, and K. Biermann, "Coherent control of intersubband excitations by a nonresonant THz pulse." Optical Terahertz Science & Technology Conference, San Diego 2015.

[148] P. Bowlan, E. Martinez-Moreno, K. Reimann, T. Elsaesser, and M. Woerner, "Ultrafast terahertz response of multilayer graphene in the nonperturbative regime," *Phys. Rev. B*, vol. 89, p. 041408(R), 2014.

[149] D. Strickland and G. Mourou, "Compression of amplified chirped optical pulses," *Optics Communications*, vol. 55, no. 6, pp. 447 – 449, 1985.

[150] M. Wegener, D. S. Chemla, S. Schmitt-Rink, and W. Schäfer,

"Line shape of time-resolved four-wave mixing," *Phys. Rev. A*, vol. 42, pp. 5675–5683, 1990.

[151] P. Bowlan, E. M. Moreno, K. Reimann, M. Woerner, and T. Elsaesser, "Ultrafast two-dimensional THz spectroscopy of graphene," *EPJ Web Conf.*, vol. 41, p. 04024, 2013.

[152] J. D. Cox, A. Marini, and F. J. G. De Abajo, "Plasmon-assisted high-harmonic generation in graphene," *Nature Communications*, vol. 8, 2017.

[153] C. Somma, G. Folpini, K. Reimann, M. Woerner, and T. Elsaesser, "Two-photon and two-phonon coherences in InSb from three-pulse THz spectroscopy." Seventh International Conference on Optical Terahertz Science and Technology, London 2017.

[154] W. S. Warren, H. Rabitz, and M. Dahleh, "Coherent control of quantum dynamics: The dream is alive," *Science*, vol. 259, pp. 1581–1589, 1993.

[155] P. C. M. Planken, I. Brener, M. C. Nuss, M. S. C. Luo, and S. L. Chuang, "Coherent control of terahertz charge oscillations in a coupled quantum well using phase-locked optical pulses," *Phys. Rev. B*, vol. 48, pp. 4903–4906, 1993.

[156] A. P. Heberle, J. J. Baumberg, and K. Köhler, "Ultrafast coherent control and destruction of excitons in quantum wells," *Phys. Rev. Lett.*, vol. 75, p. 2598, 1995.

[157] X. Marie, P. Le Jeune, T. Amand, M. Brousseau, J. Barrau, M. Paillard, and R. Planel, "Coherent control of the optical orientation of excitons in quantum wells," *Phys. Rev. Lett.*, vol. 79, pp. 3222–3225, Oct 1997.

[158] M. Woerner and J. Shah, "Resonant secondary emission from two-dimensional excitons: Femtosecond time evolution of the

coherence properties," *Phys. Rev. Lett.*, vol. 81, pp. 4208–4211, 1998.

[159] N. H. Bonadeo, J. Erland, D. Gammon, D. Park, D. S. Katzer, and D. G. Steel, "Coherent optical control of the quantum state of a single quantum dot," *Science*, vol. 282, no. 5393, pp. 1473–1476, 1998.

[160] M. Aeschlimann, M. Bauer, D. Bayer, T. Brixner, F. J. García de Abajo, W. Pfeiffer, M. Rohmer, C. Spindler, and F. Steeb, "Adaptive subwavelength control of nano-optical fields," *Nature*, vol. 446, pp. 301–304, 2007.

[161] T. Feurer, J. C. Vaughan, and K. A. Nelson, "Spatiotemporal coherent control of lattice vibrational waves," *Science*, vol. 299, pp. 374–377, 2003.

[162] J. Dai, N. Karpowicz, and X.-C. Zhang, "Coherent polarization control of terahertz waves generated from two-color laser-induced gas plasma," *Phys. Rev. Lett.*, vol. 103, p. 023001, 2009.

[163] P. Nuernberger, G. Vogt, T. Brixner, and G. Gerber, "Femtosecond quantum control of molecular dynamics in the condensed phase," *Phys. Chem. Chem. Phys.*, vol. 9, pp. 2470–2497, 2007.

[164] M. J. J. Vrakking and S. Stolte, "Coherent control of molecular orientation," *Chem. Phys. Lett.*, vol. 271, pp. 209–215, 1997.

[165] N. V. Vitanov, T. Halfmann, B. W. Shore, and K. Bergmann, "Laser-induced population transfer by adiabatic passage techniques," *Annu. Rev. Phys. Chem.*, vol. 52, pp. 763–809, 2001.

[166] S. G. Carter, V. Birkedal, C. S. Wang, L. A. Coldren, A. V. Maslov, D. S. Citrin, and M. S. Sherwin, "Quantum coherence in an optical modulator," *Science*, vol. 310, pp. 651–653, 2005.

[167] T. Kampfrath, A. Sell, G. Klatt, A. Pashkin, S. Mährlein, T. Dekorsy, M. Wolf, M. Fiebig, A. Leitenstorfer, and R. Huber, "Coherent terahertz control of antiferromagnetic spin waves," *Nature Photon.*, vol. 5, pp. 31–34, 2011.

[168] J. Stark, "Beobachtungen über den effekt des elektrischen feldes auf spektrallinien. i. quereffekt," *Annalen der Physik*, vol. 348, no. 7, pp. 965–982, 1914.

[169] A. M. Bonch-Bruevich and V. A. Khodovoi, "Current methods for the study of the Stark effect in atoms," *Usp. Fiz. Nauk*, vol. 93, pp. 71–110, 1967.

[170] S. H. Autler and C. H. Townes, "Stark effect in rapidly varying fields," *Phys. Rev.*, vol. 100, pp. 703–722, 1955.

[171] M. Gavrila and J. Z. Kaminski, "Free-free transitions in intense high-frequency laser fields," *Phys. Rev. Lett.*, vol. 52, pp. 613–616, 1984.

[172] C. N. Cohen-Tannoudji, *The Autler-Townes Effect Revisited*, pp. 109–123. New York, NY: Springer New York, 1996.

[173] F. Eickemeyer, M. Woerner, A. M. Weiner, T. Elsaesser, R. Hey, and K. H. Ploog, "Coherent nonlinear propagation of ultrafast electric field transients through intersubband resonances," *Appl. Phys. Lett.*, vol. 79, pp. 165–167, 2001.

[174] J. Faist, F. Capasso, D. L. Sivco, A. L. Hutchinson, C. Sirtori, and A. Y. Cho, "Quantum cascade laser," *Science*, vol. 264, pp. 553–556, 1994.

[175] R. Köhler, A. Tredicucci, F. Beltram, H. E. Beere, E. H. Linfield, A. G. Davies, D. A. Ritchie, R. C. Iotti, and F. Rossi, "Terahertz semiconductor-heterostructure laser," *Nature*, vol. 417, pp. 156–159, 2002.

[176] M. Wagner, H. Schneider, D. Stehr, S. Winnerl, A. M. Andrews, S. Schartner, G. Strasser, and M. Helm, "Observation of the intraexciton Autler-Townes effect in GaAs/AlGaAs semiconductor quantum wells," *Phys. Rev. Lett.*, vol. 105, p. 167401, 2010.

[177] J. Dynes, M. Frogley, M. Beck, J. Faist, and C. Phillips, "ac stark splitting and quantum interference with intersubband transitions in quantum wells," *Physical review letters*, vol. 94, no. 15, p. 157403, 2005.

[178] D. Dietze, J. Darmo, and K. Unterrainer, "THz-driven nonlinear intersubband dynamics in quantum wells," *Opt. Express*, vol. 20, p. 23053, 2012.

[179] D. Dietze, J. Darmo, and K. Unterrainer, "Efficient population transfer in modulation doped single quantum wells by intense few-cycle terahertz pulses," *New J. Phys.*, vol. 15, p. 065014, 2013.

[180] I. I. Rabi, "Space quantization in a gyrating magnetic field," *Phys. Rev.*, vol. 51, pp. 652–654, 1937.

[181] C. W. Luo, K. Reimann, M. Woerner, T. Elsaesser, R. Hey, and K. H. Ploog, "Rabi oscillations of intersubband transitions in GaAs/AlGaAs MQWs," *Semicond. Sci. Technol.*, vol. 19, pp. S285–286, 2004.

[182] R. W. Boyd, "Chapter 6 - nonlinear optics in the two-level approximation," in *Nonlinear Optics (Third Edition)* (R. W. Boyd, ed.), pp. 261–295, Burlington: Academic Press, third edition ed., 2008.

[183] K. Reimann, "Table-top sources of ultrashort THz pulses," *Rep. Prog. Phys.*, vol. 70, pp. 1597–1632, 2007.

[184] D. Ahn and S. L. Chuang, "Intersubband optical absorption

in a quantum well with an applied electric field," *Phys. Rev. B*, vol. 35, pp. 4149–4151, Mar 1987.

[185] A. Harwit and J. Harris Jr, "Observation of stark shifts in quantum well intersubband transitions," *Applied physics letters*, vol. 50, no. 11, pp. 685–687, 1987.

[186] F. Lima, M. Amato, O. Nunes, A. Fonseca, B. Enders, and E. da Silva Jr, "Unexpected transition from single to double quantum well potential induced by intense laser fields in a semiconductor quantum well," *Journal of Applied Physics*, vol. 105, no. 12, p. 123111, 2009.

[187] E. Niculescu and L. Burileanu, "Nonlinear optical absorption in inverse v-shaped quantum wells modulated by high-frequency laser field," *The European Physical Journal B-Condensed Matter and Complex Systems*, vol. 74, no. 1, pp. 117–122, 2010.

[188] E. Ozturk, "Simultaneous effects of the intense laser field and the electric field on the nonlinear optical properties in GaAs/GaAlAs quantum well," *Opt. Commun.*, vol. 332, pp. 136–143, 2014.

[189] P. Gaal, W. Kuehn, K. Reimann, M. Woerner, T. Elsaesser, R. Hey, J. S. Lee, and U. Schade, "Carrier-wave Rabi flopping on radiatively coupled shallow donor transitions in n-type GaAs," *Phys. Rev. B*, vol. 77, p. 235204, 2008.

[190] R. Eppenga, M. F. H. Schuurmans, and S. Colak, "New $k{\cdot}p$ theory for GaAs/$Ga_{1-x}Al_xAs$-type quantum wells," *Phys. Rev. B*, vol. 36, pp. 1554–1564, 1987.

[191] S. Lutgen, R. A. Kaindl, M. Woerner, T. Elsaesser, A. Hase, and H. Künzel, "Nonlinear intersubband absorption of a hot quasi-two-dimensional electron plasma studied by femtosecond

infrared spectroscopy," *Phys. Rev. B*, vol. 54, pp. R17343–17346, 1996.

[192] R. A. Kaindl, *Ultrafast mid-infrared studies of low energy excitations in solids*. Logos-Verlag, 2000.

[193] P. D. Dapkus, N. Holonyak, Jr., R. D. Burnham, D. L. Keune, J. W. Burd, K. L. Lawley, and R. E. Walline, "Spontaneous and stimulated carrier lifetime (77°K) in a high-purity, surface-free GaAs epitaxial layer," *J. Appl. Phys.*, vol. 41, pp. 4194–4199, 1970.

[194] P. Gaal, *Nonlinear THz spectroscopy on n-type GaAs*. PhD thesis, Humboldt Universitaet zu Berlin, 2008.

[195] N. Peyghambarian, H. M. Gibbs, J. L. Jewell, A. Antonetti, A. Migus, D. Hulin, and A. Mysyrowicz, "Blue shift of the exciton resonance due to exciton-exciton interactions in a multiple-quantum-well structure," *Phys. Rev. Lett.*, vol. 53, pp. 2433–2436, 1984.

[196] A. Sirenko, C. Bernhard, A. Golnik, A. M. Clark, J. Hao, W. Si, and X. Xi, "Soft-mode hardening in srtio3 thin films," *Nature*, vol. 404, no. 6776, pp. 373–376, 2000.

[197] I. Katayama, H. Aoki, J. Takeda, H. Shimosato, M. Ashida, R. Kinjo, I. Kawayama, M. Tonouchi, M. Nagai, and K. Tanaka, "Ferroelectric soft mode in a $SrTiO_3$ thin film impulsively driven to the anharmonic regime using intense picosecond terahertz pulses," *Phys. Rev. Lett.*, vol. 108, p. 097401, 2012.

[198] R. B. Hammond, K. Pencheva, K. J. Roberts, and T. Auffret, "Quantifying solubility enhancement due to particle size reduction and crystal habit modification: case study of acetyl salicylic acid," *Journal of pharmaceutical sciences*, vol. 96, no. 8, pp. 1967–1973, 2007.

[199] N. Blagden, M. de Matas, P. Gavan, and P. York, "Crystal engineering of active pharmaceutical ingredients to improve solubility and dissolution rates," *Advanced Drug Delivery Reviews*, vol. 59, no. 7, pp. 617 – 630, 2007. Drug Solubility: How to Measure it, How to Improve it.

[200] Y. Kim, K. Machida, T. Taga, and K. Osaki, "Structure redetermination and packing analysis of aspirin crystal," *Chem. Pharm. Bull.*, vol. 33, pp. 2641–2647, 1985.

[201] P. J. Wheatley, "The crystal and molecular structure of aspirin," *J. Chem. Soc.*, vol. 1964, pp. 6036–6048, 1964.

[202] A. M. Reilly and A. Tkatchenko, "Role of dispersion interactions in the polymorphism and entropic stabilization of the aspirin crystal," *Phys. Rev. Lett.*, vol. 113, p. 055701, 2014.

[203] R. Tawashi, "Aspirin: Dissolution rates of two polymorphic forms," *Science*, vol. 160, no. 3823, pp. 76–76, 1968.

[204] P. Vishweshwar, J. A. McMahon, M. Oliveira, M. L. Peterson, and M. J. Zaworotko, "The predictably elusive form ii of aspirin," *Journal of the American Chemical Society*, vol. 127, no. 48, pp. 16802–16803, 2005.

[205] R. Payne, R. C. Rowe, R. Roberts, M. Charlton, and R. Docherty, "Potential polymorphs of aspirin," *Journal of computational chemistry*, vol. 20, no. 2, pp. 262–273, 1999.

[206] C. Ouvrard and S. L. Price, "Toward crystal structure prediction for conformationally flexible molecules: the headaches illustrated by aspirin," *Crystal Growth & Design*, vol. 4, no. 6, pp. 1119–1127, 2004.

[207] A. D. Bond, R. Boese, and G. R. Desiraju, "On the polymorphism of aspirin: Crystalline aspirin as intergrowths of two "polymorphic" domains," *Angewandte Chemie International Edition*, vol. 46, no. 4, pp. 618–622, 2007.

[208] A. D. Bond, K. A. Solanko, S. Parsons, S. Redder, and R. Boese, "Single crystals of aspirin form ii: crystallisation and stability," *CrystEngComm*, vol. 13, no. 2, pp. 399–401, 2011.

[209] P. P. Bag and C. M. Reddy, "Screening and selective preparation of polymorphs by fast evaporation method: a case study of aspirin, anthranilic acid, and niflumic acid," *Crystal Growth & Design*, vol. 12, no. 6, pp. 2740–2743, 2012.

[210] S. Varughese, M. Kiran, K. A. Solanko, A. D. Bond, U. Ramamurty, and G. R. Desiraju, "Interaction anisotropy and shear instability of aspirin polymorphs established by nanoindentation," *Chemical Science*, vol. 2, no. 11, pp. 2236–2242, 2011.

[211] C. C. Wilson, "Interesting proton behaviour in molecular structures. Variable temperature neutron diffraction and *ab initio* study of acetylsalicylic acid: characterising librational motions and comparing protons in different hydrogen bonding potentials," *New J. Chem.*, vol. 26, pp. 1733–1739, 2002.

[212] M. Takahashi and Y. Ishikawa, "Translational vibrations between chains of hydrogen-bonded molecules in solid-state aspirin form I," *Chem. Phys. Lett.*, vol. 576, pp. 21–25, 2013.

[213] N. Laman, S. S. Harsha, and D. Grischkowsky, "Narrow-line waveguide terahertz time-domain spectroscopy of aspirin and aspirin precursors," *Appl. Spectroscopy*, vol. 62, pp. 319–326, 2008.

[214] K. Kawase, Y. Ogawa, H. Minamide, and H. Ito, "Terahertz parametric sources and imaging applications," *Semicond. Sci. Technol.*, vol. 20, pp. S258–265, 2005.

[215] R. C. Hilborn, "Einstein coefficients, cross sections, f values, dipole moments, and all that," *American Journal of Physics*, vol. 50, no. 11, pp. 982–986, 1982.

[216] C. Raman and T. Nedungadi, "The α-β transformation of quartz," *Nature*, vol. 145, no. 3665, p. 147, 1940.

[217] J. Scott, "Soft-mode spectroscopy: Experimental studies of structural phase transitions," *Reviews of Modern Physics*, vol. 46, no. 1, p. 83, 1974.

[218] W. Cochran, "Crystal stability and the theory of ferroelectricity," *Adv. Phys.*, vol. 9, pp. 387–423, 1960.

[219] R. Cowley, "The lattice dynamics of an anharmonic crystal," *Advances in Physics*, vol. 12, no. 48, pp. 421–480, 1963.

[220] D. Dougherty, "Interpretive barriers to successful product innovation in large firms," *Organization science*, vol. 3, no. 2, pp. 179–202, 1992.

[221] C. Kittel, *Introduction to solid state physics*. Wiley, 2005.

[222] F. Zamponi, P. Rothhardt, J. Stingl, M. Woerner, and T. Elsaesser, "Ultrafast large-amplitude relocation of electronic charge in ionic crystals," *Proc. Natl. Acad. Sci. USA*, vol. 109, pp. 5207–5212, 2012.

[223] R. W. Boyd, "Nonlinear optics," in *Handbook of Laser Technology and Applications (Three-Volume Set)*, ch. 3, pp. 161–183, Taylor & Francis, 2003.

[224] R. Lyddane, R. Sachs, and E. Teller, "On the polar vibrations of alkali halides," *Physical Review*, vol. 59, no. 8, p. 673, 1941.

[225] J. Hannay, "The clausius-mossotti equation: an alternative derivation," *European Journal of Physics*, vol. 4, no. 3, p. 141, 1983.

[226] J. Knoester and S. Mukamel, "Nonlinear optics using the multipolar Hamiltonian: The Bloch-Maxwell equations and local fields," *Phys. Rev. A*, vol. 39, pp. 1899–1914, 1989.

[227] S. Mukamel, Z. Deng, and J. Grad, "Dielectric response, nonlinear-optical processes, and the bloch–maxwell equations for polarizable fluids," *JOSA B*, vol. 5, no. 4, pp. 804–816, 1988.

[228] S. Mukamel, *Principles of nonlinear optical spectroscopy*. No. 6, Oxford University Press on Demand, 1999.

[229] T. Tyborski, R. Costard, M. Woerner, and T. Elsaesser, "Ultrafast vibrational dynamics of BH_4^- ions in liquid and crystalline environments," *J. Chem. Phys.*, vol. 141, p. 034506, 2014.

[230] D. F. Walls and G. J. Milburn, "Effect of dissipation on quantum coherence," *Phys. Rev. A*, vol. 31, p. 2403, 1985.

[231] J. P. Perdew, K. Burke, and M. Ernzerhof, "Generalized gradient approximation made simple," *Phys. Rev. Lett.*, vol. 77, pp. 3865–3868, 1996. **78**, 1396(E) (1997).

[232] V. Blum, R. Gehrke, F. Hanke, P. Havu, V. Havu, X. Ren, K. Reuter, and M. Scheffler, "Ab initio molecular simulations with numeric atom-centered orbitals," *Computer Physics Communications*, vol. 180, no. 11, pp. 2175–2196, 2009.

[233] A. Tkatchenko and M. Scheffler, "Accurate molecular van der waals interactions from ground-state electron density and free-atom reference data," *Physical review letters*, vol. 102, no. 7, p. 073005, 2009.

[234] A. Tkatchenko, R. A. DiStasio, Jr., R. Car, and M. Scheffler, "Accurate and efficient method for many-body van der Waals interactions," *Phys. Rev. Lett.*, vol. 108, p. 236402, 2012.

[235] A. Ambrosetti, A. M. Reilly, R. A. DiStasio Jr, and A. Tkatchenko, "Long-range correlation energy calculated from coupled atomic response functions," *The Journal of chemical physics*, vol. 140, no. 18, p. 18A508, 2014.

[236] A. Togo and I. Tanaka, "First principles phonon calculations in materials science," *Scripta Materialia*, vol. 108, pp. 1–5, 2015.

[237] J. E. Spanier and I. P. Herman, "Use of hybrid phenomenological and statistical effective-medium theories of dielectric functions to model the infrared reflectance of porous sic films," *Physical Review B*, vol. 61, no. 15, p. 10437, 2000.

[238] I. Tiginyanu, G. Irmer, J. Monecke, and H. Hartnagel, "Micro-raman-scattering study of surface-related phonon modes in porous gap," *Physical Review B*, vol. 55, no. 11, p. 6739, 1997.

[239] R. Ruppin, "Surface effects on optical phonons and on phonon-plasmon modes," *Surface Science*, vol. 34, no. 1, pp. 20–32, 1973.

Declarations

I declare that I have produced this doctor's thesis independently using only the literature and the tools I have specified, in accordance with section 7 para. 3 of the Faculty of Mathematics and Natural Sciences PhD regulations, published in the Official Gazette of Humboldt-Universität zu Berlin (*Amtliches Mitteilungsblatt*) no. 126/2014 on 18/11/2014.

I have not applied for a doctoral degree in the doctoral subject of Physics elsewhere and do not hold a doctoral degree in the doctoral subject of Physics.

I have taken due note of the Faculty of Mathematics and Natural Sciences PhD Regulations, published in the Official Gazette of Humboldt-Universität zu Berlin (*Amtliches Mitteilungsblatt*) no. 126/2014 on 18/11/2014.

Berlin, 19th July 2017 Giulia Folpini